DESIGN AND ANALYSIS OF ADVANCED MATERIALS IN A THERMAL/ACOUSTIC ENVIRONMENT
Delivery Order 0007: Volume 1–Structural Health Monitoring

Ramana V. Grandhi and Randy Tobe

Wright State University

MARCH 2010
Final Report

STINFO COPY

AIR FORCE RESEARCH LABORATORY
AIR VEHICLES DIRECTORATE
WRIGHT-PATTERSON AIR FORCE BASE, OH 45433-7542
AIR FORCE MATERIEL COMMAND
UNITED STATES AIR FORCE

NOTICE AND SIGNATURE PAGE

*//Signature//   //Signature//
_____   _____
TRINA L. BORNEJKO   DAVID M. PRATT, PhD
                                                             Technical Advisor
                                                             Structures Division
                                                             Aeronautical Sciences Division

1. REPORT DATE *(DD-MM-YY)*	2. REPORT TYPE	3. DATES COVERED *(From - To)*
March 2010	Final	15 July 2005 – 30 March 2010

4. TITLE AND SUBTITLE	5a. CONTRACT NUMBER
DESIGN AND ANALYSIS OF ADVANCED MATERIALS IN A THERMAL/ACOUSTIC ENVIRONMENT	FA8650-04-D-3446-0007
Delivery Order 0007: Volume 1–Structural Health Monitoring	5b. GRANT NUMBER
	5c. PROGRAM ELEMENT NUMBER
	0602201

6. AUTHOR(S)	5d. PROJECT NUMBER
Ramana V. Grandhi and Randy Tobe	A0B7
	5e. TASK NUMBER
	5f. WORK UNIT NUMBER
	0A

7. PERFORMING ORGANIZATION NAME(S) AND ADDRESS(ES)	8. PERFORMING ORGANIZATION REPORT NUMBER
Wright State University Department of Mechanical and Materials Engineering Dayton, OH 45435	

9. SPONSORING/MONITORING AGENCY NAME(S) AND ADDRESS(ES)	10. SPONSORING/MONITORING AGENCY ACRONYM(S)
Air Force Research Laboratory Air Vehicles Directorate Wright-Patterson Air Force Base, OH 45433-7542 Air Force Materiel Command United States Air Force	AFRL/RBSB
	11. SPONSORING/MONITORING AGENCY REPORT NUMBER(S)
	AFRL-RB-WP-TR-2010-3028

12. DISTRIBUTION/AVAILABILITY STATEMENT
Approved for public release; distribution unlimited.

13. SUPPLEMENTARY NOTES
PAO Case Number: 88ABW 2010-1341; Clearance Date: 22 Mar 2010. Report contains color.

14. ABSTRACT

Air vehicles flying at hypersonic speeds encounter extreme thermal, aerodynamic and acoustic loads, utilizing thermal protection systems to shield the main structure from these loads.One type of failure in a mechanically attached thermal protection system is fastener failure. Determining structural health monitoring on the fastener health of the thermal protection system is needed and can be completed by analyzing changes in the dynamic characteristics of the system due to fastener failure. The damage detection metrics include the existing modal parameters–modal assurance criterion (MAC), partial (PMAC), and coordinate (CMAC)–as well as two new modal parameters–normalized coordinate MAC and normalized coordinate MAC X summation were investigated. Two new modal parameters were formulated to identify mode shape changes in a structure due to global damage to the structure. Two damage states caused a minimal change to the low-frequency structural dynamics and could not be localized with any of the investigated damage metrics.

15. SUBJECT TERMS
reusable launch vehicle, risk-minimized design, flutter, epistemic, aleatory, and model-form uncertainties

16. SECURITY CLASSIFICATION OF:			17. LIMITATION OF ABSTRACT:	18. NUMBER OF PAGES	19a. NAME OF RESPONSIBLE PERSON (Monitor)
a. REPORT	b. ABSTRACT	c. THIS PAGE	SAR	134	Trina L. Bornejko
Unclassified	Unclassified	Unclassified			19b. TELEPHONE NUMBER (Include Area Code) N/A

i

Contents

List of Tables

List of Figures

GLOSSARY

C-C   Carbon-carbon

CCF   Complex Correlation Coefficient

COMAC   Coordinate Modal Assurance Criterion

CORTHOG Coordinate Orthogonality Check

E/M   Electro-mechanical

ECOMAC Enhanced Coordinate Modal Assurance Criterion

FAST   Future-Responsive Access to Space Technologies Program

FDAC   Frequency Domain Assurance Criterion

FMAC   Modal Assurance Criterion with Frequency Scales

FRAC   Frequency Response Assurance Criterion

FRF   Frequency Response Function

IMAC   Inverse Modal Assurance Criterion

MAC   Modal Assurance Criterion

MACRV   Modal Assurance Criterion using Reciprocal Vectors

MACSR   Modal Assurance Criterion Square Root

MLP   Multilayer Perceptron

NOCOMAC Nodal Coordinate Modal Assurance Criterion

NOCOMACSUM Nodal Coordinate Modal Assurance Criterion Summation

P-waves   Pressure Waves

PMAC   Partial Modal Assurance Criterion

PWAS   Piezoelectric Wafer Active Sensor

PZT   Piezoceramic

S-waves   Shear Waves

SH   Shear Horizontal

SHM   Structural Health Monitoring

SMAC   Scaled Modal Assurance Criterion

TOF   Time of Flight

TPS   Thermal Protection System

WMAC   Weighted Modal Assurance Criterion

FOREWORD

Chapter 1

SUMMARY

Air vehicles flying at hypersonic speeds encounter extreme thermal, aerodynamic and acoustic loads. To maintain the structural integrity of the flight vehicle, a thermal protection system shields the main structure from these loads. Therefore, maintaining the health of the thermal protection system is critical for a successful mission and vehicle safety. One of the more common types of failure in a mechanically attached thermal protection system is fastener failure. Since reducing vehicle turnaround time between flights is desired, creating an automated inspection system to perform structural health monitoring on the fastener health of the thermal protection system is needed. This can be completed by analyzing changes in the dynamic characteristics of the system due to fastener failure. While much of the recent experimental research focuses on using sensors to detect high-frequency dynamic changes (well above 10.0 kHz and into the MHz) in the system to detect damage, this research focuses on investigating fastener failure damage where only low-frequency dynamics are available (up to 2.0 kHz was used during experimentation).

This involves validating a finite element model with low-frequency experimental dynamic tests to ensure the geometry, boundary conditions, material properties, and finite element mesh properly capture the physical characteristics of the structure. The finite element model validation begins with the formation of a finite element model created to capture the geometry measured on the investigated structure. An inverse optimization problem is formulated to account for the uncertainty of the composite material properties. The bounded design variables for the inverse optimization problem are material properties with values based on the limited available material property data. The difference between the natural frequency values of the finite element model and the exper-

imental results create the objective function for the inverse optimization problem. The inverse optimization problem resulted in a validated finite element model with accurate results compared to the experimental data. After the inverse optimization problem validated the finite element model, the damage states are simulated with the finite element model.

After the finite element model is validated for the healthy state with free-free boundary conditions, the global boundary conditions and fastener failure damage states are implemented. This damage simulation allows a better understanding of how the damage states cause low-frequency dynamic changes without requiring a experimental data for each of the damage states of interest. The damage detection metrics include the existing modal parameters—modal assurance criterion, partial modal assurance criterion, and coordinate modal assurance criterion—as well as two new modal parameters—normalized coordinate modal assurance criterion and normalized coordinate modal assurance criterion summation. The existing modal parameters provide data about the correlation between modes (modal assurance criterion), the correlation between parts of mode shapes (partial modal assurance criterion), and which degrees-of-freedom contribute negatively to a low modal assurance criterion value (coordinate modal assurance criterion).

The two new modal parameters were formulated to identify mode shape changes in a structure due to global damage to the structure. They attempt to localize the areas of the mode shape with the largest changes between the healthy and damaged state, which are assumed to be close to the damaged portion of the structure, by investigating the differences between the healthy and damaged mode shapes when they are normalized to different nodes throughout the structure. The new damage parameters successfully localized the damage in the structure more often than the existing modal parameters used. While the majority of damage states implemented were successfully localized to the correct location of the failed fastener, two damage states caused a minimal change to the low-frequency structural dynamics and could not be localized with any of the investigated damage metrics.

Chapter 2

INTRODUCTION

This chapter introduces the problem statement of fastener failure in a structure and the motivation for detecting these failures with structural health monitoring (SHM) techniques. While the structure investigated in this work focuses on thermal protection systems (TPS), the techniques are applicable to any structure where detecting fastener failure is of interest to the researcher. The chapter then provides an overview of the literature of SHM before presenting an outline of the research methodology for this project.

2.1   Motivation

Hypersonic flight is required to maintain air and space supremacy for the United States. Hypersonic flight vehicles are required for launching payloads, such as satellites and components for the space station and Hubble telescope, out of Earth's atmosphere. These vehicles require a TPS to shield the main structure from the extreme thermal, acoustic, and pressure loads encountered during missions. Any severe damage to the TPS can lead to a catastrophic loss of vehicle and crew. Therefore, it is important to monitor the TPS to prevent minor damage from becoming worse. Monitoring an entire vehicle for structural integrity can be a very long, expensive, and labor-intensive process. Integrating an SHM system into the vehicle design can decrease the cost, time, and labor required to monitor the TPS health by utilizing sensors to automate the damage detection process. This can reduce the amount of downtime between vehicle missions significantly, which is a priority for next-generation spacecraft—such as in the Future-Responsive Access to Space

3

Technologies Program (FAST) program. Since fastener failure is one of the more common types of damage for mechanically attached TPS, this will be the focus of the research presented here. While the methods used here can be implemented on any structure encountering global damage (such as the fastener failure in this research), this work will focus on a TPS prototype composed of four carbon-carbon load-carrying plates with backing insulation bolted to carbon/silicon carbide brackets that are bolted to a thin metallic backing plate. The fastener failure is restricted to the bolted locations where the load-carrying plates are connected to the brackets. The bolted damage in this research is one type of fastener failure. The methods used here would be applicable to other types of fastener failure—such as damaged rivets—as well. The terms fastener and bolt are used interchangeably in this research.

2.2 SHM Literature

2.2.1 Historical Perspective

As vehicles, buildings, bridges, and other structures age, they begin to deteriorate. Detecting damage before it becomes significant enough to cause a catastrophic failure in the structure is important to maintain usability and increase safety for individuals around the aging structure. While damage can often be visually detected without any outside equipment, this is an expensive and labor-intensive process. Structural health monitoring was developed to detect the damage at early stages without the need for constant human intervention. The offshore oil industry utilized vibration-based damage detection techniques in the 1970s and early 1980s [1–10]. The offshore oil industry health monitoring results were not very successful. Because their above-water-line measurements only provided information about resonant frequencies, uniqueness issues arose during damage prediction. Data also was corrupted by environmental conditions, equipment noise, and changing mass (caused by changing fluid tank levels). These failures show the difficulty involved in SHM and led to the oil industry abandoning the technology in the mid 1980s. The difficulty in using resonant frequencies, modal damping, and mode shape vectors has been mentioned in literature reviews [11–13].

Dynamic-based SHM was used to investigate many different structures throughout the 1980s and 1990s. A brief review of some of the different early work in SHM includes the following: the 1980s initiated the investigation of metal and composite beams [14–17], bridges [18–20], the space shuttle [21–23], and nuclear plants [24]. Additional damage detection research originating in the late 1980s and the 1990s involved trusses [25–27], plates [28–32], buildings [33, 34], concrete beams [35, 36], shells and frames [37–39], horizontal axis wind turbine blades [40], and aircraft structures [41]. The global methods used in these damage detection investigations will be mentioned in more detail in Section 2.2.3.

SHM typically defines the following four levels of damage identification [42]:

- Level 1: Determination that damage is present in the structure

- Level 2: Level 1 plus determination of the geometric location of the damage

- Level 3: Level 2 plus quantification of the severity of the damage

- Level 4: Level 3 plus prediction of the remaining service life of the structure.

While determining the presence of damage has been successfully achieved for many different structures, materials, and types of damage, achieving the final level (prediction of the remaining service life of the structure) is a much more challenging and difficult problem. Some of the most common uses for SHM include detecting: cracks (and crack propagation), composite delamination, corrosion, mass changes, part degradation, and fastener failure. When a structure's dynamics is being used to investigate its health, the method (low-frequency methods or high-frequency methods) best suited to the problem depends on the type of damage expected. High-frequency methods are typically used for detecting small structural changes (such as cracks, composite delamination, and small changes in mass) since they investigate local areas. Low-frequency vibration-based methods are global in nature, so they are typically used when characterizing the entire structure (such as fastener failure and changing boundary conditions). While a distinct cutoff frequency between when low-frequency methods no longer work and high-frequency methods must be used does not

exist, one example for detecting the dynamics of a small steel beam was mentioned in Giurgiutiu's book [43]. When the beam was excited with an impact and the response was sensed with two strain gauges, the first two natural frequencies—1387 Hz and 3789 Hz—were detected, but the next natural frequencies—predicted to be around 7547Hz—was not. The higher natural frequencies were detected with the high-frequency electromechanical impedance method. The methods covered in Sections 2.2.2 and 2.2.3 focus on methods used primarily in structural health monitoring, and not on other damage detection methods (such as liquid penetration inspection, radiography, infrared thermography, eddy currents, etc.) used primarily in nondestructive evaluation and nondestructive inspection.

2.2.2 High-Frequency Methods

Methods that sense the structural dynamics based on introduced high-frequency waves (with frequencies well above 10 kHz and sometimes into the MHz range) are typically better at detecting smaller, more localized damage than the low-frequency vibration-based methods. Many of these testing methods utilize piezoelectric materials as sensors and/or actuators. Piezoelectric materials create a mechanical stress when an electric load is placed on them and generate electricity when a mechanical stress is applied to them, allowing one piezoelectric device to be used to both actuate and sense the dynamics of the system. A detailed book by Guirgiutiu [43] covers the theory, examples, and uses of piezoelectric wafer active sensors (PWAS) for many high-frequency SHM methods. While many publications classify their transducers as piezoceramics (PZT), the following sections will use PWAS as a generalized term to represent all piezoelectric transducers that can be used for sensing and actuating a structure.

2.2.2.1 Electro-Mechanical Impedance Method

The electro-mechanical (E/M) impedance method uses PWAS transducers as high-frequency modal sensors. This method couples the electrical impedance at the PWAS terminals with the mechanical impedance of the structure being investigated. This allows changes in the mechanical resonance

spectrum to be detected with the electrical signals generated at the PWAS terminals. Mechanical impedance has been used to detect damage for several decades [44]. It has since grown to be commonly used for detecting disbonds and delaminations inside laminated structures and composite materials. The E/M impedance method is an improvement over the mechanical impedance method. Advantages of the E/M impedance method over the mechanical impedance method include sensor size (thin, nonintrusive PWAS versus bulky transducers), testing availability (permanently attached PWAS transducers versus manually applying transducers to various points of interest), type of excitation (in-plane strain excitation versus normal force excitation), and impedance measuring (as a direct electrical quantity versus indirect mechanical quantities) [43]. Surface-attached PWAS have been used for coupled E/M analysis of adaptive systems since the mid-1990s [45]. One form of the electrical admittance measured at the terminals of a PWAS is

$$Y(\omega) = i\omega C \left(1 - \kappa_{31}^2 \frac{Z_{str}(\omega)}{Z_{str}(\omega) + Z_A(\omega)} \right) \qquad (1)$$

where C is the electrical capacitance of the PWAS, κ_{31} is the electro-mechanical cross coupling coefficient of the PWAS, $Z_{str}(\omega)$ is the one-degree-of-freedom structural impedance observed by the PWAS, and $Z_A(\omega)$ is the quasi-static impedance of the PWAS [43].

This formula has been used to show that the E/M admittance response accurately reflects the dynamic response of the system. In this one-degree-of-freedom coupled-system resonance, the real part of the admittance has a distinct peak shifted due to the additional stiffness caused by the PWAS. Other early research in the E/M impedance method used the half-power bandwidth method to accurately determine the natural frequency values of a structure [46]. These early works demonstrated that a permanently attached PWAS can be used as a structural-identification sensor since the PWAS terminals reflect the coupled-system dynamics. The E/M impedance method was first used for SHM to detect damage in a truss structure by Sun, et al. [47]. It was first shown to have extreme sensitivity to local damage and insensitivity to far-field damage in the tail section of a Piper Model 601P airplane [48]. While much literature exists focusing on implementing the

impedance method to detect damage, it will not be mentioned in detail here since this method was not used in this research. Additional details on the impedance method's use in SHM can be seen in a literature overview by Park, et al. [49].

2.2.2.2 Guided Waves

Guided waves are useful in SHM since they can travel large distances in a structure with minimal energy loss, allowing large areas to be investigated from a single location. Different types of ultrasonic waves exist; the best type of guided wave to use depends on the geometry of the structure being investigated. Three types of guided ultrasonic waves and the methods that use these waves for damage detection will now be briefly reviewed..

Rayleigh Waves   Rayleigh waves can be used to detect damage in solids that contain a free surface. They are also known as surface acoustic waves and surface-guided waves. Rayleigh waves propagate close to the surface of the structure with the amplitude decreasing rapidly with depth. Rayleigh waves are polarized in a plane perpendicular to the surface. The analytical solution to the Rayleigh-wave particle motion is contained in the vertical plane, meaning the x- and y-components of the velocity are nonzero and the z-component is equal to zero.

Shear Horizontal Plate Waves   Shear horizontal (SH) waves have a shear-type particle motion within the horizontal plane. When drawing SH waves in three-dimensions, the y-axis is typically placed vertically while the x-axis and z-axis compose the horizontal plane through which the SH waves propagate. SH waves propagate along the x-axis and the particle motion occurs along the z-axis. This is shown using Figure 1 from Giurgiutiu [43]. Implementing boundary conditions on the analytical problem for SH waves leads to a product of sine and cosine being equal to zero. When the sine component equals zero, the solution leads to symmetric modes (S-modes). When the cosine component equals zero, antisymmetric modes (A-modes) are formed. The analytical equations demonstrating the physical phenomena of SH waves encountered experimentally are covered by Guirgiutiu [43].
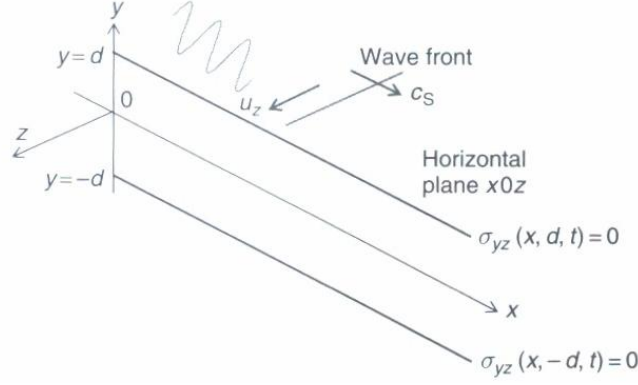
Figure 1: Shear Horizontal Wave Axes and Particle Motion Definition

Lamb Waves Lamb waves, also known as guided plate waves, are ultrasonic waves that are guided between two parallel free surfaces (such as the upper and lower surfaces of a plate). These waves were first theoretically described in the early 1900s by Horace Lamb [50]. It was much later that Lamb waves were actually generated to detect structural damage [51]. The Rayleigh-Lamb equation provides a number of solutions for Lamb waves, both symmetric modes (S_0, S_1, S_2,...) and antisymmetric modes (A_0, A_1, A_2,...). At low frequencies, symmetric Lamb waves approach the behavior of the axial plate waves while antisymmetric Lamb waves approach the behavior of flexural plate waves. The speed of Lamb waves depends on the frequency, plate thickness, and Lamb-wave mode. Lamb waves consist of a pattern of standing waves in the thickness direction of the plate traveling like waves along the guided path. Some of the beneficial characteristics of guided Lamb waves include: variable mode structure and distributions, multi-mode character, sensitivity to different types of flaws, propagation over long distances, and the capability to follow curvature and reach hidden and/or buried parts [43].

Wave Propagation Wave propagation works for damage detection by observing changes from what is expected from the sensors due to the wave interacting with the damage. For example, when a guided wave strikes the tip of a crack, it can change direction and be reflected back to a sensor before it would without the presence of damage. Wave propagation is one form of ultrasonic inspection. Ultrasonic inspection has been used in nondestructive evaluation methods to detect

damage for several decades. Ultrasonic testing involves at least one of the following measurements: time of flight (TOF), path length, frequency, phase angle, amplitude, acoustic impedance, and angle of wave deflection. PWAS can be placed on the surface of a structure to induce ultrasonic waves to perform the following techniques: pulse-echo, pitch-catch, and pulse-resonance [52].

Many types of waves can be used to investigate a structure, depending on its geometry. Pressure waves (P-waves), shear waves (S-waves), or a combination of the two can be used to investigate an infinite solid medium. P-waves work best for through-the-thickness detection of anomalies along the sound path. However, P-waves cannot reliably detect localized surface flaws and cracks. Rayleigh waves can be used to detect damage on a free surface of a solid structure. Guided Lamb waves allow thin-walled structures to be inspected efficiently. Since Lamb waves are the most common waves used for damage detection, this will be the wave type mentioned for damage detection in the next paragraph.

The pulse-echo method of damage detection can use one PWAS to transmit and detect Lamb waves in a plate. The transmitted Lamb waves are transmitted into the plate and received as multiple echoes resulting from reflections at the plate edges by the PWAS. A correlation between the TOF of each wave and the distance traveled by that wave must be established. While the TOF is immediately known when a wave arrives, determining the path traveled by the wave is much more difficult since an approximate traveled distance does not always clearly define the wave path due to the circular wave front being reflected at all edges of the plate. After understanding what the expected reflections are at the edges of the structure being investigated, detecting changes in the expected received waves must be accomplished for damage detection. When the propagating wave encounters a defect and reflects back to the sensor, this new arriving wave must be distinguishable from the reflections in the healthy structure for the defect to be detected. Since Lamb waves are dispersive in nature (their speed depends on their frequency), Lamb-wave tuning methods are used to select the Lamb waves [53].

The pitch-catch method is used to detect structural changes between at least one transmitter and at least one receiver. One PWAS transmits the Lamb wave into the plate and another PWAS

(or array of PWAS) receives the Lamb wave. The guided wave amplitude, phase, dispersion, and TOF are compared with a predefined healthy state to detect damage introduced to the structure. The pitch-catch method is typically used to detect cracks, corrosion, disbonded adhesive joints, and composite delamination. The probability of detecting the localized damage increases as the size of the defect increases.

2.2.3 Low-Frequency Vibration-Based Methods

Vibration-based methods investigate how changes in the low-frequency modal properties (modal frequencies, modal damping ratios, and mode shapes) correspond to changes in the mechanical properties of a structure due to damage. The frequency for these methods work up to several kHz, but the instruments commonly used to collect the low-frequency dynamics lose accuracy at higher frequencies. Some of the past research completed using vibration-based methods are shown in the following sections.

2.2.3.1 Frequency Changes

Changes in structural properties result in changes in vibration frequencies that allow for the completion of damage identification and health monitoring. A large amount of literature exists on investigating shifts in natural frequencies due to structural damage. However, practical limitations do exist for applying frequency shifts as the sole method for health monitoring, due to its somewhat low sensitivity to damage. This requires either very precise dynamic measurements (which are difficult to obtain in a real-world problem with changing environmental characteristics) or large levels of damage (which are trying to be avoided with the implementation of SHM). One specific example of the large level of damage not being easily detectable with frequency changes has been observed with the I-40 bridge over the Rio Grande. A 96.4% reduction in the cross-sectional stiffness at the center of a main plate girder (which reduces the bending stiffness of the overall bridge cross-section by 21%) did not result in significant reductions of the observed modal frequencies [54]. This lack of sensitivity was due to the damage location being near a node point of the mode shape.

11

Currently, frequency shifts are most useful for damage detection for very controlled environments, such as for quality control in manufacturing [11]. One example of a frequency shift being used is the detecting out-of-roundness of ball bearings with the use of precise sine-sweep frequency measurements [55]. Additionally, low-frequency shifts investigate the structure globally, making it difficult to localize detected damage. Improved localization can occur with frequency changes by investigating high-frequency shifts (which excite and extract local modes) and multiple low-frequency shifts being combined to provide spatial information about structural damage. Several references state that mode shape information has to be accounted for in addition to frequency shifts to properly detect and/or localize damage. This is often due to mode switches occurring between closely grouped resonant frequencies. The two ways SHM is completed with frequency shifts are the forward problem and the inverse problem.

The Forward Problem   The forward problem investigates frequency shifts for known type of damage. The known damage can be modeled mathematically and compared to experimentally measured frequencies to determine the presence of damage. The forward problem has been widely used since the mid-1970s. Most of the research mentioned in Section 2.2.1 involved the forward problem. Some of the damage types investigated with the forward problem include: removing members from an offshore tower [1,6], severance of structural members [2,5,7], composite cracks and/or delamination [56, 57], crack damage [8, 58–61], mass changes [9, 10], and beams with a slot [62, 63]. While severe damage could occasionally be successfully detected with the forward method, it did not do well in most instances.

The Inverse Problem   The inverse problem calculates damage parameters, such as crack length and/or location, from frequency shifts. The inverse problem typically attempts to achieve Level 2 or Level 3 damage identification while the forward problem typically achieves only Level 1 damage identification. Some of the damage types the inverse problem has been used to investigate include: changing dynamic moduli in composites [64], changing structural stiffness parameters (typically due to cracks) [27, 29, 33, 65–69], and microcracking and transverse cracks in composites [70].

12

2.2.3.2 Mode Shape Changes

Mode shape changes provide more information than frequency changes alone. Some damage can cause a mode shape to change without its associated resonant frequency shifting a detectable amount compared to the experimental uncertainty encountered during testing. Many metrics have been created to better understand and convey mode shape changes numerically. Some of these modal criteria are: modal assurance criterion (MAC), the weighted modal assurance criterion (WMAC), partial modal assurance criterion (PMAC), modal assurance criterion square root (MACSR), scaled modal assurance criterion (SMAC), modal assurance criterion using reciprocal vectors (MACRV), modal assurance criteria with frequency scales (FMAC), coordinate modal assurance criterion (COMAC), the enhanced coordinate modal assurance criterion (ECOMAC), mutual correspondence criterion, modal correlation coefficient, inverse modal assurance criterion (IMAC), frequency response assurance criterion (FRAC), complex correlation coefficient (CCF), frequency domain assurance criterion (FDAC), and coordinate orthogonality check (CORTHOG). A brief summary of these criteria and their uses follow below.

The MAC [71, 72] provides a measure of consistency (degree of linearity) between two modal vectors. It shows how similar two modal vectors (from different excitation locations, models, or system states) are. MAC values range from zero to one. A MAC value close to zero represents no consistent correspondence between the two modal vectors. A value of one represents a perfect correspondence between the two modal vectors. When two modal vectors representing the same state are compared, the diagonal terms of a MAC matrix represent the same modes being compared to each other, and the values should be close to unity. The off-diagonal terms in this MAC matrix should be much lower since they compare different modal vectors that are generally not similar. When a healthy state is compared to a damaged state, variations from the anticipated MAC matrix can be used to detect damage.

For example, if a diagonal term is significantly lower than unity—0.7 and 0.85 are used as definite and intermediate cutoffs in this research—it represents the damaged modal vector being significantly different from the healthy modal vector to which it is compared. Another way to

detect damage using the MAC matrix is two off-diagonal terms being close to unity while the diagonal terms bordering them are significantly smaller; this demonstrates a mode switch where the damage causes one modal vector which was previously excited at a higher frequency than another to be now be excited at a frequency lower than the other, causing their sequential order to switch. The MAC indicates consistency (not validity or orthogonality) between the two modal vectors; therefore, if invalid assumptions result in the same errors, random, or bias in both modal vectors being compared, they will not be detected with the MAC [73]. The MAC has been used in combination with frequency changes to detect individual damaged bolts in a constrained plate [74]. This research used manual evaluation and human judgment to achieve damage localization based on the experimental and finite element results. The MAC's linear, least-squares computational approach to analyze two vector spaces has led to the other criteria mentioned in the preceding paragraph.

Since the MAC is sensitive to sensor distribution, the WMAC was created to account for mass or stiffness distribution. The WMAC allows users to adjust the MAC to weight the degrees-of-freedom in the modal vectors according to mass or stiffness distribution, making it a pseudo-orthogonality check. The PMAC [75, 76] is a spatially limited version of the MAC. Instead of using all of the degrees-of-freedom available to calculate the MAC, a subset of the degrees-of-freedom are used with the same formula as the MAC. This allows a user to investigate only a certain sensor direction (x, y, and/or z) or only degrees-of-freedom from a single component of the entire structure. The MACSR [77] is more consistent with the orthogonality and pseudo-orthogonality calculations using an identity weighting matrix. Taking the square root of the MAC calculation tends to highlight the off-diagonal terms that are generally very small MAC values. The SMAC [78] is essentially a WMAC with the weighting matrix chosen to balance the scaling of translational and rotational degrees-of-freedom in the modal vectors. The SMAC is useful for normalizing magnitude differences in the modal vectors containing different engineering units. Without this normalization, the MAC would be dominated by the larger values since it minimizes the squared error.

The MACRV [79] compares reciprocal modal vectors with analytical modal vectors and is similar to a pseudo-orthogonality check. The reciprocal modal vector is defined as the vector that yields unity when transposed and premultiplied by a specific modal vector. A value of zero results from this same computation using the reciprocal modal vector and any other modal vector (or reciprocal modal vector). The MACRV serves as a mode isolation check provided by each reciprocal modal vector compared to expected analytical modes. Frequency scaling is added to the MAC to form the FMAC [80, 81]. The FMAC "offers a means of displaying simultaneously the mode shape correlation, the degree of spatial aliasing and the frequency comparison in a single plot." It is particularly useful in model correlation applications, such as model updating and assessment of parameter variation. The COMAC [76, 82] attempts to identify which degrees-of-freedom contribute negatively to a low value of MAC. The COMAC is calculated over a set of mode pairs that are identified to represent the same modal vector in a given frequency range. A COMAC value is computed for each degree-of-freedom in the mode pair.

The ECOMAC [83] is used to resolve problems with experimental modal vectors having calibration scaling errors and/or sensor orientation mistakes. The mutual correspondence criterion applied the MAC to vectors that do not originate as modal vectors. Instead, the mutual correspondence criterion [84] uses vector measures of acoustic information (velocity, pressure, intensity, etc.) and only correctly applies to real valued vectors. The modal correlation coefficient [85, 86] modifies the MAC to be more sensitive to small changes in magnitude that are not very noticeable with a least squares based correlation coefficient. It accomplishes the increased sensitivity with the introduction of a kink factor that accounts for slope discontinuities that may occur with damage. The IMAC [87] uses the inverse of the modal coefficients with the computational scheme of the MAC. This results in small modal coefficients that are insignificant in the MAC computation becoming large coefficients that are significant in the IMAC. Since the inverse is taken, difficulties arise if any modal coefficients are numerically zero.

The FRAC [88–90] can compare any two frequency response functions (FRF) representing the same input/output relationship. It can be used as a validation procedure between a model and

measured data. The basic assumption for the FRAC is that the FRFs being compared should be linearly related at all frequencies. The FRFs can be compared over the entire or partial frequency range collected as long as the same discrete frequencies are used in the comparison. The FRAC can serve as an independent check of the modal parameter estimation process. The CCF [91] is similar to the FRAC, only without squaring the numerator term. This causes a significant change that yields a complex coefficient. While the magnitude is the same as that of the FRAC, the CCF provides any systematic phase lag or lead between the two FRFs. When compared to an analytical FRF, the CCF can help detect the common problem of a constant phase shift due to experimental signal conditioning problems. The FDAC [92] calculation is similar to the FRAC, but it is evaluated with different frequency shifts. The FDAC is formulated to identify the difference in impedance model updating caused by the frequencies of resonances or anti-resonances. The CORTHOG [93] is a normalized error measure between the pseudo-orthogonality calculation and the analytical orthogonality calculation. This calculation uses several different normalizing or scaling methods. While mode shape changes were more successful than resonant frequency shifts alone, they were still not able to detect some damage states, such as localized damage caused by small cracks.

The MAC, PMAC, and COMAC are used to detect and localize damage using mode shapes found using a validated finite element model in Chapters 3 and 4. The MAC and PMAC were chosen since they allow for the creation of matrices with terms that numerically relate the healthy modal vector to the damaged modal vector for both the entire structure (MAC) and the individual load-carrying plates (PMAC) separately. These numbers show how the introduced damage to the system changes how the modal vectors relate to each other. The COMAC was used since it attempts to show what degrees-of-freedom used in the calculation of the MAC contribute to low MAC values. This is useful since the areas causing a low MAC likely occur close to the damage causing the change in mode shape.

2.2.3.3 Mode Shape Curvature/Strain Mode Shape Changes

An alternative to using mode shapes to investigate vibration changes spatially is to investigate mode shape derivatives, such as curvature. For beams, curvature and bending strain are mathematically represented as

$$\varepsilon = \frac{y}{\rho} = \kappa y \tag{2}$$

where ε is strain, ρ is radius of curvature, and κ is curvature (or $1/\rho$) [94]. Directly measuring the strain or computing it from displacements or accelerations is required for these methods.

One common way to find derivatives with discrete points is using the finite difference method. Finite difference methods enter the values and distances of the spatial points surrounding the location of interest into a formula to approximate the derivative. The order and accuracy of the derivative depends on the number of surrounding points and the type of difference method being used. The central difference approximation was used to successfully detect damage in a finite element model of beam structures [95]. Another method creates a damage index for a linearly elastic beam structure composed of the quotient formed with the damaged fractional strain energy in the numerator and the undamaged fractional strain energy in the denominator [96,97]. A large damage index indicates a member is likely damaged, allowing for the severity of damage to be estimated based on the fractional change in bending stiffness for that member. This method does not require sensitivity matrices, but does require the structure to be represented by beam elements and spatial differentiation of measured mode shapes.

Chance, et al. [31] concluded that the numerical methods used to calculate curvature from mode shapes can result in unacceptably large errors. Chen and Swamidas [30] avoided these numerical errors by obtaining measured strains to directly measure plate curvature. This dramatically improved results over the results calculated using mode shapes. These improved results obtained using strain mode shapes also facilitated crack location in a cantilever plate. Another parameter initially composed of the damaged and undamaged displacements and resonant frequencies was found to be more sensitive to structural damage when computed with the damaged and undamaged

strain mode shapes and resonant frequencies [98]. Other research stated that using experimental data with the central difference approximation to calculate curvature change did not typically give a good indication of damage. The most important factor to obtain good results in this study was the selection of which modes are used in the analysis [99]. Strain changes were found to be much more sensitive to crack detection than frequency shifts, even at relatively large distances from the crack [39].

2.2.3.4 Methods Based on Dynamically Measured Flexibility

A dynamically measured flexibility matrix has been used to estimate changes in the static behavior of structures. This method calculates the flexibility matrix calculated from the dynamic response of the structure. The flexibility matrix relates the applied static force and the resulting structural displacement. Therefore, each column of the flexibility matrix represents the displacement pattern of the structure associated with a unit force being applied at that column's degree-of-freedom. The measured flexibility matrix is estimated from mass-normalized measured mode shapes and frequencies, as seen in Equation 3.

$$[G] = [\phi] [\Lambda]^{-1} [\phi]^T \qquad (3)$$

where $[G]$ is the n x n measured flexibility matrix, $[\phi]$ is an n x n matrix with the ith column being the mode shape corresponding to the ith resonant frequency, and $[\Lambda]$ is an n x n diagonal matrix with the resonant frequencies composing the diagonal in sequential order.

The flexibility matrix in Equation 3 is approximate since only the first few modes of the structure are measured. Creating the complete static flexibility matrix would require all mode shapes and frequencies to be measured. Damage detection is accomplished by comparing the damaged flexibility matrix to the flexibility matrix of either the undamaged structure or a finite element model. Due to the inverse relationship to the square of the modal frequencies, the measured flexibility matrix is most sensitive to changes in the lower-frequency modes of the structure. Some of

the methods used to detect damage are mentioned in the following paragraphs.

Changes in the flexibility of a structure have been used to detect (and localize, in some cases) damage for many different structures. Atkan, et al. [100] used the measured flexibility as a "condition index" and compared it to the static deflections by truck-load tests to indicate bridge integrity. Changes in the measured flexibility of a spliced beam with linear damage were successful in localizing damage using the first two measured modes of the structure [101]. The measured flexibility of a bridge examined the cross-sectional deflection profiles to indicate damage even without a baseline data set [102]. The measured flexibility has been decomposed into elemental stiffness parameters for an assumed structural connectivity. The flexibility matrix is decomposed by projecting it onto an assemblage of the element-level static structural eigenvectors [103]. Curvature changes in the deformed shape of the structure when subjected to a uniform load (called the uniform load surface) can be calculated using the uniform load flexibilities to indicate damage. The uniform load surface is sensitive to uniform deterioration. The curvature is calculated using the central difference method on the uniform load flexibility matrix, which is constructed by summing the columns of the measured flexibility matrix [104].

The pseudo-inverse relationship between the dynamically measured flexibility matrix and the structural stiffness matrix is the basis for the unity check method. It defines an error matrix (seen in Equation 4) to measure the degree to which the pseudo-inverse is satisfied:

$$[E] = \left[G^d \right] [K^u] - [I] \tag{4}$$

where $[E]$ is the error matrix, $\left[G^d \right]$ is the damaged flexibility matrix, $[K^u]$ is the undamaged stiffness matrix, and $[I]$ is the identity matrix.

The pseudoinverse is used since the dynamically measured flexibility matrix is typically rank-deficient, making the inverse infeasible. The unity check method was first used to locate modeling errors by using the location of the entry with maximum magnitude in each column to determine the model's error location. This method is sensitive to non-orthogonality in the measured modes [105].

19

The unity check method was then extended to damage detection by defining a least-squares problem for the elemental stiffness changes that are consistent with the unity check error in potentially damaged members [106]. The stiffness error matrix method computes an error matrix that is a function of the flexibility change in the structure and the undamaged stiffness matrix. The stiffness error matrix is calculated using Equations 5 and 6.

$$[E] = [K^u] [\Delta G] [K^u] \tag{5}$$

$$[\Delta G] = \left[G^d\right] - [G^u] \tag{6}$$

where $[E]$ is the stiffness error matrix, $[K^u]$ is the undamaged stiffness matrix, $[\Delta G]$ is the difference between the damaged flexibility matrix $\left(\left[G^d\right]\right)$ and the undamaged flexibility matrix $([G^u])$. This method has been used to indicate errors between measured parameters and analytical stiffness and mass matrices.

The stiffness matrix was used instead of the mass matrix, since it generally provides more information for damage identification [107]. The type of matrix reduction technique and number of modes used in the formation of the flexibility matrix were also investigated. Acceptable results were found with the usage of Guyan reduction and indirect reduction, but not with elimination [108]. Another use of the stiffness error matrix method divided the entries in the stiffness error matrix by the variance in natural frequency resulting from damage in each member. This weighted error matrix was successfully used to detect damage in both beam and plate models [109].

The residual flexibility matrix, $[G_r]$, represents the contribution to the flexibility matrix from modes outside the measured bandwidth. The residual flexibility matrix is added to Equation 3 to provide the exact flexibility matrix given in Equation 7, relating the measured modes and the residual flexibility:

$$[G] = [\phi] [\Lambda]^{-1} [\phi]^T + [G_r] \tag{7}$$

This technique estimates the unmeasured partition of the residual flexibility matrix because only one column of the frequency response function matrix can be measured for each modal excitation

degree-of-freedom. While it does not add any new information into the residual flexibility, it does complete the reciprocity of the residual flexibility matrix for use in the computation of measured flexibility. The inclusion of the measured residual flexibility in the computation of the measured flexibility matrix was found to yield a more accurate estimate of the static flexibility matrix [110, 111].

Use of the dynamically measured stiffness matrix is a variation of using the dynamically measured flexibility matrix. The dynamically measured stiffness matrix is the pseudoinverse of the dynamically measured flexibility matrix (the dynamically measured mass and damping matrices can also be computed, but are less common). Damage localization was successfully estimated using direct comparison of these measured parameter matrices [112]. Another method proposes locating damage by solving an "inverse connectivity" problem between the measured stiffness and mass matrices. This method evaluates the change in impedance between two structural degrees-of-freedom to estimate the level of damage in the connecting members [113].

2.2.3.5 Methods Based on Updating Structural Model Parameters

Another class of damage identification methods is based on updating model matrices to reproduce the measured static or dynamic response from the data. The updated matrices (such as mass, stiffness, and damping) are solved with a constrained optimization problem based on the structural equations of motion, the nominal model, and the measured data. Damage can be indicated and quantified based on comparisons of the updated matrices to the original correlated matrices. Some of the algorithms used to solve the set of equations can be classified into the following categories: objective method to be minimized, constraints placed on the problem, and numerical scheme used to implement the optimization problem.

The objective functions and constraints for the matrix update problem can vary between several different physically based equations depending on the updating algorithm. The typical eigenvalue

equation can be written as

$$\left((\lambda_i^u)^2 [M^u] + (\lambda_i^u) [C^u] + [K^u] \right) \{\phi^u\}_i = \{0\} \tag{8}$$

where λ_i^u and $\{\phi^u\}_i$ are the measured i^{th} eigenvalue and eigenvector of the undamaged structure for all measured modes and $[M^u]$, $[C^u]$, and $[K^u]$ are the undamaged mass, damping, and stiffness matrices. Substituting the damaged state eigenvalues $\left(\lambda_i^d\right)$ and eigenvectors $\left\{\phi^d\right\}_i$ to Equation 8 yields

$$\left(\left(\lambda_i^d\right)^2 [M^u] + \left(\lambda_i^d\right) [C^u] + [K^u] \right) \left\{\phi^d\right\}_i = \{E\}_i \tag{9}$$

where $\{E\}_i$ is defined as the "modal force error" or "residual force" for the ith mode of the damaged structure. This modal force error vector represents the harmonic force excitation that would result in the damaged mode shape when applied to the undamaged structure at the corresponding eigenfrequency [114]. Similar formulas can be seen in Equations 10 and 11 when using modal matrices of the damaged structure $\left(\left[M^d\right], \left[C^d\right], \left[K^d\right] \right)$ or perturbation matrices $([\Delta M], [\Delta C], [\Delta K])$:

$$\left(\left(\lambda_i^d\right)^2 \left[M^d\right] + \left(\lambda_i^d\right) \left[C^d\right] + \left[K^d\right] \right) \left\{\phi^d\right\}_i = \{0\} \tag{10}$$

$$\left(\left(\lambda_i^d\right)^2 [\Delta M] + \left(\lambda_i^d\right) [\Delta C] + [\Delta K] \right) \left\{\phi^d\right\}_i = \{E\}_i \tag{11}$$

where the perturbation matrices are defined as the difference between the undamaged modal matrices and the damaged modal matrices as seen in Equations 12-14.

$$[\Delta M] = [M^u] - \left[M^d\right] \tag{12}$$

$$[\Delta C] = [C^u] - \left[C^d\right] \tag{13}$$

$$[\Delta K] = [K^u] - \left[K^d\right] \tag{14}$$

The modal force error can be used as both an objective function and a constraint, depending on the method being used. Other constraints are typically based on the matrices being used. Some

of these constraints include preservation of the property matrix symmetry (the transpose of the perturbation matrices being equal to the perturbation matrices), preservation of the property matrix sparcity (the zero/nonzero pattern in the undamaged property matrices being the same as the pattern in the damaged property matrices), and preservation of the property matrix positivity (the transpose of any arbitrary vector times the perturbation of each property matrix times the arbitrary vector being greater than or equal to zero).

Optimal matrix update methods are commonly used to refer to methods that use a closed-form, direct solution to compute the damaged model matrices or perturbation matrices [11]. This method typically formulates the problem as a Lagrange multiplier or penalty-based optimization problem shown in Equation 15:

$$\min_{\Delta M, \Delta C, \Delta K} \{J(\Delta M, \Delta C, \Delta K) + \lambda R(\Delta M, \Delta C, \Delta K)\} \tag{15}$$

where J is the objective function, R is the constraint function, and λ is the Lagrange multiplier or penalty constant. Much of the research using the Lagrange multiplier focuses on minimizing the norm of the property perturbations with various constraints.

Another class of matrix updating methods, the sensitivity-based update methods, is based on the solution of a first-order Taylor series. These methods minimize an error function of the matrix perturbations. The basic theory of these methods is to iteratively determine a modified parameter vector based on the initial parameter vector and a series of parameter perturbation vectors that update the parameter vector being found. The parameter perturbation vector is typically computed from the Newton-Raphson iteration problem for minimizing an error function, often selected to be the modal force error mentioned in Equation 9. The various sensitivity-based update schemes have used many methods to estimate the sensitivity matrix. While the specific methods will not be mentioned in this document, the methods use either experimental or analytical quantities for the differentiation of either parameter derivatives or matrix derivatives. A detailed list and classification of the specific sensitivity-based update techniques can be found elsewhere [115] and will not

be provided here.

The design of a fictitious controller which would minimize the modal force error, known as eigenstructure assignment, is another matrix update method. The obtained controller gains are interpreted as parameter matrix perturbations to the undamaged structure. An in-depth overview of the eigenstructure assignment technique providing useful equations [116, 117] are not included since this method was not investigated in this research.

Additionally, some researchers have investigated hybrid matrix update methods. These methods typically incorporate a combination of the aforementioned matrix update methods (such as an optimal-update method and a sensitivity-based method [118–121]) to obtain improved and or more efficient damage detection results.

2.2.3.6   Pattern Recognition

Collecting experimental data of known damaged and healthy states to train a statistical pattern recognition algorithm has become increasingly popular. One very popular pattern recognition technique is using neural networks to estimate and predict both the extent and location of damage in complex structures. Various texts [122–127] provide additional information on pattern recognition, which will briefly be covered in this section. Multilayer perceptron (MLP) trained by backpropagation will be the focus of this section since it is the most common neural network used for pattern recognition. This type of neural network is a system of cascaded sigmoid functions where the outputs of one layer are multiplied by weights, summed, and then shifted by a bias before being used as inputs to the next layer. The sigmoid function—typically $\left(\frac{1}{1+exp(-a)}\right)$—enters the input for one layer as the variable a and feeds the output into the next layer. The actual function represented by the neural network is encoded by the weights and biases, which are adjusted by minimizing the error between the predicted and measured outputs. Experimental or computational runs are completed and entered as inputs to the MLP (if more adjustable weights exist than experiments, the data can be repeatedly run through the training algorithm) until a satisfactory error between the data and the neural network is obtained. After a pattern recognition algorithm has been trained,

it can then be tested (preferably with data not used to train the algorithm) with input data to determine how accurate the trained algorithm is at properly characterizing the healthy or damaged state of the system. Pattern recognition techniques have been used to detect damage on a wide variety of structures, including stiffened plates [128], buildings [129–131], cantilever beams [132], bridges [133], trusses [134–136], spring-mass systems [137, 138].

Damage states similar to what is completed in this research—fastener damage for mechanically attached plates—has also been completed using statistical pattern recognition [139–141]. This research gathers experimental data for a predefined number of classes, one healthy state and a varying number of damage states. The data is broken down into two groups: training data and testing data. The training data defines discriminant functions for each predefined class. Then, the testing data are used to identify features that are input into the discriminant functions. The testing data is then placed in the class that corresponds to the discriminant function with the maximum value. This allows the test data to be placed in three main categories: accurately predicting the class, missed detection, and false alarm.

2.2.3.7 Other Methods

A number of other vibration-based methods have been used for damage detection. A few of these will be mentioned here, while a more-comprehensive list can be found in vibration-based literature reviews [11, 13]. The random decrement technique uses a response to take N averages with the same time length and initial displacement and alternating positive and negative starting velocities. The advantage is that a random input can be used since the effect of the initial velocities and response to the excitation are greatly reduced due to the averaging. This leaves the response to the initial displacement as a vibration decay curve to identify the resonant frequency of the structure and its damping. One early use of the random decrement technique for damage detection was able to detect damage without localization in a scale-model offshore platform [142]. More recently, a random decrement showed the potential to detect a real fatigue crack in a cantilever beam without needing to know the input excitation [143]. Another technique developed a sensitivity formulation

based on the change of the frequency response function at any point, not just near resonances or anti-resonances. Many points are taken and used with a least squares fit to determine changes in physical parameters. This method requires responses for both the healthy and damaged structure in addition to a physical model that relates the damaged parameter to a physical parameter [144].

2.3 Research Methodology

Utilizing high-frequency dynamics, a large number of sensors (such as velocimeters or accelerometers), or statistical pattern recognition can improve the likelihood of detecting and localizing damage; however, these testing characteristics are not always usable due to the sensor type, sensor availability, or amount of experimental time required. For example, capturing the high-frequency dynamics of a structure can require either big, bulky equipment (such as conventional shakers) or piezoelectric actuator/sensors that are not as common as accelerometers. Also, a large number of sensors can allow a large amount of experimental data quickly, but can change the dynamics of the system due to added mass resulting from the sensors. Statistical pattern recognition can require a significant amount of time to pick parameters and collect experimental data to train and test the algorithm. The proposed research methodology focuses on accomplishing structural health monitoring when a limited number of accelerometers and experimental testing time are available. These restrictions do not allow for high-frequency experimentation or statistical pattern recognition to be performed. Initially, the research focused on performing a sizing optimization for the plate thicknesses of the TPS prototype using a finite element model. After this initial study was completed, the research focus shifted from optimizing the current TPS prototype for SHM based on natural frequency values to focusing on changes in the current design's mode shapes for SHM. This is the focus of the research methodology presented here.

The methodology begins with the creation of a finite element model designed to capture the physics of a real-world structure that accurately captures the low-frequency dynamics observed in a laboratory. Then, low-frequency dynamic experimentation—from zero to 2000 Hz—is completed at Wright-Patterson Air Force Base to validate the finite element results. Due to the composite

material properties being uncertain, the finite element model's material properties are updated to validate that the model properly captures the low-frequency dynamics, if needed. This validated finite element model is then used to simulate the healthy state and damage states of interest.

The damage states of interest in this research are fastener failure between a load-carrying plate and brackets. The fastener failure simulates a completely damaged bolt that is modeled by removing the bolt from the validated finite element model. Unlike localized damage that cannot be detected with global methods, this global damage does not require high-frequency dynamics—over 10 kHz—to detect the damage. Low-frequency dynamic characteristics—resonant frequencies and mode shapes—are then extracted and compared between the damaged states and the healthy state. Existing modal criteria newly created modal criteria use mode shape data to detect fastener failure damage in this research. Changes between the healthy and damaged states result in changes in the calculated modal criteria that allow for damage detection and localization. This methodology is shown as a flowchart in Figure 2. While this methodology can be implemented on any structure with global damage, this research focuses on a TPS prototype. This TPS prototype is composed of four load-carrying plates bolted to brackets that are bolted to a backing structure.
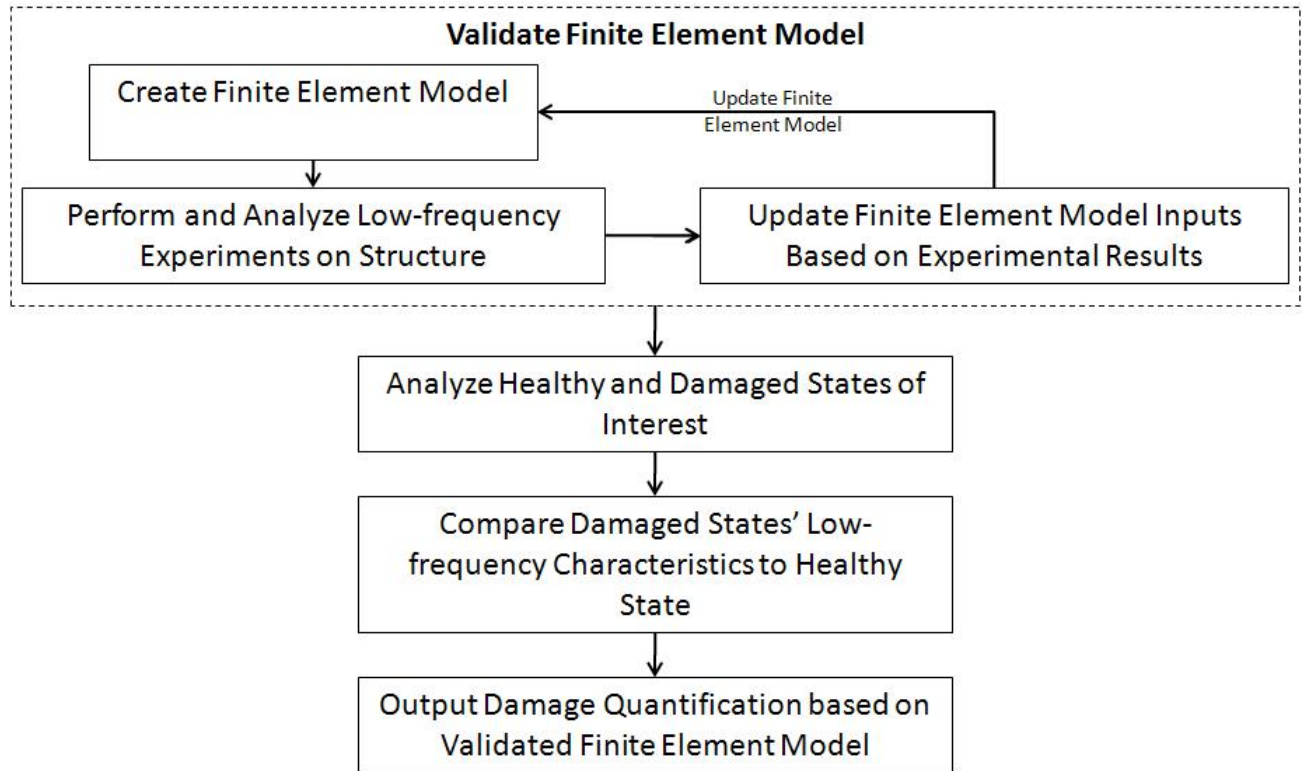
Figure 2: Flowchart of Research Methodology

Chapter 3

METHODS, ASSUMPTIONS, AND PROCEDURES

This chapter provides an overview of the completed research. The research initially focused on sizing optimization to create a structure with improved low-frequency structural dynamics. The goal of the optimized design was to improve damage detection and localization for fastener failure based on changes in natural frequency. Then, the research shifted from designing an optimized structure to focusing on analyzing the current structure. This new research focus began with the creation of a new finite element model to better capture the real-world physics of the structure. This new model is validated with experimental results. This validated model then simulates the fastener failure. The changes in mode shapes caused by the failed fastener(s) are then analyzed to detect and localize damage.

3.1 Thickness Optimization for Damage Detection

This research focuses on developing a methodology that utilizes the finite element method to improve the geometric characteristics of an initial design for damage detection. The improved geometry provides unique characteristics based on the structural health of the system between the healthy and damaged states. The characteristics for SHM could be changes in displacement or stress contours under mechanical loading, changes in fundamental frequencies of the system, or variations in responses to acoustic excitation applied to the system.

Changes in the natural frequency values of a structure due to structural damage will be the focus of this chapter. The structural damage investigated in this research is fastener failure. The fastener
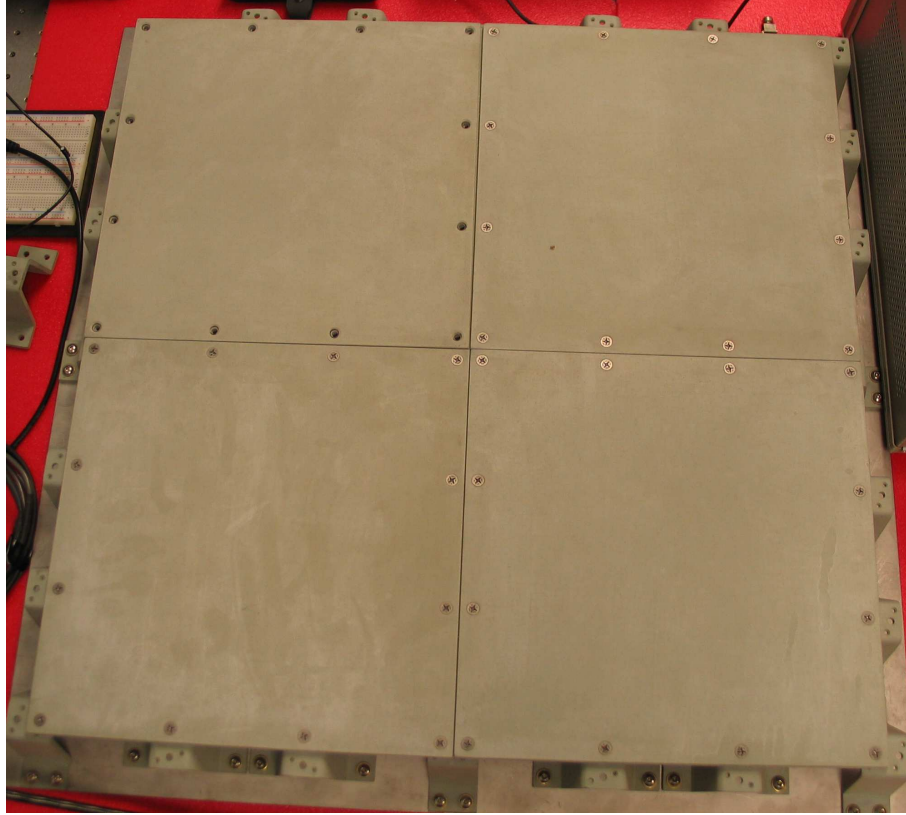
Figure 3: Top View of Physical TPS

failure in this case is a damaged bolt connecting a load-carrying plate to a bracket. Thickness sizing optimization is used to increase the differences between the resonant frequencies of the healthy state and the damaged states. This should increase the likelihood of detecting damage in the investigated structure, especially for symmetric structures where damage does not always result in a noticeable shift between closely grouped resonant frequencies. The objective function for the optimization problem is created using the differences between the natural frequencies of interest. The mode shapes corresponding to the resonant frequencies are investigated to determine the cause of the changes in resonant frequencies between the healthy state and damaged states. A case study for this methodology will be performed based on mechanical fastener failure in a symmetric TPS prototype.

The TPS prototype consists of four one-foot-by-one-foot load-carrying carbon-carbon plates that each contain four removable pieces of insulation. Each of these plates has 12 mechanical

Figure 4: Numbering of Plates and Bolt Locations

Figure 5: Back View of Load-Carrying Plate

Figure 6: Side View of Physical TPS

31

fasteners connecting it to one of the 33 carbon/silicon carbide brackets that are fixed to a backing structure. The mechanically attached carbon-carbon TPS is used on the critical, high-temperature areas of hypersonic vehicles—such as the leading edge—that encounter temperatures too high for blanket insulation. Figure 3 shows a top view of the TPS prototype. The main face of each of the load-carrying plates can be seen in this view. The locations of the four fasteners along each edge of the four load-carrying plates can also be seen. Figure 4 shows the numbering of the 48 fastener locations removed to represent damage in this research. It also numbers each of the load-carrying plates. Figure 4 represents the TPS prototype shown in the same view as Figure 3. Figure 5 shows a close-up of the back side of a load-carrying plate, including the four removable insulation pillows. Figure 6 shows a zoomed in side view of the TPS prototype. The figure shows the composite bracket connected to a load-carrying plate with one fastener at the top of the bracket and to the metal backing structure with two fasteners at each side of the bracket base.

Each damage state investigated in this sizing optimization research is simulated by the removal of a single fastener connecting the top of a bracket to a load-carrying plate, resulting in 48 separate damage states. This physical prototype has been experimented on by the US Air Force Research Laboratory, Air Vehicles Directorate at Wright-Patterson Air Force Base. This portion of the research uses an unvalidated finite element model without the backing structure included to save computational time while obtaining a better understanding of what dynamic properties to investigate further with a newly created finite element model including the backing structure validated with the experimental results obtained at Wright-Patterson Air Force Base.

The initial geometry of the brackets and load-carrying plates are first accurately modeled based on the physical dimensions and material properties of the prototype. The backing structure is not included in the analysis to save computational cost. Each of the four identical load-carrying plates has the large horizontal plate that carries the load on one side and has vertical plates containing the four separate pieces of insulation on the other side (Fig. 5). The finite element model is analyzed in NASTRAN and mode shapes are observed using PATRAN. Each of the one-foot-by-one-foot load-carrying plates is composed of 912 quadrilateral and 80 triangle plate elements. The

insulation is not explicitly represented in the model because it is lightweight and flexible. The insulation contributions are accounted for with scalar springs, which provide additional stiffness in the thickness direction of the load-carrying plates where they are attached. Two types of brackets are present in the system: 32 identical brackets that have two locations for connecting to the load-carrying plates and one large bracket in the center of the structure that has four locations for connecting to the load-carrying plates. The 32 normal supporting brackets are each composed of 200 quadrilateral plate elements, while the large central bracket is composed of 248 quadrilateral elements.

Another key aspect of the finite element model is the bolted locations. Each of the 48 bolts connecting the top plates to the supporting brackets is modeled with a beam element. Also, rigid body elements connect the edges of the bolt holes on the brackets and load-carrying plates to the center of the beam elements. This ensures that the edges of the bolts translate the same distance as the center of the bolts and maintains the original hole shape at the bolt locations. The final aspect of the system which the model must account for is boundary conditions. Since this finite element model does not include the backing structure of the TPS prototype, boundary conditions at the base of the brackets must be properly handled. The boundary conditions are taken to be fixed at each of the four bolt locations at the base of the supporting bracket. This initial design is symmetric about the x- and y-axes based on the geometry of the physical structure. Two important views of the finite element model used for the initial design are shown in Figures 7-9. Figure 7 shows the finite element model from the same view as Figure 3. Figure 8 shows one of the 32 identical brackets in the TPS. Figure 9 shows the side view of the TPS model.

After the model is properly set up, the healthy and damaged states must be defined. The healthy state is defined as the case where each of the 48 bolts connecting a load-carrying plate to a supporting bracket is healthy (the bolt is within its proper torque range). Each damage state investigated in this thickness optimization section is defined as a single fastener failure between a load-carrying plate and supporting bracket (as seen in Figs. 3 and 4), which creates 48 unique damage states. While damage definition in this section does not capture multiple bolts failing at

33
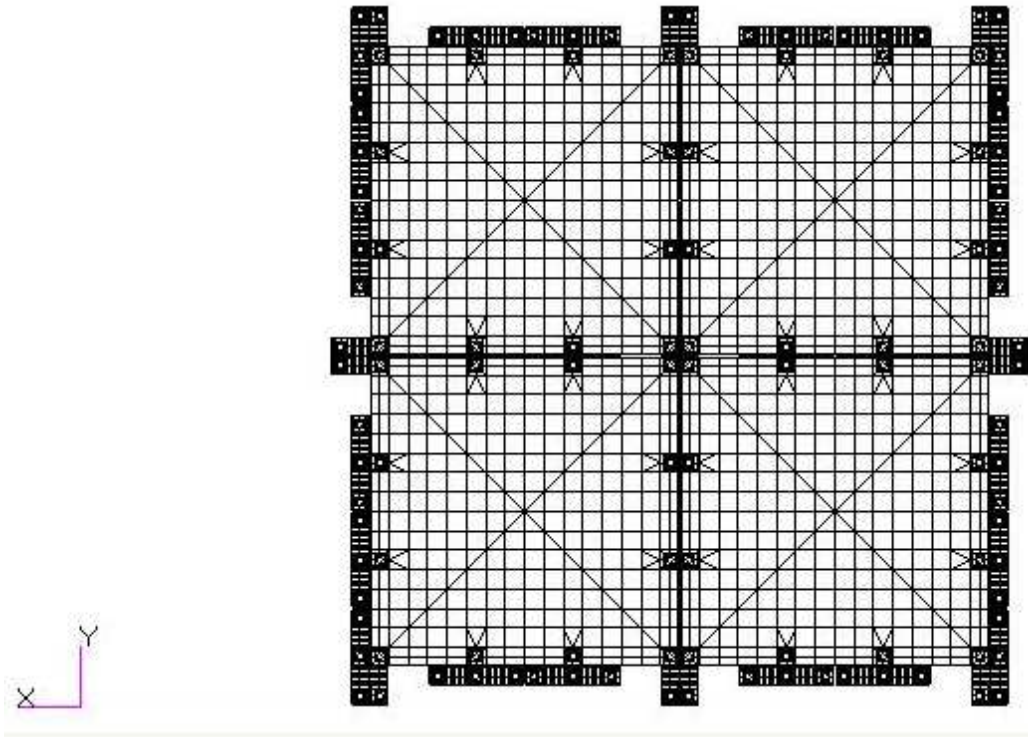
Figure 7: Top View of Finite Element Model
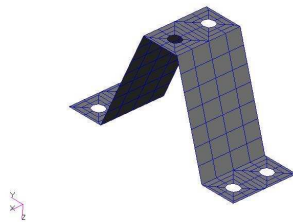
Figure 8: Single Bracket in Finite Element Model
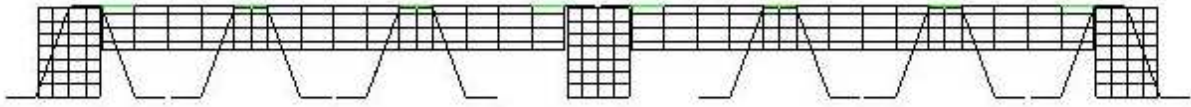
Figure 9: Side View of Finite Element Model

the same time, the high-level damage level mentioned in section 3.3 contains multiple fastener failures at the same time. These multiple fastener failings are not considered in this section since they would vastly increase the possible number of damage states required for calculation of the objective function. For simplicity, the damaged fastener is modeled by removing the beam element at the specified damage location.

3.1.1 Design Problem Formulation

Previous research by McClung [145] demonstrated how optimizing the geometry of a single plate fixed by fasteners at the corners could improve a design for SHM. Designing for SHM is accomplished by picking a design that causes differences between the natural frequencies of the healthy state and the natural frequencies of the damaged state. The increase in the frequency shift resulting from damage makes it easier for an automated system to detect damage independent of human judgment. Each damage states in this past research was a failed fastener at one of the plate corners.

This research investigates using an optimization method to increase the natural frequency differences between the predefined healthy and damaged states for a more complex geometry of a composite structure. The modified method of feasible directions is used to optimize the geometry of the stated problem to enable effective SHM. Since damage quantification is being realized by

35

observing frequency changes between healthy and damaged states of a TPS, the objective function is formulated to increase the difference between the natural frequencies of interest in both the healthy and damaged states. Each of the design variables—thicknesses of portions of the TPS—is constrained by upper and lower bounds to ensure a physically feasible design while maintaining a reasonable system mass. These bounds allow the thicknesses in the design to range between 50% from the initial value of the design variable to one-quarter inch to allow a wide number of possible solutions. The system input x_i is the thicknesses of elements entered throughout the model based on the geometry of the system. The obtained output is the numerically calculated natural frequencies of the system.

The output is utilized so that two separate objective functions (Equations (16) and (17)) can be utilized, depending on how the current model is behaving. If the current model has closely grouped natural frequencies in the healthy state, the objective function used is the product of the first nine differences between consecutive natural frequencies (Equation (16)). The first nine frequency differences were chosen because they provide a significant amount of data to allow for SHM that are accurately modeled. If sufficient differences exist between the consecutive natural frequencies to be physically distinguishable from each other (designated as a difference of at least 2.0 Hz) in the healthy state, the objective function is the product of the difference between the natural frequencies of the healthy and damaged states of interest (Equation (17)). A product of frequency differences was chosen instead of a summation since summation causes each frequency difference to have the same sensitivity for all design iterations. Using a product of frequency differences causes the greatest sensitivity of the objective function to result for the smallest of the frequency differences—resulting in small frequency differences being the driving force for each iteration. This allows relatively small frequency differences to be more likely to increase than relatively large frequency differences. For example, if one frequency difference is 0.50 Hz while the other frequency differences are each 3.00 Hz, the objective function is more sensitive to the frequency difference of 0.50 Hz, making it the driving force for the iteration. This objective functions use only the first 10 natural frequencies of the system since they are most accurate frequencies captured

in the finite element model and allow for sufficient differences between the healthy and damaged states to be observed; this number can be easily increased or decreased depending on the designer's preferences.

$$F_1(x_1, x_2, \cdots, x_n) = f_{2-1}f_{3-2}f_{4-3} \cdots f_{10-9} \tag{16}$$

$$0.5\mathrm{x}_{j0} \leq x_j \leq 0.25"$$

$$F_2(x_1, x_2, \cdots, x_n) = \prod_k \left[(f_{1H} - f_{1D^{(k)}})(f_{2H} - f_{2D^{(k)}}) \cdots (f_{10H} - f_{10D^{(k)}}) \right] \tag{17}$$

$$0.5\mathrm{x}_{j0} \leq x_j \leq 0.25"$$

The variables listed in Equations 16 and 17 are defined as the following: x_{j0} is the initial point for design variable x_j, F_1 and F_2 are the objective functions for the optimization problem, f_{m-n} is equal to healthy natural frequency m minus healthy natural frequency n, f_{iH} is the ith natural frequency of the healthy state, and $f_{iD^{(k)}}$ is the ith natural frequency of the kth damage state.

Before the design optimization begins, the natural frequencies and corresponding mode shapes are found (first for the healthy state and then for the 48 independent damage states). This provides a baseline for the frequency differentiation between each mode and between the healthy and damaged states. The goal of the optimization process will be to improve upon these baseline values. The following terminology will be used to distinguish between the four load-carrying plates for mode shape descriptions: Plate 1 is the load-carrying plate in the positive x- and y-plane, Plate 2 is the load-carrying plate in the negative x- and positive y-plane, Plate 3 is the load-carrying plate in the negative x- and y-plane, and Plate 4 is the plate in the positive x- and negative y-plane. The symmetry conditions mentioned are with respect to the global x- and y-axes (with the origin at the center of the four load-carrying plates) and local x- and y-axes (defined from the center of each plate). The local mode symmetry conditions are defined for when each load-carrying plate bends

in more than one direction at a time (out-of-plane in each direction with nodes lying along the defined local axes). The first four mode shapes show no local symmetry since they bend in one direction only.

Two groups of design variables were chosen for sizing optimization: a four-design-variable problem that maintained and global symmetry, and a nine-design-variable problem that allowed for asymmetric global designs. The four-design-variable problem contained the following variables: two thicknesses for the horizontal portion of the load-carrying plates (x_1 around the edges and x_2 composed of the middle area), one variable for thickness of the vertical portion of the load-carrying plates that hold the insulation (x_3), and one for thickness of the brackets (x_4). Each of these design variables begins with the deterministic value assigned in the original model. Since the thicknesses chosen for the load-carrying plates are locally symmetric, the overall system symmetry is maintained for any selected variables in this case. This nine-design-variables problem defined the following design variables: two for each of the four load-carrying plates (one for the horizontal face thickness—x_1, x_3, x_5, x_7—and one for the thickness of the vertical faces which hold the insulation—x_2, x_4, x_6, x_8) and one for thickness of all brackets x_9. Since each of the plates have independent design variables, design flexibility is greatly increased and global symmetry is no longer required. The outputs and objective function from the four-design-variable problem are used in this nine-design-variable problem also. The results for the initial TPS prototype, the four-design-variable optimization problem, and the nine-design-variable optimization problem are all presented in Section 4.1.

3.2   Finite Element Model Validation

3.2.1   Model Creation

The three important factors in calculating frequency results using finite element analysis: geometry, boundary conditions, and material properties. The dimensions of the geometry were taken directly from physical measurements of the composite plates, brackets, and backing structure used during the experimental dynamic analysis. Digital calipers provided measurements within one-

thousandth of an inch for plate thicknesses; larger dimensions were measured with rulers within one-sixteenth of an inch. For each length and thickness, the dimension was measured at multiple locations and averaged to reduce the amount of error that occurs due to slight geometric variations throughout the manufactured parts. Then, these precise measurements were used to create a 3-D model using S4R elements (4-noded shell elements that use reduced integration) in ABAQUS CAE [146]. These elements were chosen since the parts' relatively small thicknesses compared to their length and width make a 3D mesh much more time-consuming. Therefore, the model generated using ABAQUS CAE is geometrically very similar to the physical plate, relatively efficient, and has minimal error due to the geometric properties.

Also, a mesh convergence study was completed to ensure that the mesh was properly refined for accuracy while keeping the time required for analyses to a minimum. The mesh convergence study, the utilized identical geometric dimensions, steel material properties, types of finite elements, and free-free boundary conditions and varied only the number of nodes used to mesh the plate. This mesh convergence study found that a single load-carrying plate with 5188 nodes had a maximum percent difference of 0.651% for the first five natural frequencies compared to a mesh using 20,409 nodes. Since the maximum frequency change is under 1% when the nodes were increased over 250%, the 5188 node mesh is used in the future analyses since it shows good agreement with a much higher refined mesh while requiring significantly less computational time. Extending the same mesh generation sizing to the entire assembly resulted in a finite element model with 39,855 nodes and 36,104 elements.

The second important aspect of the finite element model is the boundary conditions. Since the experiments used free-free boundary conditions, no boundary conditions were implemented on the finite element model. This free-free finite element formulation provides six rigid body modes (corresponding to the three free translational and three free rotational degrees of freedom) which occur at very low frequencies and do not have any physical relevance to the verification process being completed. After the rigid body modes, the finite element analysis outputs the numerically obtained natural frequencies.

Table 1: Carbon-Carbon Material Properties

Material Properties	E_1 (Msi)	E_2 (Msi)	Poisson's Ratio	Density (lb/in^3)
Minimum	11.761	12.06	0.308	5.9478E-02
Maximum	12.46	12.38	0.358	6.0498E-02
Average	12.07	12.23	0.324	6.0095E-02
Standard Deviation	0.31	0.11	0.021	3.7675E-04

The third modeling aspect is material properties. A deterministic material model was used to define the quasi-isotropic for the composite materials in the structure using ABAQUS's linearly elastic lamina material model. The manufacturer of the composite plates and brackets provided experimental data showing experimental data collected to determine the material properties. The experimental data provided both an initial deterministic value (the experimental average) and an acceptable range of values for the material properties for updating of the finite element model versus experimental results. These carbon-carbon material properties can be seen in Table 1. The average values were used as the starting point in the inverse optimization of the material properties with the upper and lower boundaries being the maximum and minimum values. Since the material is assumed to be quasi-isotropic, the Young's modulus values are taken to be bounded between 11.761 and 12.46 Msi with an initial value of 12.15 Msi—the minimum, maximum, and average found for the combined E_1 and E_2 variables in Table 1. The insulation has been modeled in ABAQUS as nonstructural mass distributed over the load-carrying plates.

Three different finite element models were created to match the three aforementioned experimental setups. The first incorporates a single load-carrying plate without the nonstructural mass elements. The second includes the nonstructural mass elements on a single load-carrying plate to account for insulation effects. These single load-carrying plate finite element models can be seen in Figures 10 and 11. The third model includes the entire structure of four load-carrying plates, 33 brackets, and the backing structure. All of the bolted locations are modeled using rigid body elements that connect two separate parts. An unmeshed view of this finite element model can be seen in Figure 12.
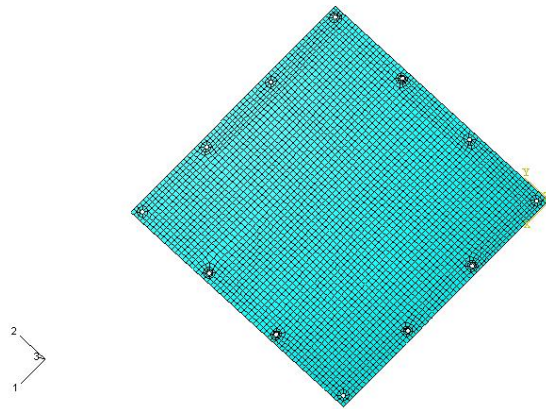
Figure 10: Front View of Single Finite Element Model Plate
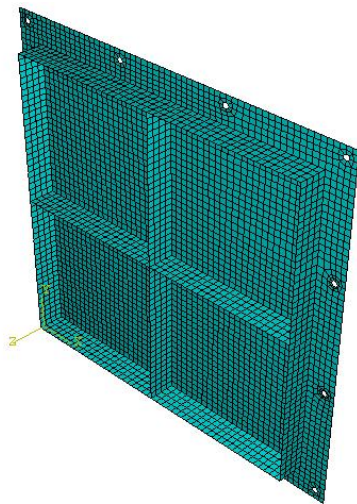
Figure 11: Back View of Single Finite Element Model Plate
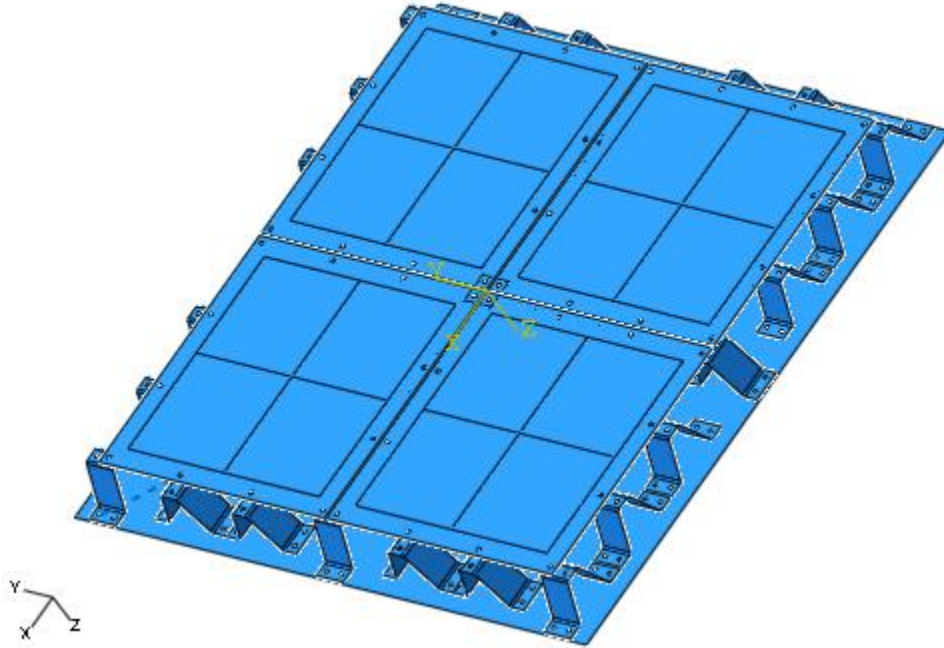
Figure 12: Unmeshed Finite Element Model of Entire TPS

3.2.2 Physical Experimentation

The experimentally tested structure investigated is shown in Figures 3-6. This structure consists of four one-foot-by-one-foot C-C load-carrying plates. Each of the load-carrying plates had a ribbed design to contain insulation (Fig. 5) on its back side. Also, each load-carrying plate is connected to a thin backing sheet of steel by composite brackets with steel fasteners. Three sets of experimental data were collected: one C-C load-carrying plate without insulation, one C-C load-carrying plate with insulation, and the entire structure. This allows the finite element variables (material properties, insulation effects, and bolted boundary conditions) to be observed on multiple levels.

Frequency response functions (FRFs) were experimentally obtained with Spectral Dynamic's SigLab software for each of the three experimental setups. Each of the FRFs used Boxcar windowing and five averages to obtain the dynamic characteristics of the composite plate from 0 to 2000 Hz. An array of three single axis tear drop accelerometers was shifted through a predefined grid to allow for both natural frequency and mode shape extraction from the experimental results.

42

The system was excited with an impulse hammer striking the plate at the same impact location (approximately 2.25 inches and 3.75 inches away from the load-carrying plate edges closest to the hole the plate is hung from with a thin wire). The thin wire used to hang the plate for experimentation should add a minimal amount of stiffness to the problem to closely represent the boundary conditions used in the finite element model. Each instance of data collection consisted gathering the FRFs at three of the predefined grid locations due to an impulse hammer striking the structure at the same location. For each of the instances, the impact location and the free-free boundary conditions are the same; the only variation is in the location of the accelerometers obtaining the FRFs.

After all of the FRFs were experimentally obtained, they were used to obtain the results for the values of the first several natural frequencies. Since FRFs are available at each of the sensing locations, a deterministic result for the natural frequencies is not available. Instead, the natural frequencies are extracted from each of the FRFs to create a distribution of the natural frequencies. For each of the frequency peaks of interest in the FRF, a single degree of freedom curve fit technique is used to extract the natural frequency. This takes the digital results and fits a curve to best fill in the location surrounding the data points to obtain a more accurate estimation of the natural frequency. Each natural frequency has a corresponding mode shape based on how the FRF varies throughout the composite plate. Since each of the natural frequencies have node locations associated with very low excitation, the grid locations close to these unexcited areas are ignored for determining that natural frequency from the experimental results.

The first experimental setup isolates a single load-carrying plate without insulation. The plate is hung in a free-free state (Fig. 13) so no insulation effects or bolted conditions influence the experimental results. For the first experimental setup, a predefined nine-by-nine grid was created on the flat one-foot-by-one-foot face of a single ribbed C-C thermal protection plate without backing insulation. This provides 81 FRFs to be used for the low-frequency characterization of the composite plate. Similarly, the second experimental setup uses the same boundary conditions, impact location, and grid locations as the first experimental setup. The only difference between the two
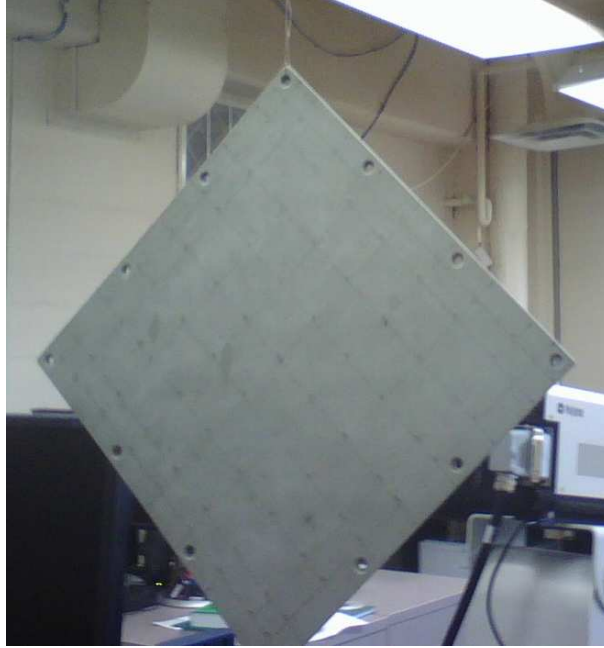
Figure 13: Experimental Layout of a Single Composite Plate

experimental setups is the addition of the insulation to the load-carrying plate. This shows how much additional damping is introduced with the addition of the nonstructural mass.

The third experimental setup is of the entire four-plate structure. Each of the load-carrying plates has the insulation included and is connected to the backing structure with brackets at each of its 12 holes. The bolts connecting the load-carrying plates to the brackets and the brackets to the backing structure are all in their healthy state. The structure is hung in a free-free state from a hole drilled through the backing structure (Fig. 14). The grid used for accelerometer placement for the entire structure is an equally spaced 7 by 7 on each of the four plates. This results in a total of 196 accelerometer locations for this experimental setup. The impulse hammer was once again used to excite the system at the same location as the single plate experiments on the plate closest to the hole from which the structure is hung.

3.3   Modal-based Damage Detection

Damage detection of the four plate C-C TPS has been computationally performed. The finite element model used throughout the damage detection process has the geometry and material prop-

Figure 14: Experimental Layout of Entire TPS

Figure 15: Numbering of Plates and Bolt Locations

erties obtained during the finite element model validation. However, the validated ABAQUS finite element model has fixed boundary conditions along the edges of the backing structure to simulate how the actual backing structure would behave on a flight vehicle. Since this research focuses on detecting fastener damage in a structure, the sets of damage states for the problem must be defined before damage characterization can be completed. This research arbitrarily chose two damage sets: high-level damage and low-level damage. The high-level damage set—composed of the four fasteners along one edge of a load-carrying plate being damaged—provides a scenario where the low-frequency dynamic changes should allow for damage detection and localization to show the feasibility of the developed methodology. Then, the low-level damage set—composed of a single fastener on a load-carrying plate being damaged—is investigated as a more difficult, real-world case.

3.3.1 Damage State Definition

The numbering of the plates and bolts follows the numbering pattern shown in Fig. 15. Figure 15 represents the physical TPS structure from its top view (as seen in Fig. 3). Each of the damage cases investigated in the high-level damage set consists of the four bolts along one edge of a load-carrying plate to be severely damaged (for example, removing bolts 1, 2, 3, and 4 and removing bolts 7, 8, 9, and 10 are each high-level damage cases); this results in 16 damage states due to the geometry of the system. Each low-level damage state consists of severe damage to an individual bolt connecting a load-carrying plate to its supporting bracket, resulting in 48 damage states.

46

As mentioned earlier, the low-frequency dynamics were investigated due to changes in the mode shapes for the first several natural frequencies. While the mode shape changes were investigated up to the seventh natural frequency, the most significant changes occurred for the second and third mode shapes. Therefore, these are the results which will be presented.

3.3.2 Low-frequency Damage Metrics

The mode shape properties that are used in this study are the MAC [73], PMAC [73, 75], and COMAC [147, 148]. These modal characteristics were chosen since they have less sensitivity to environmental changes than the resonant frequencies. Other mode shape characteristics that focus on the first derivative or second derivative of the mode shape were not investigated since they would require more data points for high-accuracy results. This would result in additional sensor placements being required for any experimentation.

3.3.2.1 Modal Assurance Criterion (MAC)

The MAC provides a correlation between the mode shapes of interest. This comparison can be between experimental and finite element results for model validation or between two separate finite element analyses/experimental results to demonstrate the similarity between the mode shapes. The MAC between two separate cases of finite elements (a healthy state and a damaged state) is used for the numerical damage detection. The formula for the MAC used in this instance is shown in Eq.18 [73]:

$$MAC = \frac{\{\phi_h\}^H \{\phi_d\} \{\phi_h\}^H \{\phi_d\}}{\{\phi_h\}^H \{\phi_h\} \{\phi_d\}^H \{\phi_d\}} \tag{18}$$

where $\{\phi_d\}$ is the normalized modal vector for the damaged finite element model, $\{\phi_h\}$ is the normalized modal vector for the healthy finite element model, and $\{\phi\}^H$ is the complex conjugate transpose of the mode shape. The formulation of the MAC results in values ranging from zero to one. For similar eigenvectors, the correlation is high, so the MAC will be relatively close to one. For less similar eigenvectors, the correlation is lower, so the MAC will be close to zero. Since the MAC is a correlation between the global mode shapes, it is better at showing when damage

is present than at localizing damage. When comparing two series of modal vectors, one MAC is calculated between each modal vector of each series. For example, if n modal vectors exist for a damaged state and a healthy state, n^2 MAC values are calculated. They are typically output in a matrix with n rows and n columns.

3.3.2.2 Partial Modal Assurance Criterion (PMAC)

In addition to the standard MAC, the PMAC will be used to detect damage location. The PMAC is calculated using the same formula as the MAC, but instead of utilizing all of the points in the modal vectors, a reduced modal vector that correlates to specific portions of the structure is used; therefore, the PMAC demonstrates how specific parts of the structure's mode shape correlate to each other, rather than the correlation of the entire structure [73, 75]. For this research, the PMAC regions are chosen to aid in damage localization. Since identifying the plate containing the damaged bolt(s) is desired, each of the load-carrying plates is separated into a region for PMAC calculation. The region containing the lowest PMAC should be on the load-carrying plate containing the damage.

3.3.2.3 Coordinate Modal Assurance Criterion (COMAC)

The COMAC attempts to measure which degrees-of-freedom contribute to a low MAC. This is beneficial for damage detection since the degrees-of-freedom with a high COMAC are likely to be located close to the damage. This method takes modal vector pairs of interest between the two states and calculates a COMAC value for each degree-of-freedom. Before calculating the COMAC, the MAC is computed for the modal vectors of interest to ensure they are properly paired. The MAC values are entered into a MAC matrix. If a mode switch occurs due to the presence of damage, the damaged modal vectors must be renumbered to ensure they correspond to the correct healthy modal vector. This modal vector renumbering is completed by observing a matrix composed of the MAC between the modal vectors of interest. When the off-diagonal terms of the MAC matrix between two modal vectors show a much higher correlation between them than

the diagonal terms do, a mode switch has occurred. This requires the modes to be renumbered (for example, modes 1, 2, 3, 4 become modes 1, 3, 2, 4 due to a mode switch between the second and third modes) for proper calculation of the COMAC. The COMAC is calculated using Equation 19 [147, 148]:

$$COMAC(j) = \frac{\left(\sum \left| (\phi_h)_{jl} (\phi_d)^*_{jl} \right| \right)^2}{\sum \left| (\phi_h)_{jl} \right|^2 \sum \left| (\phi_d)_{jl} \right|^2} \tag{19}$$

where $(\phi_h)_{jl}$ and $(\phi_d)_{jl}$ are the healthy and damaged modal vectors at degree-of-freedom j and mode l, $(\phi_d)^*_{jl}$ is the complex conjugate of the damaged modal vector, and each summation is for $j = 1$ to L (the number of modal vectors being used in the COMAC calculation).

The COMAC value will be between zero and one. COMAC values close to one show the coordinate having a minimal negative effect on the MAC value for the mode shapes used. Low COMAC values demonstrate the coordinate being a large contributor to the lower MAC value for the mode shapes used. Before completing the damage characterization, the damage levels and nodal locations must be determined to enable the analyses and calculations. The damage levels have already been defined for both the high-level and low-level damage cases. The nodal locations should be chosen to allow for enough data points to properly show mode shape correlation without choosing an unrealistic number of locations for comparison to experimental results. Therefore, the computational damage assessment was done completed with the same equally-spaced seven-by-seven grid on each of the load-carrying plates used during experimentation on the assembly, resulting in 196 node locations.

3.3.2.4 Normalized Coordinate Modal Assurance Criterion (NOCOMAC) and Normalized Coordinate Modal Assurance Criterion Summation (NOCOMACSUM)

This section describes the formulation of two new damage metrics based on mode shape normalization. The basic theory is that if two mode shapes are identical, no difference exists between any of the mode shape's nodal values independent of the normalization used. However, when a mode shape changes, differences will occur between the corresponding nodal values of the two

49

mode shapes. The areas with the most significant differences between the two mode shapes will typically have the biggest differences after normalizing both mode shapes to the same node. Since changes in mode shapes for fastener failure should have the largest changes close to the damage location, the locations of the largest differences for the normalization across the nodal locations for each correlated mode shape is the first new damage metric, which will be called the normalized coordinate modal assurance criterion, or NOCOMAC ($n\bar{o}c\bar{o}mac$). The second damage metric, the normalized coordinate modal assurance criterion summation, or NOCOMACSUM ($n\bar{o}c\bar{o}macs\breve{u}m$), takes the summation of the values used to calculate the NOCOMAC to create one vector containing all of the modal difference information, rather than just the maximum modal difference for each point. While comparing two mode shapes would typically provide only one location for damage (the location with the largest difference between the two mode shapes), a damage distribution is created to demonstrate the area(s) most likely close to the damage based on normalizing the mode shapes at each nodal point.

The methodology behind the calculation of these damage metrics from the healthy and damaged modal vectors is shown in Figure 16. The first step in calculating the two damage metrics is to calculate the normalized coordinate difference, or NOCODIFF ($n\bar{o}c\bar{o}dif$). The NOCODIFF is calculated using Equation 20 for each combination of an individual degree-of-freedom n and mode shape m. Calculating the NOCODIFF begins by taking the difference between the healthy and damaged modal vectors after they are normalized to each node and correlated mode, resulting in $m*n$ vectors. The square root of the square of the normalized differences is taken individually for each element to ensure that all of the terms in each NOCODIFF vector are positive.

$$NOCODIFF_{m,n} = \sqrt{\left(\frac{\phi_h}{(\phi_h)_{nm}} - \frac{\phi_d}{(\phi_d)_{nm}} \right)^2} \tag{20}$$

where ϕ_h is the healthy mode shape, ϕ_d is the damaged mode shape normalized, n is each nodal location, m is each correlated modal vector.

The second step is to normalize each NOCODIFF vector by its largest magnitude term, re-
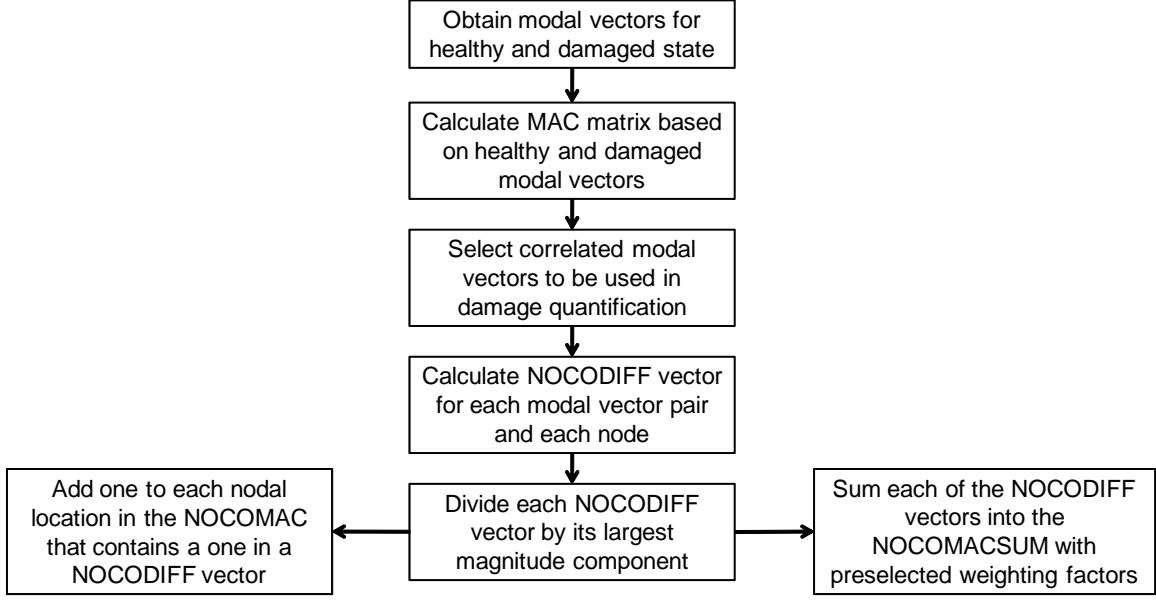
Figure 16: Flowchart for NOCOMAC and NOCOMACSUM Calculation

sulting in $m*n$ vectors ranging from 0.0 to 1.0. The NOCOMAC retains information only on the nodal location containing the maximum value in each of the NOCODIFF vectors (the nodal locations containing 1.0 after the NOCODIFF normalization). The NOCOMAC begins as a 1 x n zero vector. For each instance where the nodal location contains the greatest value in a NOCODIFF vector, 1.0 is added to the corresponding nodal location in the NOCOMAC vector. The NOCOMAC vector can be used to investigate the damage prediction level for each individual mode as well as the total using all data. The terms in the total NOCOMAC vector will sum to $m*n$ (assuming they are complex enough not to encounter multiple equivalent maximums in the same NOCODIFF vector, which would increase the total). The nodal locations containing the highest values in the NOCOMAC are predicted to be close to the damage, based on the underlying assumption that the largest differences between healthy and damaged mode shapes occur close to the damage.

The NOCOMACSUM provides a weighted sum vector (1 x n) based on the normalized NOCODIFF vectors. The NOCOMACSUM is calculated using Equation 21, which shows the normalization of the NOCODIFF to ensure a range from 0.0 to 1.0 for each term in each NOCODIFF vector.

$$NOCOMACSUM = \sum_m \sum_n \left(w_m w_n \left(\frac{NOCODIFF_{m,n}}{Max(NOCODIFF_{m,n})} \right) \right) \qquad (21)$$

51

where w_m is the mode weight, and w_n is the node weight.

The nodes close to the global damage are predicted to have higher values than the nodes far away from the global damage. The NOCOMACSUM allows for user knowledge to be incorporated into the calculation with two weighting factors, w_m for mode weighting and w_n for node weighting. The weighting terms can be set to one (recommended unless some outside knowledge of the problem exists), or shifted throughout the modes and/or nodes being used to increase or decrease the contribution of certain terms to the NOCOMACSUM. Mode weighting can be adjusted to correspond either to the MAC, the inverse of the MAC (1/MAC), or independent of the MAC. Node weighting can be selected to make the contribution of certain areas (individual plates, edges, interior nodes) more or less significant than other areas. A decreased nodal weight decreases the normalized nodal contributions corresponding to the nodes with the reduced weight. The locations closest to the global damage should have higher NOCOMACSUM values than locations farther from the damage. The node with the greatest damage value is predicted to be located closest to the damage.

<center>Chapter 4</center>

<center>**RESULTS AND DISCUSSION**</center>

This chapter reviews the results of the aforementioned research. It begins with the results for the four-design-variable and nine-design-variable optimization problems. Then, it reviews the model updating used for model validation. The results for the damage detection (both high-level and low-level) based on changes to the mode shapes from the validated finite element model are then covered.

4.1 Thickness Optimization for Damage Detection Results

4.1.1 Initial Resonant Frequency Results

As Table 2 shows, the natural frequencies are numerically grouped into the first four, the next four (frequencies five through eight), the following four, and so on. This is most likely due to the geometric symmetry of the system. The mode shapes corresponding to the first five natural frequencies are shown in Figures 17-21. The mode shapes of the first group of four natural frequencies show similar bending characteristics with changes in the global and local symmetry. While these numerical results for the first four mode shapes properly demonstrate the expected symmetry of the problem, these four mode shapes would be physically indistinguishable from each other due to their closely grouped numerical frequencies. For example, if this initial system is excited at 800 Hz, each of the mode shapes will simultaneously be excited—resulting in a combined mode shape instead of four unique mode shapes. Therefore, the natural frequencies for the healthy mode shapes are first separated from each other during the design process by using Equation (16).

<center>53</center>

Table 2: Natural Frequencies of Healthy TPS Finite Element Model

Frequency Number	Frequency (Hz)	Mode Shape Description
1	799.32	Symmetric about both axes; Magnitude equal on all plates
2	799.59	Symmetric about y-axis; Antisymmetric about x-axis; Slightly higher magnitude on plates 2 and 4
3	799.60	Symmetric about x-axis; Antisymmetric about y-axis; Slightly higher magnitude on plates 1 and 3
4	799.88	Antisymmetric about both axes; Magnitude equal on all plates
5	1144.9	Globally symmetric about both axes; Locally antisymmetric; Magnitudes slightly higher on Plates 2 and 3
6	1144.9	Globally symmetric about x-axis and antisymmetric about y-axes; Locally antisymmetric; Magnitudes slightly higher on Plates 1 and 4
7	1145.0	Globally antisymmetric about x-axis and symmetric about y-axes; Locally antisymmetric; Magnitudes equal on all plates
8	1145.4	Globally and Locally antisymmetric; Magnitudes equal on all plates
9	1187.1	Globally symmetric about x-axis and antisymmetric about y-axis; Locally symmetric; Magnitudes equal on all plates
10	1189.6	Globally antisymmetric about x-axis and symmetric about y-axis; Locally symmetric; Magnitudes equal on all plates
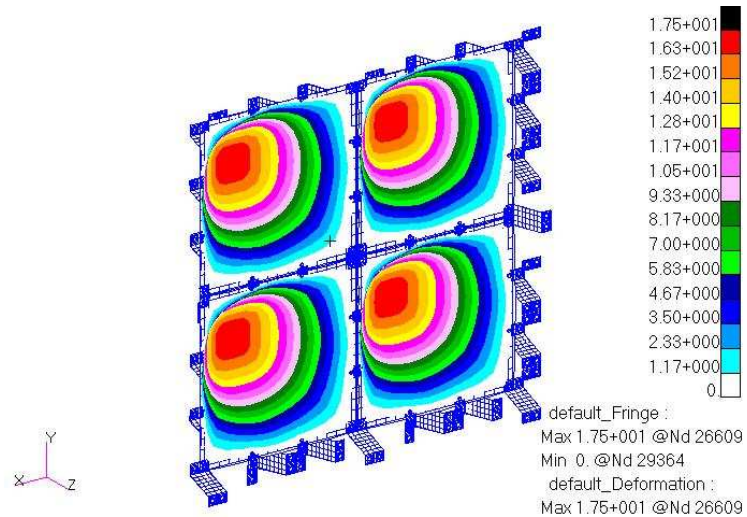
Figure 17: First Mode Shape for Healthy Starting Design
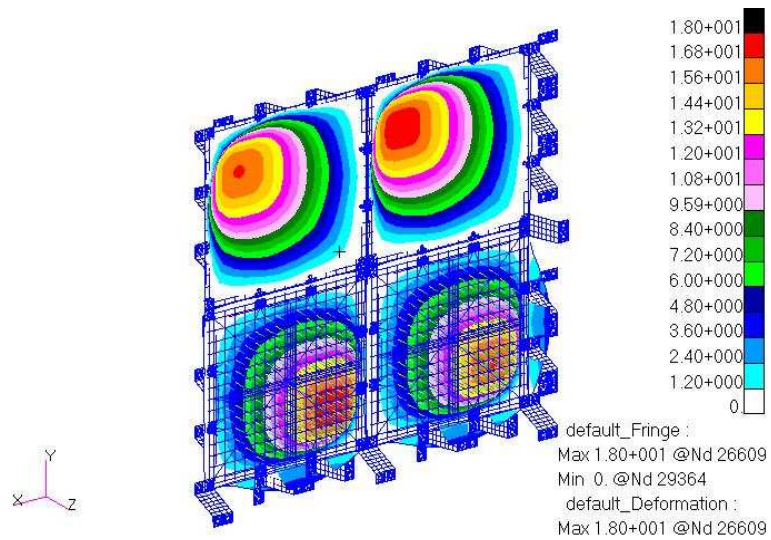
Figure 18: Second Mode Shape for Healthy Starting Design
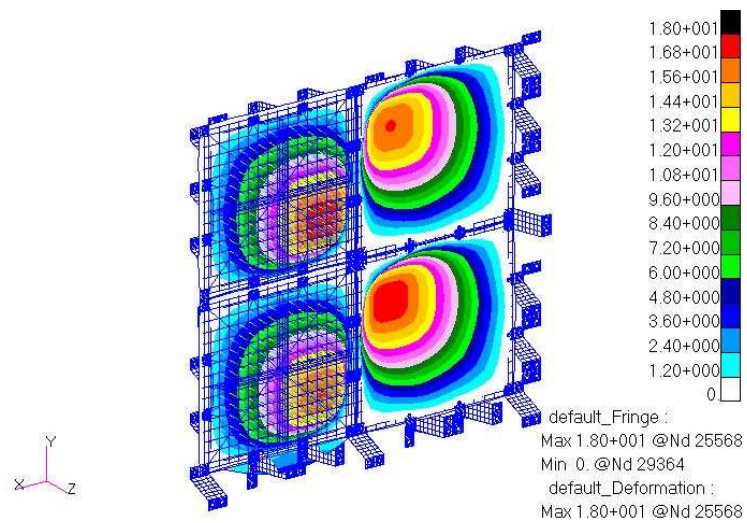
Figure 19: Third Mode Shape for Healthy Starting Design
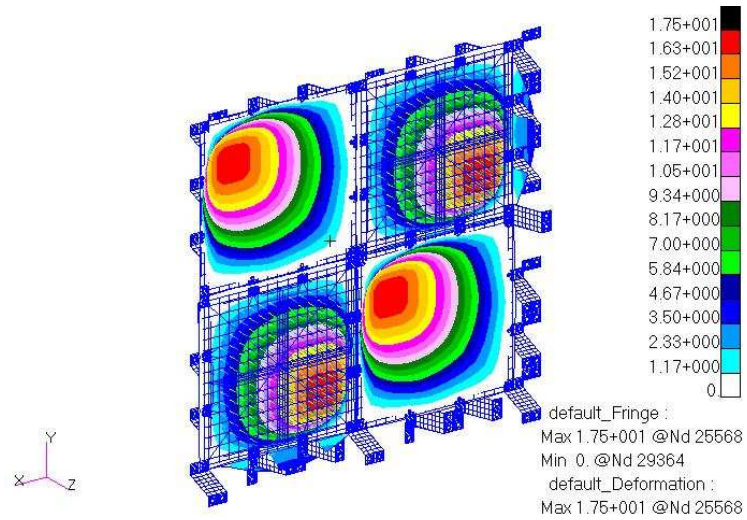
Figure 20: Fourth Mode Shape for Healthy Starting Design
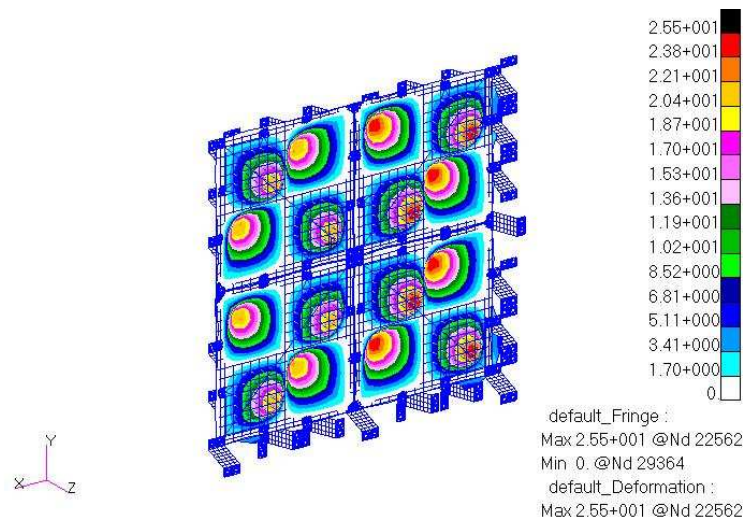
Figure 21: Fifth Mode Shape for Healthy Starting Design

After the natural frequencies and mode shapes were determined for the healthy finite element model, the natural frequencies and mode shapes for each of the 48 damaged states were found individually. Examination and comparison of the 48 damage states of interest determined using the finite element model showed the damage states falling into two separate categories based on the location of the fastener on the load-carrying plate. The 32 fasteners located along the sides of the load-carrying plates (two on each of the four edges for each of the four load-carrying plates) demonstrated both a noticeable frequency change and a changed mode shape. The natural frequencies and mode shapes change for many of the numerically obtained results due to the lack of system symmetry and reduction in system stiffness.

For simplicity, only the changes to the first natural frequency and its corresponding mode shape since it sufficiently distinguishes between the healthy and damaged states. The first fundamental frequency decreases approximately 10 Hz from the healthy state to the damaged state. Also, the corresponding first mode shape is no longer symmetric—the plate with the removed fastener has bending while the other plates remain stationary. Figure 18 shows the first mode shape resulting in out-of-plane bending of only the plate with the side damaged fastener.

The remaining 16 damage states each had very similar results based on which plate was fastened by the damaged bolt. The missing bolts for these damage states were located at the corners of the load-carrying plates (four corner bolts for each of the four plates). The ease of damage quantification for these cases was not as distinct as the other 32 damage states. The natural frequencies showed no significant change (the first natural frequency reduced less than one Hz from the healthy state). However, these numerically found mode shapes did show changes that would be observable in a laboratory. For example, the first mode shape of the system (Fig. 23) results in the plate with the fastener damage having an increased magnitude of bending compared to the other plates. While having only the magnitude of the load-carrying plates' bending is not an ideal scenario, the maximum magnitude of the plate missing the fastener is approximately 70% more than the two closest neighboring load-carrying plates and over 110% more than the remaining load-carrying plate. When acoustically exciting the structure in the laboratory, each of the first four
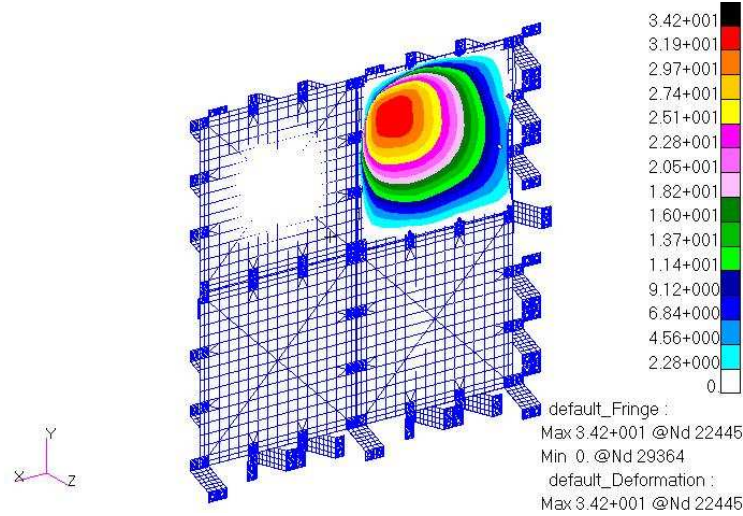
Figure 22: First Mode Shape for One of the Damaged Side Bolts on Upper Right Plate

natural frequencies would be excited simultaneously, resulting in a combined mode shape instead of four distinct mode shapes. Therefore, the initial finite element model of the prototype shows some potential for SHM, but the results most likely would be difficult to repeat in a laboratory due to the close numerical grouping of the first four natural frequencies. This demonstrates one undesired result (unobservable corner fastener damage states) that can potentially occur. Designing the structure for SHM would reduce the likelihood of unobservable damage states appearing in the final design.

4.1.2 Four-Design-Variable Results

The first attempt to improve the frequency characteristics of the healthy system was completed using four design variables: two thicknesses for the horizontal portion of the load-carrying plates (x_1 around the edges and x_2 composed of the middle area), one variable for thickness of the vertical portion of the load-carrying plates that hold the insulation (x_3), and one for thickness of the brackets (x_4). Each of these design variables begins with the deterministic value assigned in the original model. Since the thicknesses chosen for the load-carrying plates are locally symmetric, the overall system symmetry is maintained for any selected variables in this case.

While this problem quickly converged to a solution, the provided solution is not useful. The
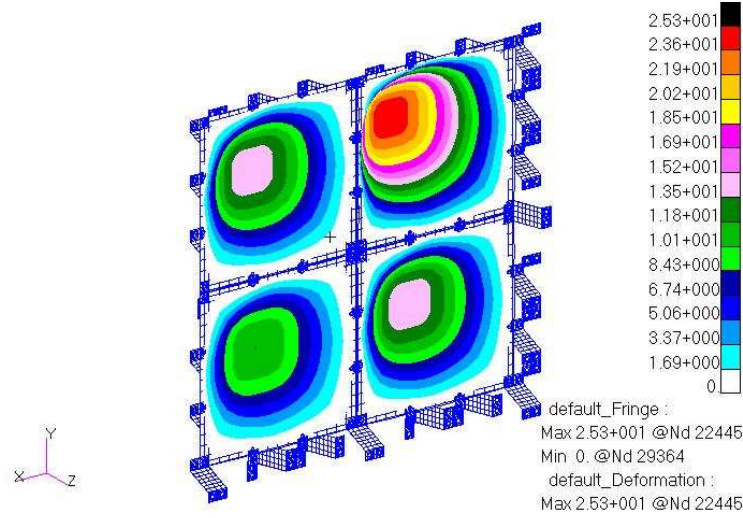
Figure 23: First Mode Shape for One of the Damaged Corner Bolts on Upper Right Plate

Table 3: Optimization Results for Four-Design-Variable Problem

	Lower Bound	Upper Bound	Initial Design	Optimized Design
x_1 (in)	0.050	0.250	0.100	0.050
x_2 (in)	0.750	0.250	0.150	0.250
x_3 (in)	0.050	0.250	0.100	0.250
x_4 (in)	0.085	0.250	0.170	0.085
F_1	N/A	N/A	1.69E-02	1.38E+09

first design iteration resulted in the bracket thickness and horizontal plate edge thickness decreasing to their lower boundaries and the middle horizontal portion of the plate and the vertical portions of the plates increasing to their upper boundaries. The design variables and objective function for this problem are shown in Table 3. The decrease to the bracket thickness led to mode switching from out-of-plane load-carrying plate bending to in-plane bracket bending and load-carrying plate shifting due to the decreased stiffness of the brackets. The mode switching resulted in the first three modes being in-plane for the load-carrying plates followed by the out-of-plane bending mode shapes. Also, the frequencies corresponding to the out-of-plane mode shapes were still numerically very close (within one Hz) while the in-plane mode shapes had large differences, which is undesirable. This result was found when different lower bounds and starting bracket thicknesses were used to begin the problem.

59

Due to this undesired mode switching, the design optimization was retried with the bracket thickness remaining constant throughout the optimization process, leaving only three design variables. While this did prevent the mode switching from occurring, the three remaining design variables did not result in sufficient frequency distribution. This shows that the frequency distribution is not sensitive to the load-carrying plate thicknesses for this stated problem. This is likely due to the symmetry of the problem resulting from the chosen design variables. Therefore, additional design variables must be introduced to eliminate this symmetric constraint imposed with four design variables.

4.1.3   Nine-Design-Variable Results

This new design optimization problem contained nine design variables: two for each of the four load-carrying plates (one for the horizontal face thickness—x_1, x_3, x_5, x_7—and one for the thickness of the vertical faces which hold the insulation—x_2, x_4, x_6, x_8) and one for thickness of all brackets x_9. Since each of the plates have independent design variables, design flexibility is greatly increased and global symmetry is no longer required. The outputs and objective function from the four-design-variable problem are used in this nine-design-variable problem also. While this problem formulation successfully separated the first 10 natural frequencies (shown in Table 4), the mode shapes of the healthy design changed due to the lack of symmetry for the problem. The first four natural frequencies each demonstrated one of the load-carrying plates having out-of-plane bending, while the other three load-carrying plates showed no deformation (similar to mode shape 1 in Fig. 22). The relationship between the plates and mode shapes for this design are: the first mode shape has only Plate 4 bending, the second mode shape has only Plate 1 bending, the third mode shape has only Plate 3 bending, and the fourth mode shape has only Plate 2 bending.

Numerically obtained mode shapes 5, 6, and 7 demonstrated in-plane deformation of the load-carrying plates, which would make it harder for sensors to observe these deformations in a laboratory. For this reason, the damage quantification began with a focus on the first four natural frequencies and mode shapes. The higher frequencies and mode shapes are only used if no conclusions

Table 4: Natural Frequencies for Healthy Nine-Design-Variable Problem

Frequency Number	Original Natural Frequency (Hz)	Optimized Natural Frequency (Hz)
1	799.32	672.78
2	799.59	716.07
3	799.60	761.36
4	799.88	805.15
5	1144.9	999.71
6	1144.9	1003.0
7	1145.0	1151.2
8	1145.4	1202.3
9	1187.1	1216.5
10	1189.6	1336.8

could be made from the first four. The damage quantification of this nine-design-variable problem showed partial success. Damaged fasteners located at the side of the load-carrying plates resulted in a noticeable frequency drop. The frequency drop—between 13.3 Hz and 19.7 Hz—occurred in the natural frequency corresponding to the load-carrying plate secured with the damage fastener—damage to Plate 1 caused a drop to the second natural frequency, damage to Plate 2 caused a drop to the fourth natural frequency, damage to Plate 3 caused a drop to the third natural frequency, and damage to Plate 4 caused a drop to the first natural frequency. The other three natural frequencies of interest (not corresponding to the mode shape of the damaged plate) and all four of the mode shapes remained the same. For example, if one of the eight side fasteners of Plate 4 (which moved at the first natural frequency) is damaged, the first natural frequency drops from 672.78 Hz to between 659.11 and 659.46 Hz. This damage state shows no change in frequencies 2-4 or mode shapes 1-4. This change in the first natural frequency shows that the damage occurred with Plate 4 (the load-carrying plate excited by the first natural frequency). Similar results were obtained for the side fasteners of Plates 1-3. This allows the load-carrying plate with a single damaged side fastener to be determined based on only the frequency changes in the system.

Determining damage of a corner fastener for this design did not work so easily. Fastener damage at the corner bolts did not result in a physically usable frequency change (less than a 0.6 Hz decrease occurred) in the first four natural frequencies. Also, no significant changes occurred in the first four mode shapes; therefore, corner fastener damage appears to be physically undetectable
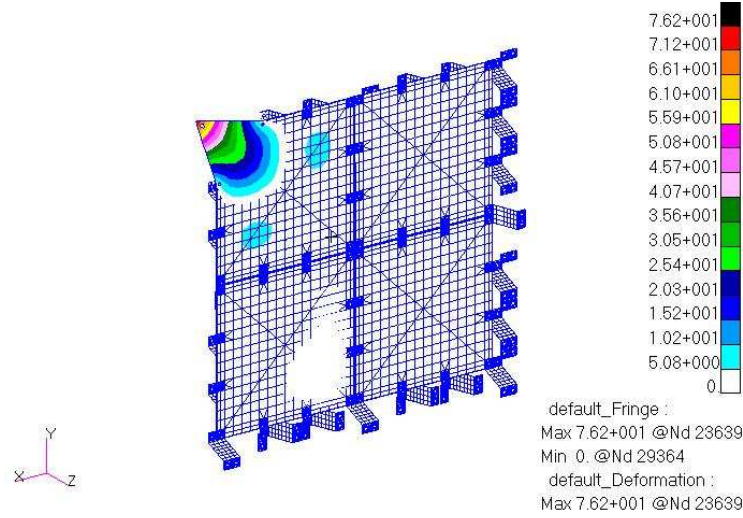
Figure 24: Seventh Mode Shape for Damaged Upper Left Corner Bolt on Upper Left Plate

when using the numerical results of only the first four natural frequencies. This leads to the need to use natural frequencies and mode shapes above the fourth to determine if the numerical results allow for the damaged corner bolt to be characterized. For each of these 16 damaged corner bolt cases, the 7th, 8th, or 9th mode shape showed isolated bending of the load-carrying plate where the damaged bolt is no longer constraining it. Two examples for this group of deformation are shown in Figure 24 and Figure 25. Since these modes do not exist in the healthy system, they are easily observable with the proper sensor placement. Since new mode shapes are introduced with these corner bolt damage states, quantifying the damage from the natural frequency results alone is very difficult. The easiest way to observe this new mode shape in a physical system would be to place sensors (piezoelectric, accelerometers, etc.) close to the corners of the load-carrying plates to ensure that any movement is captured. The initial and optimal design variables for this nine-design-variable problem are shown in Table 5.

After these results were obtained, a combined objective function was formed using Equation (16) and Equation (17) for a damaged corner fastener to determine if the first four natural frequencies with this damage state could be separated from the healthy case more effectively. This nine-design-variable optimization problem produced results similar to the results that utilized only Equation (16)—the damaged corner bolt state demonstrated no significant changes in the first four

62
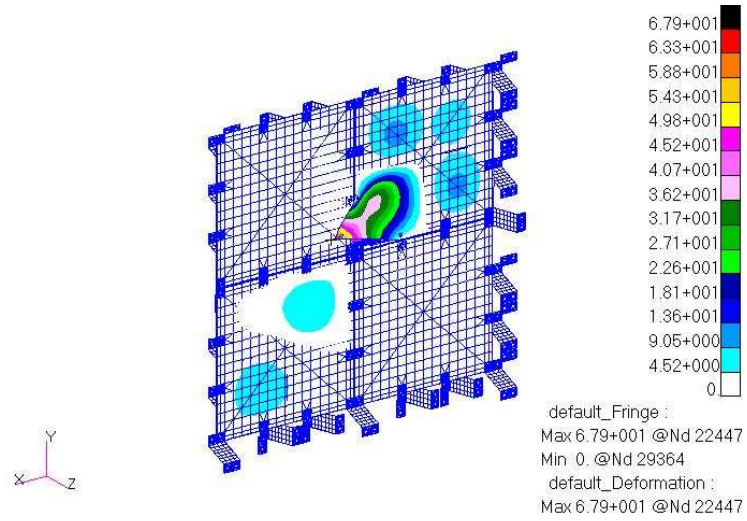
Figure 25: Eighth Mode Shape for Damaged Lower Left Corner Bolt on Upper Right Plate

Table 5: Optimization Results for Nine-Design-Variable Problem

	Lower Bound	Upper Bound	Initial Design	Optimized Design
x_1 (in)	0.050	0.250	0.100	0.164
x_2 (in)	0.050	0.250	0.100	0.250
x_3 (in)	0.050	0.250	0.100	0.248
x_4 (in)	0.050	0.250	0.100	0.150
x_5 (in)	0.050	0.250	0.100	0.240
x_6 (in)	0.050	0.250	0.100	0.248
x_7 (in)	0.050	0.250	0.100	0.216
x_8 (in)	0.050	0.250	0.100	0.070
x_9 (in)	0.085	0.250	0.170	0.145
F_1	N/A	N/A	3.83E-04	7.12E+14

natural frequencies, but observation of higher frequency values and mode shapes successfully distinguished between the healthy and damaged states. Due to the similarity between the design results for this combined objective function with the results for the first objective function only, this result is not included in this paper.

4.2 Finite Element Model Validation Results

Since the finite element analysis captures lower frequencies with the most accuracy, the first three natural frequencies will be of the most interest for this validation process. The deterministic model allowed for material property updating for validation versus the obtained experimental results. The material properties were optimized within the bounds allowable from collected experimental results using the Modified Method of Feasible Directions in VisualDOC [149]. The objective function for the optimization problem was to minimize the sum of the differences between the experimental and finite element analysis results for the first three natural frequencies. The material properties converged to an optimum after 15 iterations. The optimized material properties are shown in Table 6. The final version of the finite element model showed very good agreement with the experimental results (less than 1% difference versus the mean value for the first three natural frequencies) for the free-free boundary condition case without insulation. Also, after this case was completed, the insulation mass was added to the finite element model and compared to the first natural frequency obtained experimentally (only the first natural frequency was successfully obtained since the insulation damped out the higher modes). These results are shown in Table 7.

After the single load-carrying plate finite element model was validated, the entire TPS finite element model was validated versus experimental results. The C-C material properties obtained from the single load-carrying plate validation was used for the composite plates in the assembly. The variables for this finite element model were the material properties of the carbon/silicon carbide (C/SiC) composite brackets. The same method and objective function were used for the material updating of the entire assembly as was used for the load-carrying plate cases. The results for the finite element model of the TPS assembly are shown in Table 8.

Table 6: Optimized Carbon-Carbon Material Properties

Material Property	Lower Bound	Upper Bound	Initial Design	Optimized Design
E (Msi)	11.761	12.460	12.150	12.456
Poisson's Ratio	0.308	0.358	0.324	0.315
Density (lb/in^3)	5.95E-02	6.05E-02	6.01E-02	6.02E-02

Table 7: Experimental Validation of a Single Load-Carrying Plate

Natural Frequency	Experimental Average (Hz)	FEA (Hz)	Percent Difference for FEA
1 (without insulation)	193.26	193.32	0.03%
2 (without insulation)	1292.5	1282.6	0.77%
3 (without insulation)	1329.9	1334.3	0.33%
1 (with Insulation)	180.25	180.61	0.20%

Table 8: Experimental Validation of the TPS Assembly

Natural Frequency	Experimental Average (Hz)	FEA (Hz)	Percent Difference for FEA
1	129.36	125.29	3.15%
2	147.68	152.26	3.10%
3	152.37	161.76	6.16%

4.3   Modal-based Damage Detection Results

The file-reading and data processing of the MAC were completed using MATLAB. The mode shapes used to obtain these results were found using the finite element model that was validated versus experimental results. First, the MAC is computed using the same healthy finite element eigenvectors to observe the differences between the first five mode shapes. Using the same eigenvectors for the MAC calculation results in a symmetric matrix where the main diagonal is 1.0. The off-diagonal terms in this MAC matrix demonstrate how similar the eigenvectors are to each other. For example, since the terms corresponding to the correlation between the first and fifth eigenvectors in the healthy-healthy MAC is 0.71808, these eigenvectors are fairly similar at the selected nodes when compared to any of the other off-diagonal terms. This healthy-healthy MAC is shown in Table 9. There are two main ways to detect damage using MAC: large reductions in the magnitude of one or more terms along the main diagonal and large terms appearing in off-diagonal locations which are small in the healthy-healthy MAC seen in Table 9. These two damage detection cases will be referred to as diagonal MAC reduction and mode switching. The diagonal MAC reduction represents a case where the mode shape has significantly changed from the healthy state.

For this case, a main-diagonal term reduced below 0.700 from an expected value above 0.900 will be the damage threshold. The unexpected off-diagonal large terms arises due to mode switch-

Table 9: Healthy-Healthy MAC Matrix

	Healthy					
	Mode	1	2	3	4	5
Healthy	1	1.00000	0.00013	0.00000	0.00002	0.71808
	2	0.00013	1.00000	0.00003	0.00473	0.00072
	3	0.00000	0.00003	1.00000	0.02590	0.00044
	4	0.00002	0.00473	0.02590	1.00000	0.00001
	5	0.71808	0.00072	0.00044	0.00001	1.00000

ing introduced by the damage. In mode switching, the order of the mode shapes is not the same for the healthy and damaged cases. This occurs since the damage causes the natural frequency corresponding to one mode shape to shift to a value lower than that of another natural frequency of the structure.

This research encounters some damage states that cause the third healthy mode shape to be excited before the second healthy mode shape; thus, a mode switch between modes two and three occurs in this example. The MAC and PMAC are combined in a two-tiered approach for damage detection and localization. The first tier is computing the MAC matrix using the finite element results for the healthy and damaged structural states. Observing diagonal MAC reduction and mode switching in this tier detects the damage. The second tier computes four separate PMAC matrices consisting of the 49 nodal locations for each individual plate. This second tier isolates the correlation between the healthy and damaged mode shapes for each plate. If a local mode shape is affected by the damaged bolts, this will cause the PMAC for that mode shape to decrease in value. Therefore, if damage is detected in the structure by a reduction in one or more MAC terms, the plate with the lowest corresponding PMAC corresponding to the reduced MAC term should be the plate attached to the damaged bolts. The COMAC is used as a supplement to the two-tiered MAC/PMAC method. While it is not required to complete the two-tiered approach, it provides additional information that should aid in determining the damage location.

Additionally, the new mode-based damage metrics—NOCOMAC and NOCOMACSUM—are investigated. The NOCOMAC outputs a percentage of location predictions to be close to the damage based on mode shape normalization. A higher accuracy percentage represents the damage
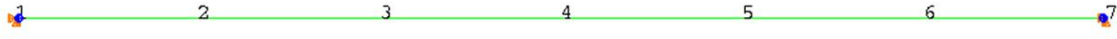
Figure 26: Node Numbering of the Six-Beam Example Problem

being successfully detected. The NOCOMACSUM results in a single weighted summation vector with one value for each node used in the investigation. The node with the highest overall value will be taken to be closest to the damage in the structure. Since the damage introduced to the structure is known, the success of the two-tiered MAC/PMAC method, the COMAC, the NOCOMAC, and the NOCOMACSUM can be investigated independently and compared. Before investigating the validated finite element model, the methods will all be utilized on a simple example problem to demonstrate the approaches.

4.3.1 Six-beam Example Problem

To demonstrate the new damage metrics, an example problem was created and analyzed using ABAQUS/CAE. The model consists of six beam elements in a horizontal line in the xy-plane fixed at the ends can be seen in Figure 26. The healthy state is fixed in all six degrees of freedom at the left edge (Node 1) and the right edge (Node 7). The damaged state is fixed in all six degrees of freedom at the left edge (Node 1) and free to rotate about the z-axis at the right edge (Node 7). The first five natural frequencies are used to calculate all of the damage metrics in this problem. The first step in solving this problem is to calculate the MAC matrix based on the first five healthy and damaged mode shapes.

Table 10 shows the modal vectors for the healthy state. Each column represents a modal vector corresponding to the natural frequency listed at the top of the column. Table 11 shows the modal vectors for the damaged state. These values are used to calculate the MAC matrix seen in Table 12. Table 12 shows that while the mode shapes between the healthy and damaged mode shapes are different, they are still reasonably correlated. The first and fifth mode shapes have MAC values of 0.9433 and 0.9465 while the highlighted second through fourth MAC values are lower (0.8832,

Table 10: Healthy Modal Vectors

		Modal Vector at Natural Frequency				
		1	2	3	4	5
Node	2	0.2827	0.6542	-0.9524	-1.0000	0.8225
	3	0.7747	1.0000	-0.2982	0.6535	-0.9453
	4	1.0000	0.0000	1.0000	0.0000	1.0000
	5	0.7747	-1.0000	-0.2982	-0.6535	-0.9453
	6	0.2827	-0.6542	-0.9524	1.0000	0.8225

Table 11: Damaged Modal Vectors

		Modal Vector at Natural Frequency				
		1	2	3	4	5
Node	2	0.2254	0.5393	0.8935	1.0000	-0.9229
	3	0.6713	1.0000	0.5632	-0.4327	1.0000
	4	1.0000	0.3923	-0.9167	-0.3923	-0.9486
	5	0.9956	-0.6512	-0.2817	0.9239	0.7366
	6	0.6179	-0.8683	1.0000	-0.7481	-0.4019

0.8658, and 0.8830). This demonstrates that none of the modes switch, and the first and fifth mode shapes are correlated higher than the second, third, and fourth.

Table 13 shows the COMAC values for damage localization. The lowest values of the COMAC predict damage location since these are the locations that contribute the most to the decreased MAC diagonal. While the lowest value is accurately predicted at Node 6 (closest to the actual damage location of Node 7), the three values from Node 4-6 are all very close to Node 4, and slightly higher than Node 6 (0.8979 versus 0.8711). This would predict that the damage would be almost as likely in the middle as it would be at the right edge.

The NOCODIFF in Table 14 shows how the normalization at each of the five nodes for the

Table 12: MAC Matrix between Healthy and Damaged Modal Vectors

		Healthy				
	Mode	1	2	3	4	5
Damaged	1	0.9433	0.0524	0.0037	0.0005	0.0001
	2	0.0411	0.8832	0.0693	0.0058	0.0006
	3	0.0105	0.0461	0.8658	0.0736	0.0041
	4	0.0040	0.0144	0.0501	0.8830	0.0487
	5	0.0012	0.0040	0.0112	0.0370	0.9465

69

Table 13: COMAC Values for Damage Localization

Node 2	Node 3	Node 4	Node 5	Node 6
0.9904	0.9561	0.8979	0.9053	0.8711

Table 14: NOCODIFF for First Modal Vector

		Difference Normalized to Node				
		2	3	4	5	6
Node	2	0.0000	0.0291	0.0573	0.1385	0.6352
	3	0.2379	0.0000	0.1034	0.3257	1.6539
	4	0.8992	0.1988	0.0000	0.2864	1.9189
	5	1.6767	0.4831	0.2209	0.0000	1.1291
	6	1.7413	0.5555	0.3352	0.2557	0.0000

Table 15: NOCODIFF for First Modal Vector Normalized to Maximum Components

		Normalized Difference Normalized to Node				
		2	3	4	5	6
Node	2	0.0000	0.0525	0.1709	0.4253	0.3310
	3	0.1366	0.0000	0.3085	1.0000	0.8619
	4	0.5164	0.3579	0.0000	0.8793	1.0000
	5	0.9629	0.8696	0.6590	0.0000	0.5884
	6	1.0000	1.0000	1.0000	0.7850	0.0000

first mode shape can predict different locations for the damage. The highest values in each column (which are highlighted) demonstrate the location predicted with the largest difference between the healthy and damaged first mode shape. Table 15 is created by normalizing each column versus its highest value component to ensure each column's terms range from zero to one. The components with a value of 1.0 in each column are extracted to form the NOCOMAC in Table 16. Normalization for Nodes 2 through 6 provides predicted damage locations of six, six, six, three, and four. This generates values of one for Node 3, one for Node 4, and three for Node 6, in the first column in Table 16. Therefore, the first mode predicts damage closest to Node 6. Table 16 demonstrates how each of the modal vectors individually contributes to the NOCOMAC along with the total NOCOMAC from the summation of all modes. The final column shows the damage is predicted close to Node 6 since it contains 10 of the 27 values (37.0% of the predicted locations). The values also decrease going away from Node 6, a trend which shows a decreased likelihood of damage moving towards the middle (Node 4) and left edge (Node 2). There are six values for the NOCOMAC corresponding to modes 2 and 4, due to symmetry in the problem which results in a NOCODIFF value with equal maximum values at two nodes both being counted.

Table 16: NOCOMAC for Damage at Node 7

		Maximum Difference for Modal Vector					
		1	2	3	4	5	Total
Node	2	0	0	0	1	1	2
	3	1	1	0	0	1	3
	4	1	2	1	1	0	5
	5	0	2	3	2	0	7
	6	3	1	1	2	3	10

The second damage metric, NOCOMACSUM (seen in Table 17), was calculated with two different weightings. The first weighted summation was calculated with uniform weighting for both the modes and normalized nodes. The second weighted summation was calculated with uniform node weighting and mode weighting using the MAC values from Table 12. This means that the results for mode 1 through 5 were multiplied by 0.9433, 0.8832, 0.8658, 0.8830, and 0.9465 before being added together. The highest value in each column is highlighted to show where that NOCOMACSUM vector predicts the damage to be nearest. The results show that the damage with uniform weighting provided reasonable results where Node 5 and Node 6 had nearly identical values of 15.74 and 15.73, which would predict the damage to be close to these two nodes. When the MAC weighting was used for the second NOCOMACSUM, the largest value shifted to Node 6, slightly higher than Node 5 (14.32 versus 14.15). This demonstrates that using the MAC weighting to calculate the NOCOMACSUM shifts the damage prediction towards Node 6. Therefore, including MAC weighting shows an improvement over the uniform mode weighting by slightly shifting the damage prediction towards the actual damage location of Node 7. Both the uniform and MAC weighted NOCOMACSUM values clearly predict damage closest to the right edge and farthest away from the left edge.

4.3.2 High-level Damage Results

The high-level damage is more severe than the low-level damage; therefore, detecting this damage is investigated first to demonstrate the two-tiered MAC/PMAC theory being used. The defined damage case of each edge consisting of four bolts being simultaneously damaged representing

72

Table 17: NOCOMACSUM for Damage at Node 7

		Normalized Maximum Diff. Summation for Modal Vector						
		1	2	3	4	5	Total	MAC Weight
	2	0.9797	1.6899	2.0912	2.8885	2.4581	10.1074	9.1043
	3	2.3070	2.7204	1.8922	2.0834	2.3236	11.3266	10.2561
Node	4	2.7536	3.4673	2.2421	3.2898	2.0218	13.7745	12.4194
	5	3.0799	3.3305	3.8693	3.3428	2.1184	15.7408	14.1535
	6	3.7850	3.0386	2.2402	2.8171	3.8476	15.7285	14.3229

Table 18: MAC Matrix for Damaged Bolts 4-7

		Healthy		
	Mode	1	2	3
Damaged	1	0.98972	0.00287	0.00003
Bolts 4-7	2	0.00062	0.58362	0.0013
	3	0.00133	0.00361	0.98709

one damaged state resulted in 16 damaged states and one healthy state. These 17 states were all analyzed using ABAQUS. Each of the high-level damage states were detectable using the MAC for the first three healthy and damaged mode shapes. Eight of the damage states were detectable due to diagonal MAC reduction while the other eight were the result of a combined mode switching and MAC reduction. A MAC matrix representing diagonal MAC reduction due to damage of bolts 4, 5, 6, and 7 is shown in Table 18.

Since the MAC between healthy and damaged eigenvector two is only 0.58362, this shows a significant change between healthy mode shape 2 and damaged mode shape 2. This can visually be seen in Figure 27. The reduction in stiffness along the edge containing bolts 4-7 have a much larger magnitude in the damaged state than they had in the healthy state. This causes the easily detectable change in the MAC. Similarly, a MAC matrix demonstrating mode switching and MAC reduction can be seen due to damage to bolts 7, 8, 9, and 10 in Table 19. Since the value of 0.98657 corresponds to healthy mode shape 2 and damaged mode shape 3 (and a MAC reduced 0.55899 between healthy mode shape 3 and damaged mode shape 2), this means that mode shapes 2 and 3 switched due to the damage. The mode shapes for these cases are shown in Figures 28 and 29. Figure 28 shows how the healthy mode shape 3 corresponds to the damaged mode shape 2.
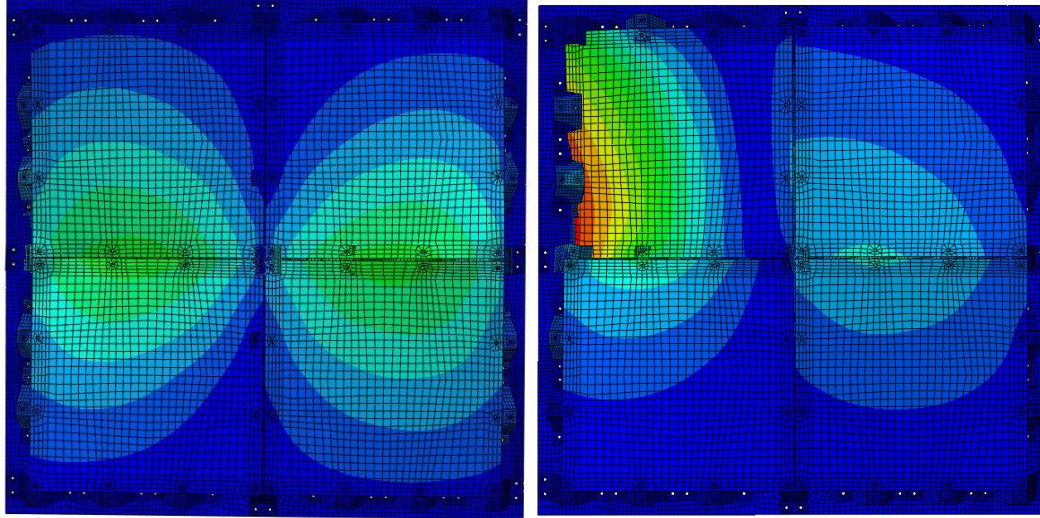
Figure 27: Healthy Mode Shape 2 and Damaged Bolts 4-7 Mode Shape 2

Table 19: MAC Matrix for Damaged Bolts 7-10

		Healthy		
	Mode	1	2	3
Damaged	1	0.99398	0.00061	0.0017
Bolts 7-10	2	0.02639	0.07439	0.55899
	3	0.00175	0.98657	0.00086

Similarly, Figure 29 shows how the healthy mode shape 2 corresponds to the damaged mode shape 3.

After completing successful damage detection, damage localization was performed by calculating the PMAC for each individual load-carrying plate. As Figures 27 and 28 show, the load-carrying plate with the damaged bolts shows a significant change in mode shape from the corresponding healthy mode shape. Looking at the 3-by-3 PMAC matrices for each of the four plates allowed for damage localization to be made for which load-carrying plate contained the damaged bolts. The 3-by-3 PMAC matrix for the damaged plate contains the diagonal (or off-diagonal, if mode switching is present) term with the lowest magnitude. For the aforementioned damage case to bolts 4-7, the four 3-by-3 PMAC matrices are presented in Table 20. Since the MAC for the Damaged Bolts 4-7 case demonstrated a reduction in the correlation between healthy and damaged mode shape 2, the four PMAC corresponding to this mode shape comparison should isolate the

74
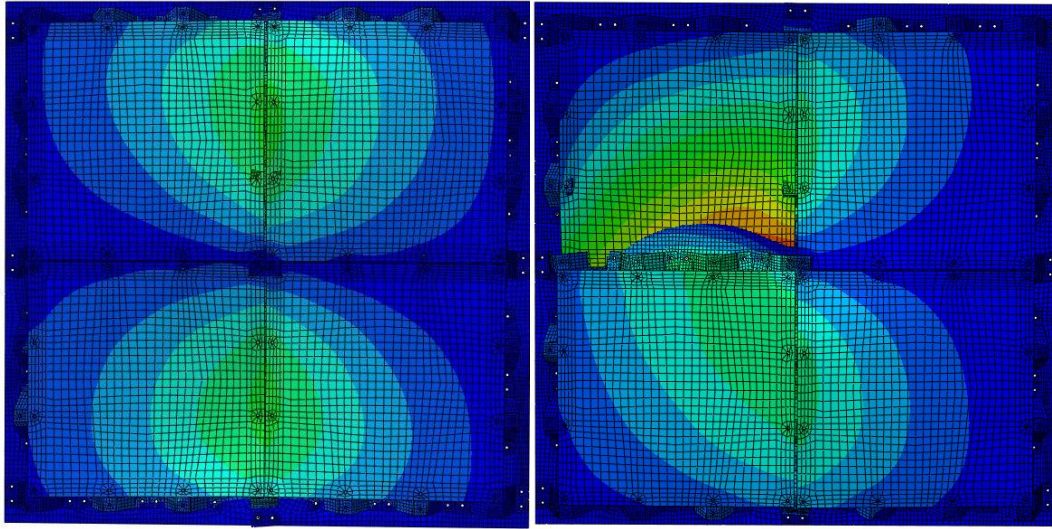
Figure 28: Healthy Mode Shape 3 and Damaged Bolts 7-10 Mode Shape 2
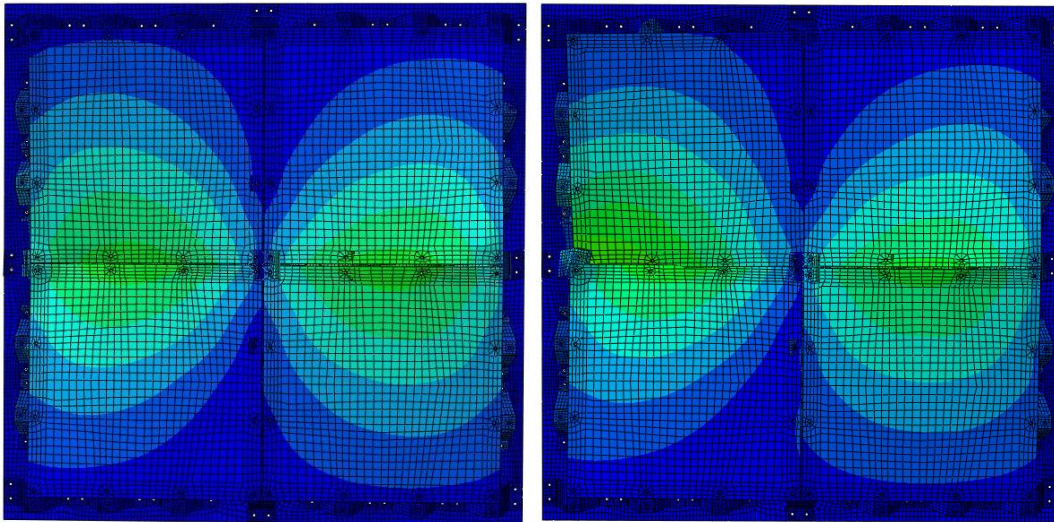
Figure 29: Healthy Mode Shape 2 and Damaged Bolts 7-10 Mode Shape 3

Table 20: Load-Carrying Plate PMAC Matrices for Damaged Bolts 4-7

		Plate 1: Healthy			Plate 2: Healthy			Plate 3: Healthy			Plate 4: Healthy		
	Mode	1	2	3	1	2	3	1	2	3	1	2	3
Damaged Bolts 4-7	1	0.973	0.853	0.560	1.000	0.696	0.709	1.000	0.768	0.595	0.999	0.681	0.662
	2	0.229	0.705	0.143	0.946	0.847	0.740	0.889	0.967	0.397	0.470	0.951	0.211
	3	0.534	0.295	0.984	0.648	0.314	0.991	0.669	0.460	0.991	0.633	0.313	0.997

Table 21: Load-Carrying Plate PMAC Matrices for Damaged Bolts 7-10

	Mode	Plate 1: Healthy			Plate 2: Healthy			Plate 3: Healthy			Plate 4: Healthy		
		1	2	3	1	2	3	1	2	3	1	2	3
Damaged	1	0.999	0.740	0.558	1.000	0.681	0.727	1.000	0.772	0.584	1.000	0.650	0.672
Bolts 7-10	2	0.955	0.886	0.506	0.619	0.252	0.968	0.759	0.464	0.961	0.934	0.681	0.851
	3	0.612	0.977	0.306	0.728	0.998	0.418	0.820	0.996	0.410	0.590	0.993	0.288

damage to a specific plate. As the shaded cells demonstrate, the 0.705 observed in plate 1 is significantly less than the other three PMAC (0.847, 0.967, and 0.951) between healthy and damaged mode shape 2. Since bolts 4-7 attach to plate 1, the damage is correct in localizing the damage to plate 1.

For the other high-level damage state that has been presented, this same method can be used to localize the damage. The four 3-by-3 PMAC matrices used to localize the damage to bolts 7-10 are shown in Table 21. Since this instance showed a mode switch between mode shapes 2 and 3 and a reduction in the MAC between healthy mode shape 3 and damaged mode shape 2, this portion of the PMAC matrices is the focus for damage localization. Looking at the shaded values shows that this value is 0.968, 0.961, and 0.851 for plates 2, 3, and 4, but a much smaller 0.506 for plate 1. Once again, the damage localization has successfully been accomplished for the high-level damage state being investigated. In fact, each of the 16 investigated high-level damage states was correctly localized to the correct plate using the two-tiered MAC/PMAC system.

After successfully localizing the high-level damage with the two-tiered MAC/PMAC system, the COMAC was calculated to investigate if the damage could be further localized to the correct edge within the damaged plate. Since the COMAC calculation creates one COMAC value for each coordinate used in the MAC calculations (196 values for the 14 by 14 grid being used), the COMAC results will be presented graphically to efficiently show the results. The COMAC was not successful in localizing the high-level damage to the correct damaged bolt edge for 13 of the 16 damage states. For the other three damage states, the COMAC showed its lowest values on a line corresponding to the coordinate locations closest to the edge of damaged bolts, successfully localizing the damage. The lowest values of the COMAC are shown in blue in the contour plots
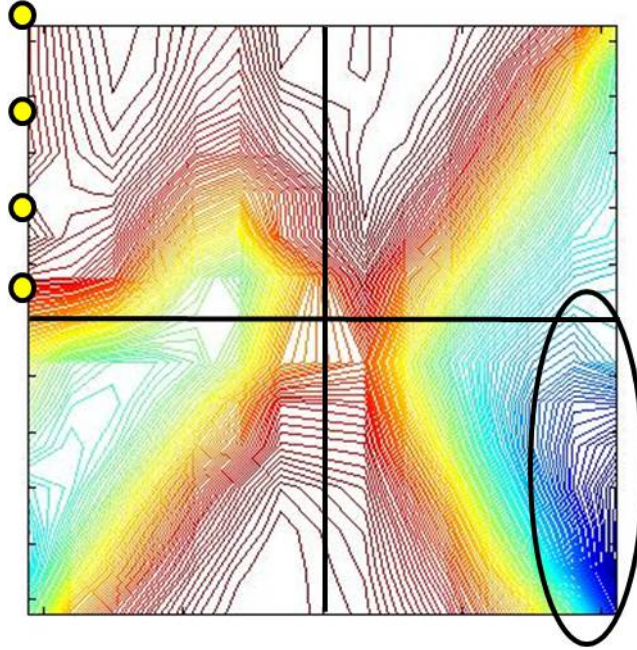
Figure 30: COMAC Plot for Damaged Bolts 4-7

and are circled in Figures 30 and 31. Also, the damaged bolts in the COMAC plots are shown as yellow circles outlined in black. Figure 30 shows the COMAC failing to localize the damage state for damaged bolts 4-7. The lowest values (expected to correspond to the damaged bolt area) are shown in blue and roughly dispersed along the right side, instead of along the top left vertical edge corresponding to the coordinates closest to bolts 4-7. Figure 31 shows the successful damage localization for the state where bolts 7-10 are damaged. It is clearly shown that the circled lowest values are along the line of coordinates closest to bolts 7-10.

Next, the NOCOMAC and the NOCOMACSUM are implemented to investigate the their capability to localize the high-level damage to the correct plate edge. The following variables are used for the NOCOMAC and NOCOMACSUM calculations: number of nodes used, number of modes used, node weighting, and mode weighting. Both the NOCOMAC and NOCOMACSUM are calculated with three separate numbers of nodes—196, 64, and 48—and two separate numbers of modes—three modes and five modes. Different numbers of nodes and modes are used to determine how varying the number of nodes and modes influence the damage detection results. Figures 32-34 show the numbering of the nodal locations and bolt locations used for the damage states
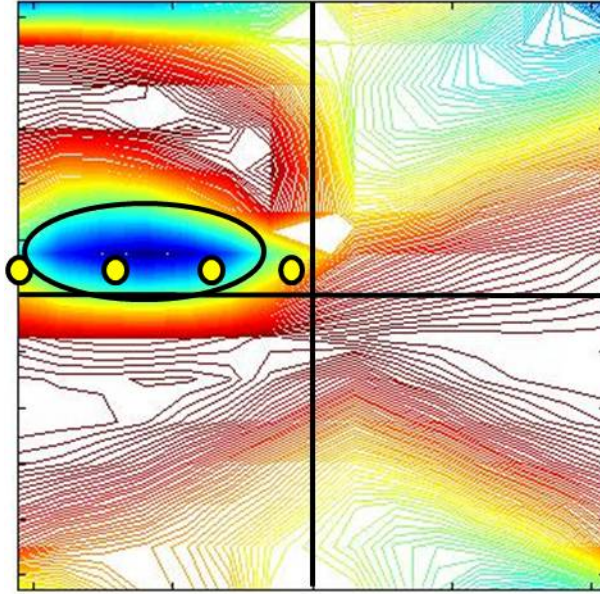
Figure 31: COMAC Plot for Damaged Bolts 7-10

being investigated. The bolt numbering for each of the instances is identical—beginning at the top

right corner for each plate and increasing in the counterclockwise direction. The bolt numbering

is from B1-B48 where B1 is the abbreviation for bolt 1. The numbers (1-196) represent the node

locations used for the NOCOMAC and NOCOMACSUM damage metrics. The nodal locations in

the reduced node location cases (Figures 33 and 34) use a portion of the same nodes as the 196

node case (Figure 32). For example, node 70 in Figure 32 is the same as node 24 in Figure 33 and

node 16 in Figure 34.

Additionally, the NOCOMACSUM was calculated with nine different weighting combinations

to discover how these variables influence the NOCOMACSUM damage prediction. The node and

mode weights are shown in Table 22. The three modal weights used are uniform, the MAC values,

and the inverse of the MAC values. The mode weights using the MAC correspond to the MAC

values of each correlated mode pair for between the healthy and damaged state. The mode weight

using the inverse of the MAC values is equal to one divided by the MAC values of each correlated

mode pair between the healthy and damaged state. The three nodal weights used are uniform (1.0

for all nodes), the edge node weights being twice the inner node weights (edge nodes equal to 1.0

with inner nodes equal to 0.5), and the edge node weights being half the inner node weights (edge

78

```
B4          B3          B2       B1 | B16          B15          B14       B13
   14  28  42  56  70  84  98       |     112 126 140 154 168 182 196
   13  27  41  55  69  83  97       | B17 111 125 139 153 167 181 195
B5 12  26  40  54  68  82  96   B12 |     110 124 138 152 166 180 194        B24
   11  25  39  53  67  81  95       |     109 123 137 151 165 179 193
   10  24  38  52  66  80  94       | B18 108 122 136 150 164 178 192
B6  9  23  37  51  65  79  93   B11 |     107 121 135 149 163 177 191        B23
    8  22  36  50  64  78  92       |     106 120 134 148 162 176 190
B7          B8          B9      B10 | B19          B20          B21       B22
-----------------------------------+-------------------------------------------
B40         B39         B38      B37| B28          B27          B26       B25
    7  21  35  49  63  77  91       |     105 119 133 147 161 175 189
    6  20  34  48  62  76  90       |     104 118 132 146 160 174 188
B41 5  19  33  47  61  75  89   B48 | B29 103 117 131 145 159 173 187        B36
    4  18  32  46  60  74  88       |     102 116 130 144 158 172 186
    3  17  31  45  59  73  87       |     101 115 129 143 157 171 185
B42 2  16  30  44  58  72  86   B47 | B30 100 114 128 142 156 170 184        B35
    1  15  29  43  57  71  85       |      99 113 127 141 155 169 183
B43         B44         B45      B46| B31          B32          B33       B34
```

Figure 32: Bolt and Nodal Location Layout for 196 Nodes Used

```
B4       B3       B2      B1 | B16       B15       B14      B13
    8       16      24    32 |     40       48      56    64
B5                          | B17
    7       15      23    31 |     39       47      55    63      B24
                            |
                            |
B6  6       14      22    30 | B18 38       46      54    62      B23
                            |
    5       13      21    29 |     37       45      53    61
B7       B8       B9     B10 | B19       B20       B21      B22
----------------------------+--------------------------------------
B40      B39      B38    B37 | B28       B27       B26      B25
    4       12      20    28 |     36       44      52    60
B41                         | B29
    3       11      19    27 |     35       43      51    59      B36
                            |
    2       10      18    26 |     34       42      50    58
B42                         | B30                                 B35
                            |
    1        9      17    25 |     33       41      49    57
B43      B44      B45    B46 | B31       B32       B33      B34
```

Figure 33: Bolt and Nodal Location Layout for 64 Nodes

B4		B3		B2		B1	B16		B15		B14		B13
	8		12		16	24		32		36		40	48	
B5	7					23	B12	B17	31				47	B24
B6	6					22	B11	B18	30				46	B23
	5		11		15	21			29		35		39	45
B7		B8		B9		B10	B19		B20		B21		B22
B40		B39		B38		B37	B28		B27		B26		B25
	4		10		14	20		28		34		38	44	
B41	3					19	B48	B29	27				43	B36
B42	2					18	B47	B30	26				42	B35
	1		9		13	17			25		33		37	41
B43		B44		B45		B46	B31		B32		B33		B34

Figure 34: Bolt and Nodal Location Layout for 48 Nodes

nodes equal to 0.5 with inner nodes equal to 1.0).

Since the NOCOMAC outputs one nodal location for each node normalization and each mode shape, the NOCOMAC can be deemed accurate for high-level damage for each instance where the predicted node lies along the edge containing the damage and inaccurate for each instance where the predicted node does not lie along the edge containing the damage. This combination results in the three-mode NOCOMAC with 588, 192, and 144 predicted locations for the three levels of number of nodes used (196, 64, and 48). Similarly, the five-mode NOCOMAC results

Table 22: Weighting Combinations for the NOCOMACSUM

		Nodal Weight (w_n)		
		Uniform (U)	Edge=1, Inner=0.5 (E)	Edge=0.5, Inner=1 (I)
Modal Weight (w_m)	Uniform (U)	U/U	U/E	U/I
	MAC (M)	M/U	M/E	M/I
	Inverse MAC (I)	I/U	I/E	I/I

80

Table 23: NOCOMAC Accuracy for High-level Damage

Damage State	196 Nodes		64 Nodes		48 Nodes	
	% for 3 modes	% for 5 modes	% for 3 modes	% for 5 modes	% for 3 modes	% for 5 modes
1	85.0%	78.7%	84.4%	78.4%	82.6%	76.7%
2	80.3%	75.9%	79.2%	76.3%	77.1%	74.6%
3	86.6%	84.5%	84.4%	83.4%	83.3%	82.9%
4	74.8%	77.8%	76.0%	79.1%	77.8%	80.4%
5	69.4%	69.0%	69.3%	69.1%	69.4%	70.4%
6	84.2%	82.3%	84.4%	83.1%	83.3%	82.5%
7	73.3%	75.4%	75.0%	77.5%	76.4%	78.8%
8	83.8%	77.8%	82.3%	78.8%	79.9%	77.5%
9	87.6%	83.9%	87.0%	83.4%	86.8%	83.8%
10	71.3%	74.6%	72.4%	75.6%	73.6%	76.3%
11	82.7%	76.9%	80.2%	76.3%	77.8%	76.3%
12	57.0%	61.6%	56.3%	62.8%	55.6%	62.9%
13	75.5%	78.8%	75.0%	78.4%	74.3%	78.3%
14	79.1%	74.7%	76.0%	73.1%	73.6%	72.1%
15	78.4%	74.5%	77.6%	73.4%	75.7%	71.7%
16	85.4%	84.1%	82.8%	82.8%	81.3%	82.5%

have 980, 320, and 240 predicted locations for the three node levels. The NOCOMAC results for the high-level damage are shown in Table 23. The damaged states each correspond to a high-level damage state on the edge of failed fasteners (damage state 1 is damaged bolts 1-4, damage state 2 is damaged bolts 4-7, etc.). Table 23 shows the damage state and the percentage of accurate node predictions for both three-modes and five-mode cases for each of the three nodal levels (196, 64, and 48).

All of the 16 high-level damage states are successfully localized to the proper edge for the high-level damage. While an exact percentage for localizing a damage state is in the judgment of the user, any percentage of accurate node predictions above 30.0% is deemed successful for this high-level damage. The lowest percentage of accurate predictions was 55.6% for damage state 12 with three modes and 48 nodes used. This demonstrates how highly accurate and consistent this method can be for large global damage.

Next, the results between the three-node levels (196, 64, and 48) and the two-mode levels

(three and five) are analyzed to determine which set has more accurate damage localizations. The three-mode NOCOMAC results show a slightly greater percentage of accurate predictions than the five-mode NOCOMAC results (78.0% versus 76.9%). The combined three-mode and five-mode results show the best results when using 196 nodes and the worst results when using 48 nodes. The accuracy percentages for the three nodal levels are: 77.5% for 196 nodes, 77.2% for 64 nodes, and 76.7% for 48 nodes. This demonstrates the slight predictive trends of more nodes and fewer modes being used resulting in improved damage localization for high-level damage.

The second damage metric, the NOCOMACSUM, was then calculated for the high-level damage with uniform node and mode weights. This provides a vector composed of a value for each node used in the formulation of the NOCODIFF and NOCOMAC. The location corresponding to the node containing the greatest value in the NOCOMACSUM vector is predicted to be closest to the damage (in this case the predicted node should lie along the edge closest to the damage). The predicted nodes are shown in Table 24 for the three node levels used. The nodes predicted when using both three modes and five modes all result in the node predicted to be accurate for each of the three node levels used. While the exact location of the damage along the edge varied slightly, all of the NOCOMACSUM locations did accurately lie along the damaged edge. Since the NOCOMACSUM successfully localized the damage in all instances with uniform weighting, alternative weighting functions were not investigated for the high-level damage states.

4.3.3   Low-level Damage Results

With the cases of high-level damage successfully localized to the correct plate (and to the correct edge for three of the 16 damaged states), the low-level damage cases were investigated. The healthy-healthy MAC matrix is the same as in MAC matrix for high-level damage, and is shown in Table 9. As expected, the low-level damage cases cause less significant changes than the high-level damage cases. Looking at the 3 x 3 MAC matrix for the cases of low-level damage versus the healthy case resulted in four categories: mode switch, large magnitude reduction along the main matrix diagonal (magnitude below 0.70), moderate magnitude reduction along the main matrix

Table 24: NOCOMACSUM Predicted Node Location for High-level Damage

| Damage | 196 Nodes | | 64 Nodes | | 48 Nodes | |
State	3 modes	5 modes	3 modes	5 modes	3 modes	5 modes
1	98	98	32	32	24	24
2	8	9	5	5	5	5
3	92	8	29	5	21	5
4	93	97	29	31	21	23
5	112	182	40	56	32	40
6	107	112	38	40	30	32
7	120	148	37	53	29	39
8	190	191	61	61	45	45
9	105	189	36	60	28	44
10	105	101	36	34	28	26
11	99	113	33	41	25	33
12	189	188	60	59	44	43
13	77	7	28	4	20	4
14	7	6	4	3	4	3
15	85	1	25	1	17	1
16	91	85	28	25	20	17

diagonal (magnitude between 0.70 and 0.85), and no significant difference along the main matrix diagonal (magnitude above 0.85). The first two categories are the same as in the high-level damage cases. These categories detect only 16 of the 48 low-level damage states.

The third category represents an additional case in which the damage causes a reduction in MAC values that would be between the second category (damage is detected) and the fourth category (damage is not detected). This category contains an additional four damage states that are more difficult to detect than the other 16 states. Even including this category, low-level damage detection using the predefined nodal locations is only successful for 20 of the 48 states. Tables 25-28 show examples of each of the categories. Table 25 shows the MAC matrix for damage to bolt 1 resulting in mode switching between mode shapes 2 and 3. Table 26 shows the MAC matrix for damage to bolt 9 reducing the MAC between healthy and damaged mode shapes for natural frequencies 2 and 3 each being below 0.70. Damage to bolt 18 is shown in Table 27. This MAC has reduced values between healthy and damaged mode shapes for natural frequencies 2 and 3, but

Table 25: MAC Matrix for Damaged Bolt 1

	Healthy		
Mode	1	2	3
Damaged Bolt 1 1	0.99974	0.00009	0.00011
2	0.00024	0.00701	0.97833
3	0.00012	0.99338	0.00746

Table 26: MAC Matrix for Damaged Bolt 9

	Healthy		
Mode	1	2	3
Damaged Bolt 9 1	0.99996	0.00025	0.00000
2	0.00078	0.69216	0.30936
3	0.00008	0.31302	0.68113

the values are not below the original threshold of 0.70. The final MAC matrix where the damage is not detected is shown for damage to bolt 4 in Table 28.

Figure 35 shows a graphic representation of the low-level damage classification using the MAC. The damage state for each of the 48 bolt locations is classified based on the key to the right of the bolt-numbered layout. Some of the damage states fall into both mode switching and either large or moderate magnitude reduction. These cases are classified in the mode switching category since this is typically the more obvious damage state.

Then, the PMAC was used to investigate the low-level damage states observed using the MAC. Only seven of the twenty cases could be successfully localized based on the PMAC values from the plates. These instances showed that either one or two of the PMAC values on the plates were significantly lower than the corresponding PMAC values for each of the other three plates. The remaining thirteen cases of damage could not be localized using the PMAC because the differences

Table 27: MAC Matrix for Damaged Bolt 18

	Healthy		
Mode	1	2	3
Damaged Bolt 18 1	0.99999	0.00012	0.00001
2	0.00300	0.84243	0.14213
3	0.00000	0.23348	0.77056

Table 28: MAC Matrix for Damaged Bolt 4

	Mode	Healthy		
		1	2	3
Damaged	1	0.99996	0.00015	0.00000
Bolt 4	2	0.00010	0.98649	0.01113
	3	0.00000	0.01554	0.98521
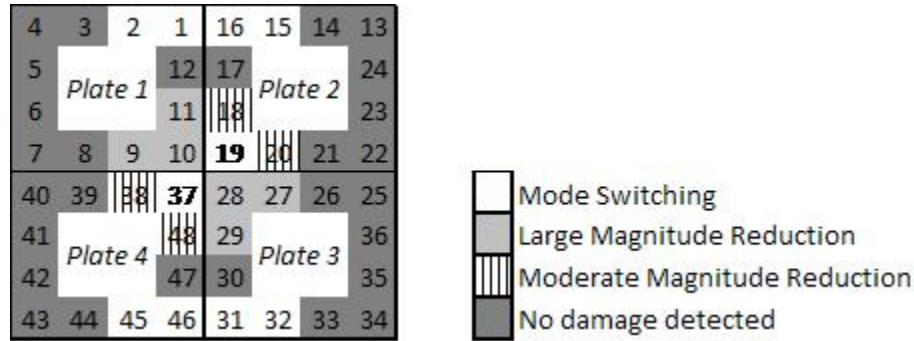
Figure 35: Low-level Damage Classification Using MAC

between the healthy and damaged PMAC values were too minor to definitively show the presence of damage. A sample of the PMAC values indicating successful damage localization is shown in Table 29. The shaded boxes demonstrate less modal agreement between modes 2 and 3 in plate 1 than the other three plates. Plate 1 has both the lowest single diagonal value 0.582 between healthy and damaged mode 2 (the next lowest is 0.643, a significantly larger value), and two diagonal values below the 0.85 threshold that was utilized earlier for minor changes.

The COMAC showed promise in localizing the fastener damage to the correct load-carrying plate (often to the correct bolt). It was able to localize the damage for 27 of the 48 damage states. Once again, the COMAC presentation is best illustrated graphically where the circled blue areas represent the lower values of the COMAC, which would represent the location of the predicted

Table 29: Load-Carrying Plate PMAC Matrices for Damaged Bolt 9

	Mode	Plate 1: Healthy			Plate 2: Healthy			Plate 3: Healthy			Plate 4: Healthy		
		1	2	3	1	2	3	1	2	3	1	2	3
Damaged	1	1.000	0.724	0.587	1.000	0.697	0.712	1.000	0.772	0.591	1.000	0.649	0.674
Bolt 9	2	0.178	0.582	0.002	0.862	0.871	0.760	0.327	0.698	0.005	0.827	0.879	0.708
	3	0.818	0.771	0.836	0.214	0.004	0.658	0.827	0.747	0.855	0.186	0.000	0.643
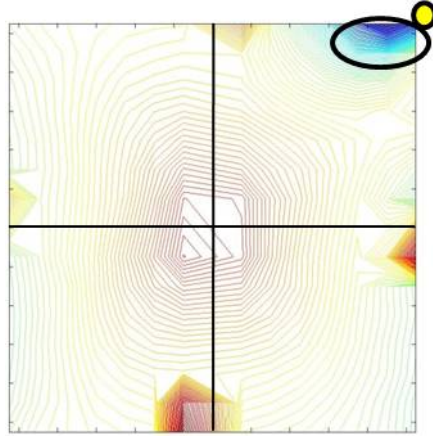
Figure 36: COMAC Plot for Damaged Bolt 13
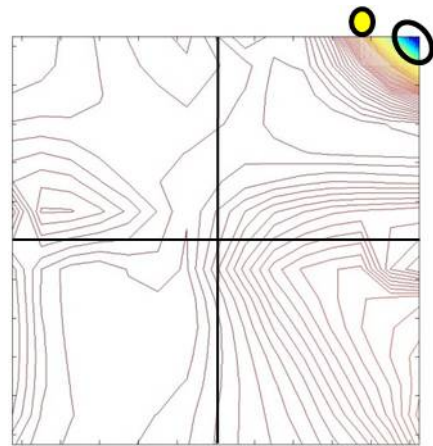
Figure 37: COMAC Plot for Damaged Bolt 14

damaged area. Since the COMAC is more sensitive to small local changes than the MAC and PMAC, it can localize some damage states that otherwise would go undetected.

Four sample COMAC values can be seen in Figures 36-39. Figure 36 shows the COMAC for damage to bolt 13. The circled dark blue area of this plot occurs near the top right corner of the structure, accurately predicting damage to bolt 13 which is shown in yellow. Figure 37 shows a COMAC with the dark blue area predicting damage once again at the top right corner (damage to bolt 13) when the damage is actually located at its neighboring bolt 14. Similarly, Figure 38 demonstrates a predicted damage state for one of the bolts along the upper edge of plate 3 (bolts 25-28) corresponding to the lowest values of the COMAC. Since Figure 38 represents damage at bolt 27, it accurately captures a region containing the damaged bolt, but could not localize the
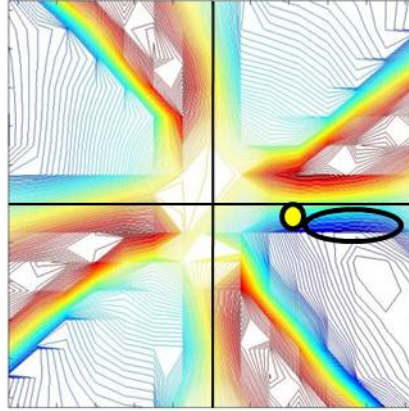
Figure 38: COMAC Plot for Damaged Bolt 27
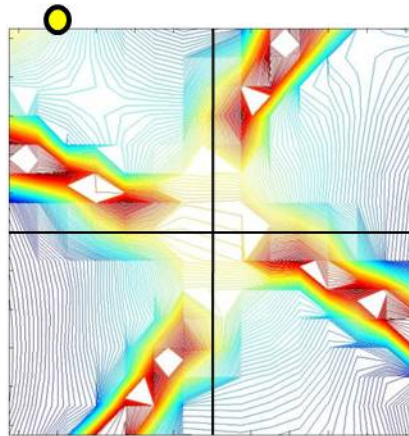
Figure 39: COMAC Plot for Damaged Bolt 3
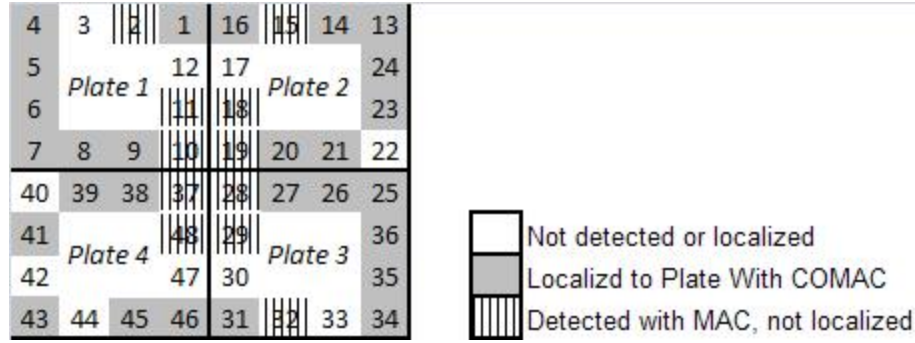
Figure 40: Overall low-level Damage Detection and Localization

damage to an individual bolt. Finally, Figure 39 shows a case where damage goes undetected for damage to bolt 3. No single area is low enough to obtain a predicted damage area, so unlike the other COMAC Figures no region in is circled. The load-carrying plate containing the damaged bolt was correctly predicted in Figs. 36-38, but not in Figure 39.

The localization to a single damaged bolt proved very difficult with the COMAC. In some cases, localization was successful (Fig. 36), in some cases damage was predicted at a neighboring bolt of the actual damaged bolt (Fig. 37), and in some cases a range containing the damaged bolt was predicted (Fig. 38). However, 21 of the 48 low-level damage states do not show a particular region that is most likely to have damage. Figure 39 shows one such case, where no area has a blue region representing a decreased COMAC that accurately indicates damage. Combining the MAC and COMAC results for the low-level damage detection resulted in the data seen in Figure 40. The 27 individual bolt locations shaded in grey represent the damage states that are localized to the correct plate using the COMAC. The 11 individual bolt locations with vertical lines through them represent the damage states that were detected with the MAC, but not successfully localized with the PMAC or COMAC. The remaining 10 bolt locations were not detected or localized with the MAC or COMAC.

The NOCOMAC and NOCOMACSUM were then investigated on the low-level damage with a single fastener failure instead of the high-level damage with all four bolts along an edge being damaged. This results in 48 independent low-level damage states. These damage states are separated into two categories: 16 corner bolts (B1, B4, B7, B10, B13, B16, B19, B22, B25, B28, B31,

B34, B37, B40, B43, B46) and 32 side bolts (B2-3, B5-6, B8-9, B11-12, B14-15, B17-18, B20-21, B23-24, B26-27, B29-30, B32-33, B35-36, B38-39, B41-42, B44-45, B47-48). The results for the NOCOMAC are reduced into three levels: accurate, semi-accurate, and inaccurate. For the low-level damage case, accurate is defined to be a nodal damage prediction localizing to the correct individual bolt. For the 196 node case, the three nodes closest to the damage are deemed accurate for each damage state. For the 64 and 48 node cases, accurate damage assessment is defined for a single node for each damage state. For example, bolt 4 damage is defined as accurate damage assessment for nodes 13, 14, or 28 when using 196 nodes, and for only node 8 in the 64 and 48 node cases. Semi-accurate is defined as the damage being localized to the correct plate, but not to the correct bolt. For example, if bolt 4 damage is localized to any nodal location on the Plate 1 other than 13, 14, or 28, it is deemed semi-accurate since the correct plate is localized but the correct bolt is not localized. The final category, inaccurate, is defined to be any node prediction being made to the wrong plate (Plates 2-4 for bolt 4).

The results for the low-level corner bolt damage accuracy are shown in Table 30. It can easily be seen localizing corner bolt damage is mostly acceptable with the 30.0% accurate threshold being obtained in most cases. Only the three highlighted cells (damaged bolt 13 for three modes used for both 64 and 48 nodes used and damaged bolt 43 for three modes and 48 nodes used) do not meet the 30.0% requirement. The lowest value accuracy percentage of 29.2% is just below the threshold for successful damage localization. Since the low-level corner bolt damage results demonstrated acceptable accuracy percentages, the semi-accurate and inaccurate instances will not be shown.

Next, the results between the three-node levels (196, 64, and 48) and the two-mode levels (three and five) are analyzed to determine which set has more accurate damage localizations. The five-mode NOCOMAC results show a greater percentage of accurate predictions than the three-mode NOCOMAC results (60.6% versus 50.4%). The combined three-mode and five-mode results show the best results when using 196 nodes and the worst results when using 48 nodes. The accuracy percentages for the three nodal levels are: 57.7% for 196 nodes, 55.9% for 64 nodes, and 54.4% for 48 nodes. This demonstrates more nodes predicting slightly better than less nodes and a the

Table 30: NOCOMAC Accuracy for Low-level Corner Bolt Damage

Damaged Bolt	196 Nodes		64 Nodes		48 Nodes	
	% for 3 modes	% for 5 modes	% for 3 modes	% for 5 modes	% for 3 modes	% for 5 modes
1	62.8%	70.5%	56.3%	66.9%	54.2%	65.0%
4	49.7%	61.1%	50.5%	62.5%	49.3%	60.4%
7	77.6%	78.6%	75.0%	77.5%	72.9%	75.0%
10	43.5%	56.2%	41.7%	54.4%	40.3%	52.9%
13	30.6%	50.6%	29.7%	51.3%	29.2%	50.0%
16	58.7%	67.1%	55.2%	65.0%	52.8%	63.8%
19	42.0%	38.9%	41.1%	38.4%	40.3%	38.3%
22	57.8%	68.1%	56.3%	67.5%	54.9%	65.8%
25	61.2%	69.6%	59.4%	68.4%	57.6%	66.3%
28	40.5%	52.2%	35.9%	48.8%	34.0%	47.1%
31	60.4%	67.1%	55.2%	64.1%	53.5%	62.9%
34	56.6%	65.2%	55.7%	65.3%	54.2%	63.3%
37	45.4%	57.6%	44.3%	55.3%	44.4%	54.6%
40	53.6%	64.5%	51.0%	63.1%	49.3%	61.3%
43	30.8%	49.2%	30.2%	48.8%	29.9%	47.1%
46	53.6%	65.6%	47.9%	61.9%	46.5%	60.4%

five-mode results being significantly better than the three-mode results for the low-level corner bolt damage.

The results for the low-level side bolt damage accuracy are shown in Table 31. Since the low-level side bolt damage does not influence the stiffness of the system as significantly as the high-level damage or the low-level corner bolt damage, most of the percentages are below the 30.0% threshold set for successful damage localization. Only five of the damaged side bolts (bolts 6, 27, 36, 41, and 45) reached the 30.0% threshold for all six of the cases. In some instances, an additional seven damaged side bolts could be localized. All of the instances successfully localized to the correct bolt using the NOCOMAC are highlighted in Table 31.

The damage localization for the low-level side bolt damage demonstrated virtually no sensitivity to the number of modes or the number of nodes being used. The three-mode NOCOMAC results have a slightly greater percentage of accurate predictions than the five-mode NOCOMAC results (23.5% versus 23.0%). The accuracy percentages for the combined three nodal levels are:

Table 31: NOCOMAC Accuracy for Low-level Side Bolt Damage

Damaged Bolt	196 Nodes		64 Nodes		48 Nodes	
	% for 3 modes	% for 5 modes	% for 3 modes	% for 5 modes	% for 3 modes	% for 5 modes
2	28.1%	27.2%	27.6%	23.4%	27.1%	22.1%
3	28.1%	16.8%	27.6%	16.6%	27.8%	16.7%
5	29.1%	17.7%	29.2%	19.7%	29.2%	20.4%
6	51.2%	39.7%	48.4%	34.1%	47.2%	32.9%
8	21.4%	39.9%	24.5%	40.6%	24.3%	41.3%
9	23.5%	16.4%	13.5%	8.1%	9.7%	5.8%
11	0.0%	8.6%	0.0%	8.1%	0.0%	8.8%
12	0.0%	24.7%	0.0%	24.4%	0.0%	25.8%
14	23.3%	14.7%	21.9%	14.1%	20.8%	13.8%
15	27.9%	16.7%	27.6%	16.6%	27.1%	17.1%
17	2.2%	26.0%	3.6%	26.3%	4.9%	26.7%
18	6.0%	3.6%	1.0%	0.6%	0.7%	0.4%
20	36.6%	33.3%	16.1%	20.9%	13.9%	19.2%
21	24.8%	40.1%	24.0%	38.4%	26.4%	40.4%
23	41.7%	25.0%	36.5%	21.9%	34.7%	20.8%
24	28.1%	16.8%	27.1%	16.3%	25.7%	15.4%
26	21.4%	38.8%	20.8%	37.5%	22.2%	38.8%
27	42.0%	41.9%	34.4%	35.3%	31.9%	33.8%
29	2.7%	1.6%	0.0%	0.0%	0.0%	0.0%
30	0.3%	25.4%	2.1%	25.6%	2.8%	25.8%
32	27.9%	16.7%	27.6%	16.6%	27.1%	16.3%
33	28.4%	17.0%	27.6%	16.6%	27.1%	16.3%
35	28.1%	16.8%	27.6%	16.6%	27.8%	17.9%
36	79.4%	47.7%	54.7%	32.8%	53.5%	32.1%
38	42.9%	29.5%	19.8%	13.8%	17.4%	12.5%
39	25.2%	40.6%	26.6%	41.3%	25.7%	41.3%
41	48.3%	36.9%	44.8%	31.6%	44.4%	31.7%
42	23.5%	14.8%	22.9%	14.7%	22.2%	14.6%
44	0.0%	0.0%	0.0%	0.0%	0.0%	0.0%
45	52.2%	36.3%	46.9%	31.3%	45.1%	32.1%
47	0.0%	26.3%	0.0%	23.8%	0.0%	24.6%
48	0.0%	12.2%	0.0%	11.6%	0.0%	10.4%

24.3% for 196 nodes, 21.3% for 64 nodes, and 21.0% for 48 nodes. This demonstrates a very slight predictive trend of more nodes improving results, and three modes working better than five modes for damage localization of low-level corner bolt damage.

This leads to a secondary fastener failure localization being used for low-level side bolt damage based on localizing to the correct plate. Correct plate localization will be determined when over half of the predicted locations are either accurate (to the correct bolt) or semi-accurate (to the correct plate). This will be investigated by determining which side bolt locations have an inaccurate percentage below 50.0%. The inaccuracy results for the NOCOMAC for low-level side bolt damage are shown in Table 32. The highlighted cells are instances where the damage is successfully localized to the correct plate. Thirteen damaged side bolt locations are correctly predicted to the plate in all six instances, while an additional eight side bolt locations are correctly predicted to the plate in at least one of the six instances. While the NOCOMAC can successfully localize the damage to some extent in the majority of low-level damage cases, it is not successful in localizing all of the low-level states. At least some of the instances localized the low-level bolt damage to the correct bolt for 28 of the 48 damaged states (16 corner bolts and 12 side bolts) and to the correct plate for 37 of the 48 damage states (16 corner bolts and 21 side bolts) using the NOCOMAC.

The NOCOMACSUM was then calculated for the low-level damage with the nine weighting combinations for three modes and for five modes. The node with the highest output value in the NOCOMACSUM was then used as the predicted location of the damage. These predicted locations were then separated into the accurate, semi-accurate, and inaccurate categories that were used in the NOCOMAC low-level damage localization. All of the corner bolt damage cases were successfully localized to the correct bolt. The low-level side bolts were collectively investigated and separated into groups for easy comparison. The average values of the 32 side-bolt damage cases over all of the instances are: 12.83 accurate, 12.09 semi-accurate, and 7.07 inaccurate. This shows that, on average, the NOCOMAC accurately localized the 48 low-level damage states to the right bolt 28.83 times (16 corner and 12.83 side), to the right plate 40.92 times (16 corner and 24.92 side), and did not localize to the right plate 7.07 times.

Table 32: NOCOMAC Inaccuracy for Low-level Side Bolt Damage

Damaged Bolt	196 Nodes		64 Nodes		48 Nodes	
	% for 3 modes	% for 5 modes	% for 3 modes	% for 5 modes	% for 3 modes	% for 5 modes
2	61.2%	56.5%	62.5%	56.6%	61.1%	56.3%
3	65.6%	56.6%	66.7%	57.8%	65.3%	56.7%
5	55.4%	48.3%	51.0%	45.3%	54.9%	46.7%
6	27.6%	32.9%	27.6%	33.1%	29.2%	33.3%
8	54.6%	41.8%	54.2%	41.6%	55.6%	42.1%
9	46.4%	48.6%	46.4%	47.5%	47.2%	48.8%
11	79.9%	67.7%	80.2%	68.1%	80.6%	67.5%
12	67.3%	50.1%	68.2%	50.0%	68.8%	50.0%
14	59.2%	55.6%	59.9%	55.6%	60.4%	56.3%
15	49.3%	50.6%	47.9%	49.7%	49.3%	50.8%
17	96.6%	68.7%	94.3%	66.9%	92.4%	65.4%
18	59.7%	66.2%	61.5%	66.9%	61.8%	67.1%
20	38.8%	38.7%	40.1%	38.8%	38.9%	37.9%
21	27.0%	27.6%	27.6%	25.9%	27.1%	24.6%
23	38.8%	40.4%	35.4%	39.4%	34.7%	39.6%
24	44.7%	43.9%	44.8%	44.7%	45.8%	45.4%
26	33.8%	30.0%	32.3%	30.0%	32.6%	29.6%
27	38.6%	38.0%	38.0%	37.8%	36.8%	36.7%
29	55.6%	57.7%	56.3%	57.8%	56.9%	57.9%
30	63.8%	48.6%	66.1%	51.3%	66.0%	51.3%
32	43.7%	46.5%	46.9%	50.3%	47.2%	52.5%
33	38.3%	44.6%	42.7%	47.2%	43.8%	49.2%
35	43.9%	43.9%	39.1%	42.8%	40.3%	44.6%
36	16.0%	26.3%	17.2%	27.8%	18.8%	28.8%
38	43.9%	54.5%	40.6%	51.9%	41.7%	52.1%
39	68.5%	49.8%	67.2%	49.4%	67.4%	48.8%
41	33.8%	33.7%	34.9%	34.4%	33.3%	33.3%
42	53.6%	54.3%	54.7%	55.3%	56.3%	57.9%
44	87.6%	69.4%	85.4%	70.6%	84.0%	70.0%
45	24.8%	34.7%	24.0%	35.3%	24.3%	36.7%
47	64.8%	46.8%	56.8%	42.8%	55.6%	41.3%
48	79.3%	63.4%	73.4%	59.7%	72.2%	59.2%

Table 33: Average Results for Varying Number of Nodes in NOCOMACSUM Calculation

	196 Node	64 Node	48 Node
Accurate	15.56	10.61	12.33
Semi-Accurate	9.39	14.06	12.83
Inaccurate	7.06	7.33	6.83

Table 34: Average Results for Varying Number of Modes in NOCOMACSUM Calculation

	3 mode	5 mode
Accurate	8.93	16.74
Semi-Accurate	13.00	11.18
Inaccurate	10.07	4.07

Each of the four variables used in the NOCOMACSUM calculation—number of nodes used, number of modes used, mode weight w_m, and node weight w_n—were investigated to determine how the variables influenced the success of making accurate damage localization predictions. The average accurate, semi-accurate, and inaccurate values for each of the variable influences are shown in Tables 33-36. Table 33 shows how the number of nodes used in the NOCOMACSUM calculation influences its accuracy. While using 196 nodes results in the highest accurate average (15.56), the 48 node result has the lowest inaccurate average (6.83). It is likely that the 196 node case has the highest accurate average because it includes nodes between two bolts deemed acceptable for both bolts (such as node 13 being accurate for both bolt 4 and bolt 5). Table 34 illustrates the number of modes used in the NOCOMACSUM calculation being consistently better with five modes used. The five-mode results outperformed the three-mode results with both a higher accurate average (16.74 versus 8.93) and a lower inaccurate average (4.07 versus 10.07). Table 35 demonstrates mode weighting using the MAC (w_m=M) being better than the uniform mode weight (w_m =U) and the inverse mode weight (w_m=I) results in both accuracy and inaccuracy averages. Table 36 displays the node weighting with the edge nodes being twice the inner nodes (w_n=E) superior to both the inner nodes being twice the edge nodes (w_n=I) and uniform node weighting (w_n=U).

These results show that the best average accuracy is obtained when 196 nodes, five modes,

Table 35: Average Results for Varying Mode Weighting in NOCOMACSUM Calculation

	w_m=U	w_m=M	w_m=I
Accurate	12.67	13.50	12.33
Semi-Accurate	12.00	12.67	11.61
Inaccurate	7.33	5.83	8.06

Table 36: Average Results for Varying Node Weighting in NOCOMACSUM Calculation

	w_n=U	w_n=E	w_n=I
Accurate	12.83	13.22	12.44
Semi-Accurate	11.94	11.83	12.50
Inaccurate	7.22	6.94	7.06

MAC mode weighting, and edge node weighting are used. Similarly, the best average inaccuracy is achieved with 48 nodes, five modes, MAC mode weighting, and edge node weighting. The best overall instance obtained with the variable combinations was 20 out of 32 side node accurate readings with only two out of 32 inaccurate readings. This instance was obtained for two cases: 196 nodes, five modes, MAC mode weighting, and uniform or edge node weighting. The only two low-level damage cases that were never accurate or semi-accurate were for the damage in bolt 18 and bolt 44. Both of these damage states resulted in minimal changes in the first five mode shapes that were not detected numerically. No difference was detected with a visual investigation of these two damage states either. Since these damage states did not significantly change the global response to the five modes being investigated, the damage went undetected.

Chapter 5

CONCLUSIONS

This research began with a numerical investigation of damage detection based on natural frequency changes caused by damaged fasteners. Sizing optimization improved the design geometry to allow for damage quantification to take place more effectively. The fastener damage in the TPS model can numerically determine which plate contained the damaged fastener based on the changes in the first 10 natural frequencies and their corresponding mode shapes. Most of the damage states can be detected using only the changes in natural frequencies, but some of the damage states require the use of new mode shapes arising due to the fastener failure for damage detection.

In order to obtain a more robust SHM system for this TPS prototype, a new finite element model was created to include the backing structure. This finite element model captures the entire structure, and not just the load-carrying plates and brackets. The focus of the research was shifted from changing the material thicknesses to optimize the TPS design to validating the new finite element model versus experimental results. Also, since frequency differentiation can be difficult to achieve (especially when ensuring a symmetric design), mode shapes are used to investigate damage instead of focusing on changes in the resonant frequencies. While changes in the resonant frequencies are achieved with sizing optimization, observing changes in the mode shapes corresponding to the resonant frequencies is a better way to detect damage that is less sensitive to environmental changes, like changing environmental temperature.

A research methodology was developed to detect simulated structural damage using a validated finite element model on changes in its low-frequency dynamics. A finite element model was developed to capture the physical characteristics of a TPS prototype. The TPS was composed

of composite parts with approximate material properties. The initial material property estimations provided reasonable answers that could be improved upon by updating the unknown material properties. After completion of the material property updating with the experimentally obtained results, the single load-carrying plate had under a 1% difference for the first three mode shapes. The finite element model of the TPS assembly captured the added complexity of the backing structure, brackets, and bolted locations. The entire structural model agreed with the experimental results for the first three mode shapes, with a maximum difference of 6.16%. This validates that the finite element model properly simulates the low-frequency dynamics of the TPS.

The validated finite element model is then used to complete the fastener failure damage detection based on mode shape changes. Fastener failure damage is simulated using the validated finite element model and modal characteristics are extracted to detect damage. The fastener failure investigation can be composed of an individual failed bolt or multiple failed bolts, depending on the interest of the investigator. In this research, two predefined damage levels were investigated with three calculated modal parameters (MAC, PMAC, and COMAC) between the healthy state and each damaged state. The high-level damage state demonstrated the feasibility of the methodology by properly localizing the damage to the correct load-carrying plate for each damage state, using a two-tiered MAC/PMAC approach. The COMAC works better than the two-tiered MAC/PMAC to localize the low-level damage, but it requires the MAC to be used to check for mode switching. The low-level damage used the same methodology and successfully detected and localized a majority of the damage states. However, some of the low-level damaged states went undetected.

The NOCOMAC and NOCOMACSUM provided improved damage localization versus the two-tiered MAC/PMAC and COMAC results. Both the NOCOMAC and NOCOMACSUM localized the high-level TPS damage to the correct edge for each of the 16 damage states. Similarly, all 16 of the low-level corner bolt damage cases are localized to the correct bolt using the NOCOMAC and NOCOMACSUM. Depending on the selection of the variables used in calculation of the NOCOMAC and NOCOMACSUM, up to 20 of the low-level side bolt damage cases could be localized to the correct bolt with an additional 10 localized to the correct plate. This means that

only two of the 48 low-level damage cases were not successfully localized to the correct plate using the best variables with the NOCOMACSUM versus 21 unsuccessful low-level damage localizations with the two-tiered MAC/PMAC and COMAC approaches. This demonstrates the improved damage localization capabilities of the two new modal-based damage metrics versus the already existing modal metrics.

Bibliography

[1] J. K. Vandiver, "Detection of structural failure on fixed platforms by measurement of dynamic response," *Journal of Petroleum Technology*, vol. 29, pp. 305–310, March 1977.

[2] R. D. Begg, A. C. Mackenzie, C. J. Dodds, and O. Loland, "Structural integrity monitoring using digital processing of vibration signals," in *Proc. of the 8th Annual Offshore Technology Conference*, (Houston, TX), pp. 305–311, May 1976.

[3] O. Loland and C. J. Dodds, "Experience in developing and operating integrity monitoring system in north sea," in *Proc. of the 8th Annual Offshore Technology Conference*, (Houston, TX), pp. 313–319, May 1976.

[4] M. E. Wojnarowski, S. G. Stiansen, and N. E. Reddy, "Structural integrity evaluation of a fixed platform using vibration criteria," in *Proc. of the 9th Annual Offshore Technology Conference*, (Houston, TX), pp. 247–256, May 1977.

[5] R. N. Coppolino and S. Rubin, "Detectability of structural failures in offshore platforms by ambient vibration monitoring," in *Proc. of the 12th Annual Offshore Technology Conference*, (Houston, TX), pp. 101–110, May 1980.

[6] D. M. Duggan, E. R. Wallace, and S. R. Caldwell, "Measured and predicted vibrational behavior of gulf of mexico platforms," in *Proc. of the 12th Annual Offshore Technology Conference*, (Houston, TX), pp. 92–100, May 1980.

[7] R. M. Kenley and C. J. Dodds, "West sole WE platform: Detection of damage by structural response measurements," in *Proc. of the 12th Annual Offshore Technology Conference*, (Houston, TX), pp. 111–118, May 1980.

[8] H. Crohas and P. Lepert, "Damage-detection monitoring method for offshore platforms is field-tested," *Oil and Gas Journal*, vol. 80, pp. 94–103, Feb 1982.

[9] R. Nataraja, "Structural integrity monitoring in real seas," in *Proc. of the 15th Annual Offshore Technology Conference*, (Houston, TX), pp. 221–228, May 1983.

[10] T. R. Whittome and C. J. Dodds, "Monitoring offshore structures by vibration techniques," in *Proc. of the Design in Offshore Structures Conference*, (London, England), pp. 93–100, March 1983.

[11] S. W. Doebling, C. R. Farrar, M. B. Prime, and D. W. Shevitz, "Damage identification and health monitoring structures and mechanical systems from changes in their vibration characteristics: A literature review," Tech. Rep. LA-13070-MS, Los Alamos National Laboratory (Los Alamos, NM), 1996.

[12] C. R. Farrar and S. W. Doebling, "An overview of modal-based damage identification methods," in *EUROMECH 365 International Workshop: DAMAS 97, Structural Damage Assessment Using Advanced Signal Processing Procedures*, (Sheffield, UK), June 1997.

[13] S. W. Doebling, C. R. Farrar, and M. B. Prime, "A summary review of vibration-based damage identification methods," *The Shock and Vibration Digest*, vol. 30, no. 2, pp. 91–105, 1998.

[14] P. Gudmundson, "The dynamic behavior of slender structures with cross-sectional cracks," *Journal of the Mechanics and Physics of Solids*, vol. 31, pp. 329–345, 1983.

[15] M. F. F. Yuen, "A numerical study of the eigenparameters of a damaged cantilever," *Journal of Sound and Vibration*, vol. 103, pp. 301–310, 1985.

[16] F. Ju and M. Mimovich, "Modal frequency method in diagnosis of fracture damage in structures," in *Proc. of the 4th International Modal Analysis Conference*, (Los Angeles, CA), pp. 1168–1174, February 1986.

[17] D. Sanders, R. N. Stubbs, and Y. I. Kim, "Global nondestructive damage detection in composite structures," in *Proc. of the 7th International Modal Analysis Conference*, (Las Vegas, NV), pp. 1501–1507, February 1989.

[18] H. J. Salane, J. W. Baldwin, and R. C. Duffield, "A dynamics approach for monitoring bridge deterioration," *Transportation Research Record*, vol. 832, pp. 21–28, 1981.

[19] M. Kato and S. Shimada, "Vibration of PC bridge during failure process," *ASCE Journal of Structural Engineering*, vol. 112, no. 7, pp. 1692–1703, 1986.

[20] J. D. Turner and A. J. Pretlove, "A study of the spectrum of traffic-induced bridge vibration," *Journal of Sound and Vibration*, vol. 122, no. 1, pp. 31–42, 1988.

[21] W. M. West, "Single point random modal test technology application to failure detection," *The Shock and Vibration Bulletin*, vol. 52, no. 4, pp. 25–31, 1982.

[22] W. M. West, "Illustration of the use of modal assurance criterion to detect structural changes in an orbiter test specimen," in *Proc. of the 4th International Modal Analysis Conference*, (Los Angeles, CA), pp. 1–6, February 1986.

[23] D. L. Hunt, S. P. Weiss, W. M. West, T. A. Dunlop, and S. R. Freesmeyer, "Development and implementation of a shuttle modal inspection system," *Sound and Vibration*, vol. 24, no. 9, pp. 34–42, 1990.

[24] H. J. Petroski and J. L. Glazik, "Effects of cracks on the response of circular cylindrical shells," *Nuclear Technology*, vol. 5, pp. 303–316, 1980.

[25] S. W. Smith and P. McGowan, "Locating damaged members in a truss structure using modal test data- a demonstration experiment," in *Proc. of the 30th AIAA/ASME/ASCE/AHS/ASC*

Structures, Structrual Dynamics and Materials Conference, no. AIAA-89-1291-CP, (Mobile, AL), April 1989.

[26] P. E. McGowan, S. W. Smith, and M. Javeed, "Experiments for locating damage members in a truss structure," in *Proc. of the 2nd USAF/NASA Workshop on System Identification and Health Monitoring of Precision Space Structures*, (Pasadena, CA), pp. 571–615, March 1990.

[27] N. Stubbs, T. Broome, and R. Osegueda, "Nondestructive construction error detection in large space structures," *AIAA Journal*, vol. 28, no. 1, pp. 146–152, 1990.

[28] T. Wolff and M. Richardson, "Fault detection in structures from changes in their modal parameters," in *Proc. of the 7th International Modal Analysis Conference*, (Las Vegas, NV), pp. 87–94, February 1989.

[29] M. H. Richardson and M. A. Mannan, "Remote detection and location of structural faults using modal parameters," in *Proc. of the 10th International Modal Analysis Conference*, (San Diego, CA), pp. 502–507, February 1992.

[30] Y. Chen and A. S. J. Swamidas, "Dynamic characteristics and modal parameters of a plate with a small growing surface crack," in *Proc. of the 12th International Modal Analysis Conference*, (Honolulu, HA), pp. 1155–1161, February 1994.

[31] J. Chance, G. R. Tomlinson, and K. Worden, "A simplified approach to the numerical and experimental modeling of the dynamics of a cracked beam," in *Proc. of the 12th International Modal Analysis Conference*, (Honolulu, HA), pp. 778–785, February 1994.

[32] A. S. J. Swamidas and Y. Chen, "Monitoring crack growth through change of modal parameters," *Journal of Sound and Vibration*, vol. 186, no. 2, pp. 325–343, 1995.

[33] G. Hearn and R. B. Testa, "Modal analysis for damage detection in structures," *Journal of Structural Engineering*, vol. 117, no. 10, pp. 3042–3063, 1991.

[34] O. S. Salawu, "Non-destructive evaluation of constructed facilities using vibration testing," *Insight*, vol. 36, no. 8, pp. 611–615, 1994.

[35] M. R. Chowdhury and M. Ramirez, "A comparison of the modal responses for defective versus nondefective concrete test beams," in *Proc. of the 10th International Modal Analysis Conference*, (San Diego, CA), pp. 508–515, February 1992.

[36] J. Slastan and S. Pietrzko, "Changes of rc-beam modal parameters due to cracks," in *Proc. of the 11th International Modal Analysis Conference*, (Orlando, FL), pp. 70–76, February 1993.

[37] M. G. Srinivasan and C. A. Kot, "Effect of damage on the modal parameters of a cylindrical shell," in *Proc. of the 10th International Modal Analysis Conference*, (San Diego, CA), pp. 529–535, February 1992.

[38] M. Friswell, J. E. T. Penny, and D. Wilson, "Using vibration data and statistical measures to locate damage in structures," *Modal Analysis: The International Journal of Analytical and Experimental Modal Analysis*, vol. 9, no. 4, pp. 239–254, 1994.

[39] D. I. Nwosu, A. S. J. Swamidas, J. Y. Guigne, and D. O. Olowokere, "Studies on influence of cracks on the dynamic response of tubular T-joints for nondestructive evaluation," in *Proc. of the 13th International Modal Analysis Conference*, (Nashville, TN), pp. 1122–1128, February 1995.

[40] G. James, R. Mayes, T. Carne, T. Simmermacher, and J. Gooding, "Health monitoring of operational structures- initial results," in *Proc. of the 36th AIAA/ASME/ASCE/AHS/ASC Structures, Structural Dynamics and Materials Conference*, no. AIAA-1995-1072, (New Orleans, LA), pp. 2226–2236, April 1995.

[41] N. A. Robinson, L. D. Peterson, G. H. James, and S. W. Doebling, "Damage detection in aircraft structures using dynamically measured static flexibility matrices," in *Proc. of the 14th International Modal Analysis Conference*, (Detroit, MI), pp. 857–865, February 1996.

[42] A. Rytter, *Vibration based inspection of civil engineering structures*. PhD thesis, Department of Building Technology and Structural Engineering, AalborgUniversity, Denmark, 1993.

[43] V. Giurgiutiu, *Structural Health Monitoring with Piezoelectric Wafer Active Sensors*. Academic Press, New York, NY, 2008.

[44] P. Cawley, "The impedance method for non-destructive inspection," *NDT International*, vol. 17, no. 2, pp. 59–65, 1984.

[45] C. Liang, F. P. Sun, and C. A. Rogers, "Coupled electro-mechanical analysis of adaptive material systems-determination of the actuator power consumption and system energy transfer," *Journal of Intelligent Material Systems and Structures*, vol. 5, no. 1, pp. 12–20, 1994.

[46] F. P. Sun, C. Liang, and C. A. Rogers, "Experimental modal testing using piezoceramic patches as collocated sensors-actuators," in *Proc. of the 1994 SEM Spring Conference & Exhibits*, (Baltimore, MD), June 1994.

[47] F. P. Sun, Z. Chaudhry, C. Liang, and C. A. Rogers, "Truss structure integrity identification using PZT sensor-actuator," *Journal of Intelligent Material Systems and Structures*, vol. 6, no. 1, pp. 134–139, 1995.

[48] Z. A. Chaudhry, T. Joseph, F. P. Sun, and C. A. Rogers, "Local-area health monitoring of aircraft via piezoelectric actuator/sensor patches," in *Proc. of the SPIE: Smart Structures and Integrated Systems*, vol. 2443, (San Diego, CA), March 1995.

[49] G. Park, H. Sohn, C. R. Farrar, and D. J. Inman, "Overview of piezoelectric impedance-based health monitoring and path forward," *The Shock and Vibration Digest*, vol. 35, pp. 451–463, November 2003.

[50] H. Lamb, "On waves in an elastic plate," *Proc. of the Royal Society of London. Series A, Containing Papers of a Mathematical and Physical Character*, vol. 93, no. 648, pp. 293–312, 1917.

[51] D. N. Alleyne and P. Cawley, "The interaction of Lamb waves with defects," *IEEE Transactions on Ultrasonics, Ferroelectrics and Frequency Control*, vol. 39, no. 3, pp. 381–397, 1992.

[52] J. Blitz and G. Simpson, *Ultrasonic Methods of Non-Destructive Testing*. Chapman & Hall, New York, NY, 1st ed., 1996.

[53] V. Giurgiutiu, "Lamb wave generation with piezoelectric wafer active sensors for structural health monitoring," in *Proc. of SPIE*, vol. 5056, 2003.

[54] C. R. Farrar, W. E. Baker, T. M. Bell, K. M. Cone, T. W. Darling, T. A. Duffey, A. Eklund, and A. Migliori, "Dynamic characterization and damage detection in the I-40 bridge over the Rio Grande," Tech. Rep. LA-12767-MS, Los Alamos National Laboratory (Los Alamos, NM), 1994.

[55] A. Migliori, T. M. Bell, R. D. Dixon, and R. Strong, "Resonant ultrasound non-destructive inspection," Tech. Rep. LA-UR-93-225, Los Alamos National Laboratory (Los Alamos, NM), 1993.

[56] P. Cawley and R. D. Adams, "The locations of defects in structures from measurements of natural frequencies," *Journal of Strain Analysis*, vol. 14, no. 2, pp. 49–57, 1979.

[57] J. J. Tracy and G. C. Pardoen, "Effect of delamination on the natural frequencies of composite laminates," *Journal of Composite Materials*, vol. 23, no. 12, pp. 1200–1215, 1989.

[58] P. Gudmundson, "Eigenfrequency changes of structures due to cracks, notches, or other geometric changes," *Journal of the Mechanics and Physics of Solids*, vol. 30, no. 5, pp. 339–353, 1982.

[59] F. Ismail, A. Ibrahim, and H. R. Martin, "Identification of fatigue cracks from vibration testing," *Journal of Sound and Vibration*, vol. 140, no. 2, pp. 305–317, 1990.

[60] U. Meneghetti and A. Maggiore, "Crack detection by sensitivity analysis," in *Proc. of the 12th International Modal Analysis Conference*, (Honolulu, HA), pp. 1292–1298, February 1994.

[61] J. M. M. Silva and A. J. M. A. Gomes, "Crack identification of simple structural elements through the use of natural frequency variations: The inverse problem," in *Proc. of the 12th International Modal Analysis Conference*, (Honolulu, HA), pp. 1728–1735, February 1994.

[62] C. H. J. Fox, "The location of defects in structures: A comparison of the use of natural frequency and mode shape data," in *Proc. of the 10th International Modal Analysis Conference*, (San Diego, CA), pp. 522–528, February 1992.

[63] X. T. Man, L. M. McClure, Z. Wang, R. D. Finch, P. Y. Robin, and B. H. Jansen, "Slot depth resolution in vibration signature monitoring of beams using frequency shift," *Journal of the Acoustic Society of America*, vol. 95, no. 4, pp. 2029–2037, 1994.

[64] J. M. Lifshitz and A. Rotem, "Determination of reinforcement unbonding of composites by a vibration technique," *Journal of Composite Materials*, vol. 3, no. 3, pp. 412–423, 1969.

[65] W. Wang and A. Zhang, "Sensitivity analysis in fault vibration diagnosis of structures," in *Proc. of the 5th International Modal Analysis Conference*, (London, England), pp. 496–501, February 1987.

[66] N. Stubbs and R. Osegueda, "Global non-destructive damage evaluation in solids," *Modal Analysis: The International Journal of Analytical and Experimental Modal Analysis*, vol. 5, no. 2, pp. 67–79, 1990.

[67] N. Stubbs and R. Osegueda, "Global damage detection in solids–experimental verification," *Modal Analysis: The International Journal of Analytical and Experimental Modal Analysis*, vol. 5, no. 2, pp. 81–97, 1990.

[68] Y. Narkis, "Identification of crack location in vibrating simply supported beams," *Journal of Sound and Vibration*, vol. 172, no. 4, pp. 549–558, 1994.

[69] P. S. Skjaerbaek, S. R. K. Nielsen, and A. S. Cakmak, "Assessment of damage in seismically excited rc-structures from a single measured response," in *Proc. of the 14th International Modal Analysis Conference*, (Detroit, MI), pp. 133–139, February 1996.

[70] D. Sanders, Y. I. Kim, and R. N. Stubbs, "Nondestructive evaluation of damage in composite structures," *Experimental Mechanics*, vol. 32, no. 3, pp. 240–251, 1992.

[71] R. J. Allemang, *Investigation of Some Multiple Input/Output Frequency Response Function Experimental Modal Analysis Techniques*. PhD thesis, Mechanical Engineering Department, University of Cincinnati, Ohio, 1980.

[72] R. J. Allemang and D. L. Brown, "A correlation coefficient for modal vector analysis," in *Proc. of the International Modal Analysis Conference*, (Orlando, FL), pp. 110–116, November 1982.

[73] R. J. Allemang, "The modal assurance criterion - twenty years of use and abuse," *Sound and Vibration Magazine*, vol. 37, pp. 14–23, August 2003.

[74] R. M. Vandawalker, A. N. Palazotto, and R. G. Cobb, "Damage detection through analysis of modes in a partially constrained plate," *Journal of Aerospace Engineering*, vol. 20, pp. 90–96, April 2007.

[75] W. Heylen and T. Janter, "Extensions of the modal assurance criterion," *Journal of Vibrations and Acoustics*, vol. 112, pp. 468–472, October 1990.

[76] J.-H. Kim, H.-S. Jeon, and C.-W. Lee, "Applications of the modal assurance criteria for detecting and locating structural faults," in *Proc. of the 10th International Modal Analysis Conference*, (San Diego, CA), pp. 536–540, February 1992.

[77] J. O'Callahan, "Correlation considerations: Part 4 (modal vector correlation techniques)," in *Proc. of the 16th International Modal Analysis Conference*, (Santa Barbara, CA), pp. 197–206, February 1998.

[78] E. Brechlin, K. Bendel, and W. Keiper, "A new scaled modal assurance criterion for eigenmodes containing rotational degrees of freedom," in *Proc. of the 23rd International Seminar on Modal Analysis*, (Leuven, Belgium), p. 7, September 1998.

[79] J. Wei and R. Allemang, "Model correlation and orthogonality criteria based on reciprocal modal vectors," in *Proc. of the 9th International Modal Analysis Conference*, (Florence, Italy), pp. 486–491, April 1991.

[80] D. Fotsch and D. J. Ewins, "Applications of MAC in the frequency domain," in *Proc. of the 18th Modal Analysis Conference*, (San Antonio, TX), pp. 1225–1231, February 2000.

[81] D. Fotsch and D. J. Ewins, "Further applications of the FMAC," in *Proc. of the 19th Modal Analysis Conference*, (Kissimmee, FL), pp. 635–639, February 2001.

[82] N. A. J. Lieven and D. J. Ewins, "Spatial correlation of mode shapes, the coordinate modal assurance criterion (COMAC)," in *Proc. of the 6th International Modal Analysis Conference*, (Orlando, FL), pp. 690–695, February 1988.

[83] D. L. Hunt, "Application of an enhanced coordinate modal assurance criterion," in *Proc. of the 10th International Modal Analysis Conference*, (San Diego, CA), pp. 66–71, February 1992.

[84] S. Milecek, "The use of modal assurance criterion extended," in *Proc. of the 12th International Modal Analysis Conference*, (Honolulu, HA), pp. 363–369, February 1994.

[85] M. M. Samman, "Structural damage detection using the modal correlation coefficient (MCC)," in *Proc. of the 15th International Modal Analysis Conference*, (Orlando, FL), pp. 627–630, February 1997.

[86] M. M. Samman, "A modal correlation coefficient for detection of kinks in mode shapes," *ASME Journal of Vibration and Acoustics*, vol. 118, no. 2, p. 271, 1996.

[87] L. D. Mitchell, "Increasing the sensitivity of the modal assurance criteria (MAC) to small mode shape changes: The IMAC," in *Proc. of the 16th International Modal Analysis Conference*, (Santa Barbara, CA), pp. 64–69, February 1998.

[88] W. Heylen and S. Lammens, "FRAC: A consistent way of comparing frequency response functions," in *Proc. of the Conference on Identification in Engineering Systems*, (Swansea, UK), pp. 48–57, March 1996.

[89] A. Fregolent and W. D'Ambrogio, "Evaluation of different strategies in the parametric identification of dynamic models," in *Proc. 16th Biennial ASME Conference on Mechanical Vibration and Noise*, (Sacramento, CA), pp. DETC97/VIB–4154, September 1997.

[90] D. J. Nefske and S. H. Sung, "Correlation of a coarse mesh finite element model using structural system identification and a frequency response criterion," in *Proc. of the 14th International Modal Analysis Conference*, (Detroit, MI), pp. 597–602, February 1996.

[91] H. V. der Auweraer, M. Iadevaia, U. Emborg, M. Gustavsson, U. Tengzelius, and N. Horlin, "Linking test and analysis results in the medium frequency range using principal field shapes," in *Proc. of the 23rd International Seminar on Modal Analysis*, (Leuven, Belgium), p. 8, September 1998.

[92] R. Pascual, J. C. Golinval, and M. Razeto, "A frequency domain correlation technique for model correlation and updating," in *Proc. of the 15th International Modal Analysis Conference*, (Orlando, FL), pp. 587–592, February 1997.

[93] P. Avitabile and F. Pechinsky, "Coordinate orthogonality check (CORTHOG)," in *Proc. of the 12th International Modal Analysis Conference*, (Honolulu, HA), pp. 753–760, February 1994.

[94] F. P. Beer, E. R. Johnston, and J. T. DeWolf, *Mechanics of Materials*. McGraw-Hill, New York, NY,, 3rd ed., 2002.

[95] A. K. Pandey, M. Biswas, and M. M. Samman, "Damage detection from changing in curvature mode shapes," *Journal of Sound and Vibration*, vol. 145, no. 2, pp. 321–332, 1991.

[96] N. Stubbs, J.-T. Kim, and K. Topole, "An efficient and robust algorithm for damage localization in offshore platforms," in *Proc. of the ASCE 10th Structures Congress*, (San Antonio, TX), pp. 543–546, April 1992.

[97] N. Stubbs, J.-T. Kim, and C. R. Farrar, "Field verification of a nondestructive damage localization and severity estimation algorithm," in *Proc. of the 13th International Modal Analysis Conference*, (Nashville, TN), pp. 210–218, February 1995.

[98] C. Dong, P. Q. Zhang, W. Q. Feng, and T. C. Huang, "The sensitivity study of the modal parameters of a cracked beam," in *Proc. of the 12th International Modal Analysis Conference*, (Honolulu, HA), pp. 98–104, February 1994.

[99] O. S. Salawu and C. Williams, "Bridge assessment using forced-vibration testing," *Journal of Structural Engineering*, vol. 121, no. 2, pp. 161–173, 1994.

[100] A. E. Aktan, K. L. Lee, C. Chuntavan, and T. Aksel, "Modal testing for structural identification and condition assessment of constructed facilities," in *Proc. of the 12th International Modal Analysis Conference*, (Honolulu, HA), pp. 462–468, February 1994.

[101] A. K. Pandey and M. Biswas, "Damage detection in structures using changes in flexibility," *Journal of Sound and Vibration*, vol. 169, no. 1, pp. 3 – 17, 1994.

[102] T. Toksoy and A. Aktan, "Bridge-condition assessment by modal flexibility," *Experimental Mechanics*, vol. 34, no. 3, pp. 271–278, 1994.

[103] S. W. Doebling, L. D. Peterson, and K. F. Alvin, "Experimental determination of local structural stiffness by disassembly of measured flexibility matrices," *Journal of Vibration and Acoustics*, vol. 120, no. 4, pp. 949–957, 1998.

[104] Z. Zhang and A. E. Atkan, "The damage indices for constructed facilities," in *Proc. of the 13th International Modal Analysis Conference*, (Nashville, TN), pp. 1520–1529, February 1995.

[105] C. S. Lin, "Location of modeling errors using modal test data," *AIAA Journal*, vol. 28, no. 9, pp. 1650–1654, 1990.

[106] C. S. Lin, "Unity check method for structural damage detection," in *Proc. of the 35th AIAA/ASME/ASCE/AHS/ASC Structures, Structural Dynamics and Materials Conference*, no. AIAA-1994-1717, (Hilton Head, SC), pp. 347–354, April 1994.

[107] J. He and D. J. Ewins, "Analytical stiffness matrix correction using measured vibration modes," *Modal Analysis: The International Journal of Analytical and Experimental Modal Analysis*, vol. 1, no. 3, pp. 9–14, 1986.

[108] H. P. Gysin, "Critical application of an error matrix method for location of finite element modeling inaccuracies," in *Proc. of the 4th International Modal Analysis Conference*, (Los Angeles, CA), pp. 1339–1351, February 1986.

[109] Y. S. Park, H. S. Park, and S. S. Lee, "Weighted-error-matrix application to detect stiffness damage-characteristic measurement," *Modal Analysis: The International Journal of Analytical and Experimental Modal Analysis*, vol. 3, no. 3, pp. 101–107, 1988.

[110] S. W. Doebling, L. D. Peterson, and K. F. Alvin, "Estimation of reciprocal residual flexibility from experimental modal data," *AIAA Journal*, vol. 34, no. 8, pp. 1678–1685, 1996.

[111] S. W. Doebling, L. D. Peterson, and K. F. Alvin, "Measurement of static flexibility matrices for experiments with incomplete reciprocity," in *Proc. of the 36th AIAA/ASME/ASCE/AHS/ASC Structures, Structural Dynamics and Materials Conference*, no. AIAA-95-1092, (New Orleans, LA), pp. 2777–2791, April 1995.

[112] O. S. Salawu and C. Williams, "Structural damage detection using experimental modal analysis–a comparison of some methods," in *Proc. of the 11th International Modal Analysis Conference*, (Orlando, FL), pp. 254–260, February 1993.

[113] L. D. Peterson, K. F. Alvin, S. W. Doebling, and K. C. Park, "Damage detection using experimentally measured mass and stiffness matrices," in *Proc. of the 34th AIAA/ASME/ASCE/AHS/ASC Structures, Structural Dynamics and Materials Conference*, no. AIAA-93-1482, (La Jolla, CA), pp. 1518–1528, April 1993.

[114] I. U. Ojalvo and D. Pilon, "Diagnostics for geometrically locating structural math model errors from modal test data," in *Proc. of the 29th AIAA/ASME/ASCE/AHS/ASC Structures, Structural Dynamics and Materials Conference*, no. AIAA-1988-2358, pp. 1174–1186, 1988.

[115] F. M. Hemez, *Theoretical and Experimental Correlation Between Finite Element Models and Modal Tests in the Context of Large Flexible Space Structures*. PhD thesis, Dept. of Aerospace Engineering Sciences, University of Colorado, Boulder, CO, 1993.

[116] T. W. Lim, "Structural damage detection of a planar truss structure using a constrained eigenstructure assignment," in *Proc. of the 35th AIAA/ASME/ASCE/AHS/ASC Structures, Structural Dynamics and Materials Conference*, no. AIAA-1994-1715, (Hilton Head, SC), April 1994.

[117] T. W. Lim, "Structural damage detection using constrained eigenstructure assignment," *Journal of Guidance, Control, and Dynamics*, vol. 32, no. 5, pp. 1049–1057, 1995.

[118] H. M. Kim and T. J. Bartkowicz, "Damage detection and health monitoring of large space structures," *Sound and Vibration*, vol. 27, no. 6, pp. 12–17, 1993.

[119] H. M. Kim and T. J. Bartkowicz, "A two-step structural damage detection using a hexagonal truss structure," in *Proc. of the 35th AIAA/ASME/ASCE/AHS/ASC Structures, Structural Dynamics and Materials Conference*, no. AIAA-1994-1713, (Hilton Head, SC), pp. 318–324, April 1994.

[120] C. Li and S. W. Smith, "A hybrid approach for damage detection in flexible structures," in *Proc. of the 35th AIAA/ASME/ASCE/AHS/ASC Structures, Structural Dynamics and Materials Conference*, no. AIAA-1994-1710, (Hilton Head, SC), pp. 285–295, April 1994.

[121] C. Li and S. W. Smith, "Hybrid approach for damage detection in flexible structures," *Journal of Guidance, Control, and Dynamics*, vol. 18, no. 3, pp. 419–425, 1995.

[122] C. M. Bishop, *Neural Networks for Pattern Recognition*. Oxford University Press, New York, NY, 1995.

[123] R. O. Duda and P. E. Hart, *Pattern Classification and Scene Analysis*. John Wiley & Sons, New York, NY, 1973.

[124] K. Fukunaga, *Introduction to Statistical Pattern Recognition*. Academic Press, San Diego, CA, 2nd ed., 1990.

[125] C. W. Therrien, *Decision Estimationand Classification: An Introduction to Pattern Recognition and Related Topics*. John Wiley & Sons, New York, NY, 1989.

[126] C.-H. Chen, *Statistical Pattern Recognition*. Hayden Book Co., Rochelle Park, NJ, 1973.

[127] A. Nigrin, *Neural Networks for Pattern Recognition*. MIT Press, Cambridge, MA, 1993.

[128] J. N. Kudva, N. Munir, and P. W. Tan, "Damage detection in smart structures using neural networks and finite-element analysis," *Smart Materials and Structures*, vol. 1, no. 2, pp. 108–112, 1992.

[129] X. Wu, J. Ghaboussi, and J. H. Garrett, "Use of neural networks in detection of structural damage," *Computers and Structures*, vol. 42, no. 4, pp. 649–659, 1992.

[130] M. F. Elkordy, K. C. Chang, and G. C. Lee, "Neural network trained by analytically simulated damage states," *Journal of Computing in Civil Engineering*, vol. 7, no. 2, pp. 130–145, 1993.

[131] J. E. Stephens and R. D. VanLuchene, "Integrated assessment of seismic damage in structures," *Microcomputers in Civil Engineering*, vol. 9, no. 2, pp. 119–128, 1994.

[132] J. Rhim and S. W. Lee, "A neural network approach for damage detection and identification of structures," in *Proc. of the 35th AIAA/ASME/ASCE/AHS/ASC Structures, Structural Dynamics and Materials Conference*, no. AIAA-1994-1753, (Hilton Head, SC), pp. 173–180, April 1994.

[133] W. Spillman, D. Huston, P. Fuhr, and J. Lord, "Neural network damage detection in a bridge element," in *Proc. of SPIE: Smart Sensing, Processing, and Instrumentation*, vol. 1918, (Albuquerque, NM), pp. 288–295, February 1993.

[134] R. Manning, "Damage detection in adaptive structures using neural networks," in *Proc. of the 35th AIAA/ASME/ASCE/AHS/ASC Structures, Structural Dynamics and Materials Conference*, no. AIAA-1994-1752, (Hilton Head, SC), pp. 160–172, April 1994.

[135] C. Povich and T. Lim, "An artificial neural network approach to structural damage detection using frequency response functions," in *Proc. of the 35th AIAA/ASME/ASCE/AHS/ASC Structures, Structural Dynamics and Materials Conference*, no. AIAA-1994-1751, (Hilton Head, SC), pp. 151–159, April 1994.

[136] P. Z. Szewczyk and P. Hajela, "Damage detection in structures based on feature-sensitive neural networks," *Journal of Computing in Civil Engineering*, vol. 8, no. 2, pp. 163–178, 1994.

[137] P. Tsou and M.-H. H. Shen, "Structural damage detection and identification using neural networks," *AIAA Journal*, vol. 32, no. 1, pp. 176–183, 1994.

[138] B. J. Schwarz, P. L. McHargue, and M. H. Richardson, "Using SDM to train neural networks for solving modal sensitivity problems," in *Proc. of the 14th International Modal Analysis Conference*, (Detroit, MI), pp. 1285–1291, February 1996.

[139] S. E. Olson, M. P. DeSimio, and M. M. Derriso, "Fastener damage estimation in a square aluminum plate," *Structural Health Monitoring*, vol. 5, pp. 173–183, June 2006.

[140] M. DeSimio, I. Miller, M. Derriso, K. Brown, and M. Baker, "Structural health monitoring experiments with a canonical element of an aerospace vehicle," in *Proc. of the 2003 IEEE Aerospace Conference*, vol. 7, (Piscataway, NJ), pp. 3105–3111, March 2003.

[141] M. DeSimio, S. Olson, and M. Derriso, "Decision uncertainty in a structural health monitoring system," *Proc. of SPIE*, vol. 5764, pp. 530–541, 2005.

[142] J. C. S. Yang, J. Chen, and N. G. Dagalakis, "Damage detection in offshore platforms by the random decrement technique," *ASME Journal of Energy Resources Technology*, vol. 106, pp. 38–42, 1984.

[143] O. V. Shiryayev, *Improved Structural Health Monitoring Using Random Decrement Signatures*. PhD thesis, Wright State University, Dayton, OH, 2008.

[144] S. S. Law, P. Waldron, and C. Taylor, "Damage detection of a reinforced concrete bridge deck using the frequency response function," in *Proc. of the 10th International Modal Analysis Conference*, (San Diego, CA), pp. 772–778, February 1992.

[145] A. J. W. McClung, "Design for structural health monitoring for location of fastener failure in thermal protection systems," Master's thesis, Wright State University, 2005.

[146] *ABAQUS Users Manual*.

[147] N. M. M. Maia and J. M. M. Silva, eds., *Theoretical and Experimental Modal Analysis*. Research Studies Press Ltd., Baldock, Hertfordshire, England, 1997.

[148] S. Braun, D. Ewins, and S. Rao, eds., *Encyclopedia of Vibration*. Academic Press, San Diego, CA, 2002.

[149] Vanderplaats Research & Development, *VisualDOC How to Manual*, 2006.